Bitlis Eren Üniversitesi
Fen Bilimleri Dergisi

Bitlis Eren University
Journal of Science

ISSN : 2147-3129
e-ISSN : 2147-3188

Cilt / *Volume*: 8 Sayı / *Number*: Özel Sayı Yıl / *Year*: 2019

Yazışma Adresi

Bitlis Eren Üniversitesi
Fen Bilimleri Enstitüsü
13000, Merkez, Bitlis/TÜRKİYE
Tel: 0 (434) 2220071

fbe@beu.edu.tr
http://dergipark.gov.tr/bitlisfen

Yayın Kurulu / *Editorial Board*

Danışma Kurulu / *Advisory Board*

Hakem Kurulu / *Reviewer Board*

Dergi Hakkında / *About Journal*

Bitlis Eren Üniversitesi Fen Bilimleri Dergisi, mühendislik ve temel bilimler alanlarındaki gelişmeleri ve yenilikleri takip etmek, meslek kuruluşlarının, araştırmacıların ve bireylerin ulusal ve uluslararası gelişimlerine katkıda bulunmak ve bu alanlarda elektronik bir kaynak oluşturmak amacıyla yayımlanmaktadır. Derginin yazım dili Türkçe veya İngilizcedir. Fen Bilimleri Dergisi, Bitlis Eren Üniversitesi Fen Bilimleri Enstitüsü yayını olup, 2012 yılından bu yana ücretsiz ve açık erişimli olarak yayın hayatına devam etmektedir. Mühendislik ve temel bilimlerin bilgi tabanına ve teknolojik gelişmelere ışık tutması amacıyla bu alanlarda yapılmış deneysel ve teorik ilerlemeleri konu alan özgün araştırma makalelerine, derlemelere ve teknik notlara yer verilmektedir. Dergiye gönderilen çalışmaların benzerlik oranı %15'i geçmemelidir. Yazım kurallarına uymayan makaleler, hakemlere gönderilmeden önce düzeltilmek üzere yazara geri gönderilir. Bu nedenle, derginin yazım kuralları dikkate alınmalıdır. Ayrıca, editörlerden yazarlara iletilen düzeltmelere veya taleplere 15 gün içerisinde cevap verilmediği takdirde ilgili makaleler reddedilir. Makaleler şekiller ve tablolar dâhil 20 sayfayı geçmemelidir. Dergiye yayın için gönderilen makaleler en az iki hakem tarafından değerlendirilir. Yazarlardan hakem önerisi talep edilmemektedir. Makalelerin dergide yayımlanabilmesi için hakemler tarafından olumlu görüş bildirilmesi gerekmektedir. Dergi Editör Kurulu, hakem raporlarını (*iki hakemin değerlendirmeleri geldikten sonra*) dikkate alarak makalelerin yayımlanmak üzere kabul edilip edilmemesine karar verir. Fen Bilimleri Dergisi, yılda dört defa (*Mart, Haziran, Eylül, Aralık*) yayımlanmaktadır. **Dergimiz Tübitak-Ulakbim Mühendislik ve Temel Bilimler Veri Tabanı Dergi Listesinde taranmaktadır.**

B.E.Ü. Fen Bilimleri Dergisi 8(Özel Sayı), 2019 / *B.E.U. Journal of Science 8(Special Issue), 2019*

İÇİNDEKİLER / *CONTENTS*

Araştırma Makaleleri (NSP 2019) / *Research Articles (NSP 2019)*

Araştırma Makalesi / Research Article

Examination of Radiation Absorption Properties of $Pb(NO_3)_2$ Doped Wallpapers

Yusuf KAVUN*

Kahramanmaras Sutcu Imam University, Vocational School of Health Services, Department of Medical Imaging Techniques, Kahramanmaras, Turkey
(ORCID: 0000-0001-9635-4388)

Abstract
The harmful effects of radiation on human health have long been recognized. These effects include radiation burns, radiation diseases, shortening of life span, cancer and hereditary disorders. Therefore, the absorption properties and applicability of the material used in radiation shielding are very important. Hence, studies are underway on the development of different types of shielding materials. In this study, radiation absorption properties of lead (II) nitrate $Pb(NO_3)_2$ coated wall papers were investigated. The wall papers in different densities (100% precipitated calcium carbonate (PCC), 2.5 g, 5 g, and 7.5 g amounts of $Pb(NO_3)_2$) and various thicknesses (0.176-0.236 mm) were prepared and investigated. 4 MeV-energized electrons were applied to the $Pb(NO_3)_2$ coated wall papers and measurements were taken with the PTW brand electron detector. Also, theoretical calculations have been done by using WinXCom program. According to the obtained results, these wallpapers' absorption properties increased depending on thickness. Thus, it has been seen that the $Pb(NO_3)_2$ coated wallpapers can be used with other materials in radiation shielding.

Keywords: Radiation, shielding, wallpaper, lead (II) nitrate.

$Pb(NO_3)_2$ Katkılı Duvar Kâğıtlarının Radyasyon Soğurma Özelliklerinin İncelenmesi

Öz
Radyasyonun insan sağlığı üzerindeki zararlı etkileri uzun zamandır bilinmektedir. Bu etkiler radyasyon yanıkları, radyasyon hastalıkları, yaşam süresinin kısalması, kanser ve kalıtsal bozuklukları içerir. Bu nedenle, radyasyon zırhlamada kullanılan malzemenin soğurma özellikleri ve uygulanabilirliği çok önemlidir. Bu nedenle, farklı koruyucu malzemelerin geliştirilmesi üzerine çalışmalar devam etmektedir. Bu çalışmada kurşun(II) nitrat $Pb(NO_3)_2$ kaplamalı duvar kâğıtlarının radyasyon soğurma özellikleri araştırılmıştır. Farklı yoğunluklarda (%100 çökeltilmiş kalsiyum karbonat (PCC), 2.5 g, 5 g ve 7.5 g $Pb(NO_3)_2$) ve çeşitli kalınlıklarda (0.176-0.236 mm) duvar kağıtları hazırlandı ve araştırıldı. $Pb(NO_3)_2$ kaplanmış kağıtlara 4 MeV-enerjili elektron uygulandı ve PTW marka elektron detektörü ile ölçümler alındı. Ayrıca, WinXCom programı kullanılarak teorik hesaplamalar yapıldı. Elde edilen sonuçlara göre, bu duvar kâğıtlarının soğurma özellikleri kalınlığa bağlı olarak artmıştır. Böylece, $Pb(NO_3)_2$ kaplı duvar kağıtlarının diğer malzemelerle birlikte radyasyon zırhlamada kullanılabileceği görülmüştür.

Anahtar kelimeler: Radyasyon, zırhlama, duvar kâğıdı, kurşun (II) nitrat.

1. Introduction

Radiation has been a part of our world since the formation of the universe. In this process, humanity has always been exposed to natural radiation from Earth and space. However, it is available in situations where radiation is artificially produced and used. For example, X-rays can be used to diagnose and treat diseases and can be used in industrial applications. In addition, the radiation released by accidents as a result of failures in nuclear facilities can damage humanity and nature. In all these cases, the most

*Sorumlu yazar: yusufkavun@gmail.com
Geliş Tarihi: 07.10.2019, Kabul Tarihi: 19.12.2019

important principles of radiation protection are exposure time, shielding and distance. In this way the amount of dose exposed can be prevented or reduced by using simple preventive measures. In cases where radiation is used, exposure time should be limited to as much as necessary, the distance from the radiation source should be maximized and the source should be protected wherever possible [1]. To measure personal dose intake in the event of occupational or emergency exposure, personal dosimeters should be used for external radiation and bioassay techniques should be applied for the internal dose due to ingestion of radioactive contamination [2].

In radiation shielding, the radioactive particles are blocked by a barrier or barrier material to provide absorption of radiation. charged particle energies are reduced by methods such as photoelectric, scattering or double formation according to the attenuation principle of energy by interacting with the electrons of the material in the barrier. Thus, the particles can be rendered less harmful by, for example, elastic or inelastic scattering events of neutrons [3].

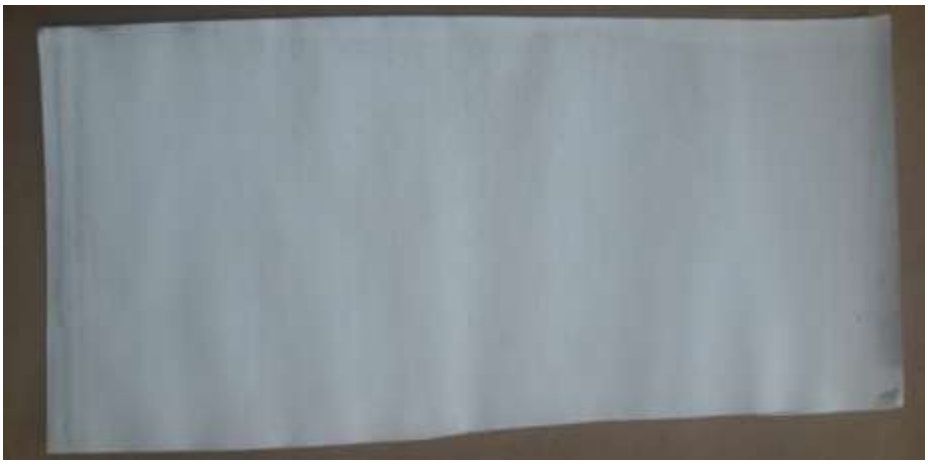

Figure 1. Example of $Pb(NO_2)_3$ doped wallpaper

To date, many materials have been developed for radiation shielding purposes. The amount of absorption varies according to the properties of the material to be produced. $Pb(NO_3)_2$ can be a good shielding material in terms of properties. Its molar mass 331.2 g/mol and density are 4.53 g/cm^3 (20°C). $Pb(NO_3)_2$ is used in textile dyeing, nylon and polyesters and as heat stabilizers and as photo thermographic paper. $Pb(NO_3)_2$ is used to improve speed and yield, particularly in the processing of partially oxidized ores. It is also an oxidant in the paint industry [4].

In this study, $Pb(NO_3)_2$ doped wallpapers were used for radiation shielding (Figure 1). 100% precipitated calcium carbonate (PCC) and $Pb(NO_3)_2$ materials of different densities and thicknesses were added to the surfaces of these papers. These wallpapers can be used for the purpose of shielding radiation in different places. For example, it can be used in radiation treatment centres to prevent exposure of patients and workers to radiation doses.

2. Material and Method

In this study, $Pb(NO_3)_2$ salts (100% precipitated calcium carbonate (PCC), 2.5 g., 5 g. and 7.5 g.) were applied to 85 g. wallpaper surface obtained from markets. By using VARIAN brand [5,6] linear accelerator, 4 MeV energized electrons are applied to wallpaper that are placed between solid phantoms. PTW [7] brand electron detector was used for dose measurements. Every measurement was repeated 3 times following the same method. The wallpapers samples were placed at a distance of 100 cm from the gantry and the detector was placed just below the samples as can be seen in Figure 2.

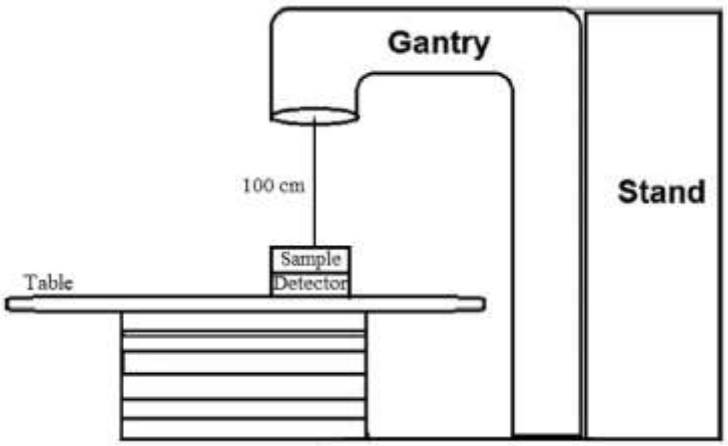

Figure 2. Experimental setup

The amount of radiation absorption of wallpaper is determined by Beer-Lambert's law [1,3];

$$I = I_0 . e^{-\mu t} \quad (1)$$

Here, I is sample counts, t (cm) is the thickness of the sample, I_0 is the sample-free counts and μ (cm^{-1}) is the linear absorption coefficient. Equation (1) was used in the calculation of linear absorption coefficient and results were obtained according to the properties of the absorber material. Description of the half-layer (HVL) is the thickness of the material which can pass half of the radiation interacting with the material. Also, description of tenth value layer (TVL) are the thickness of material capable of passing one-tenth of the radiation interacting with the material [3,8].

$$HVL = \frac{\ln 2}{\mu} \quad (2)$$

$$TVL = \frac{\ln 10}{\mu} \quad (3)$$

Preparation of the mortar to be applied to the wallpaper's surface is as follows: In order to develop shielding materials, mixtures containing lead(II)nitrate $Pb(NO_3)_2$ salts were prepared separately by taking calcium carbonate (PCC) precipitated in 5%, 10% and 15% ratios, 15% starch and 85%, 80%, 75% and 70% ratios specified in the table below. Prepared mixtures and their ratios are shown in Table 1.

Table 1. Preparation of $Pb(NO_3)_2$ doped coated mortar at different mixing ratios

Group	$Pb(NO_3)_2$ (%)	Starch (%)	PCC(%)
1	0	15	85
2	5	15	80
3	10	15	75
4	15	15	70

Also, the radiation shielding quantities of $Pb(NO_3)_2$ doped wallpapers systems were investigated using WinXCom package software [9] in the energy of 14 MeV. The total linear absorption coefficient (μ) value of wallpapers systems were calculated by using WinXCom software based on the mixture rule [9]. The calculation results can be seen in Table 2.

3. Results and Discussion

The structure of the shielding material is important in terms of radiation permeability. In controlled and uncontrolled areas, the shielding design is designed to meet the recommended effective dose limits for staff and patient. Equivalent radiation dose is 0.02mSv per week, except in public and uncontrolled areas.

The radiation permeability of some produced materials is shown in Figure 3. Here can be seen the absorption coefficients obtained by adding some quantities of $Pb(NO_3)_2$ (PCC, 2.5 g., 5g. and 7.5g.)

to the coating mortar used for coating the wallpaper surface. The wallpaper thickness and attenuation coefficients obtained by applying the mortar prepared using lead nitrate in different proportions to the wallpaper surface are given in Table 2. Also, the total absorption coefficients calculated by the WinXCom program are also given in the Table 2. The ratios in Table 1 are used for the values calculated with the WinXCom program. Table 2 shows that values calculated with the WinXCom program have been given higher results. Furthermore, the linear attenuation coefficients have been increased as the thickness increases. The half-value thickness (HVL) and one-tenth thickness (TVL) values calculated using these linear attenuation coefficients are given in Table 3. HVL and TVL values decreased as thickness increased. This indicates that the absorption efficiency of the wallpaper increases according to the thickness of the material. Figure 4 shows the comparison of HVL and TVL values obtained by using (2) and (3) equations.

Table 2. Thickness and linear attenuation coefficient values of wallpapers doped with $Pb(NO_3)_2$

Layer	PCC Thick. (mm)	μ(cm^{-1})	2.5 g Thick. (mm)	μ(cm^{-1})	5.0 g Thick. (mm)	μ(cm^{-1})	7.5 g Thick. (mm)	μ(cm^{-1})
3	0.192	0.0047	0.187	0.0048	0.212	0.0099	0.201	0.01203
6	0.196	0.0055	0.211	0.0071	0.221	0.0110	0.207	0.01422
9	0.206	0.0080	0.216	0.0087	0.231	0.0124	0.224	0.01685
WinXCom		0.0255		0.0308		0.0337		0.0355

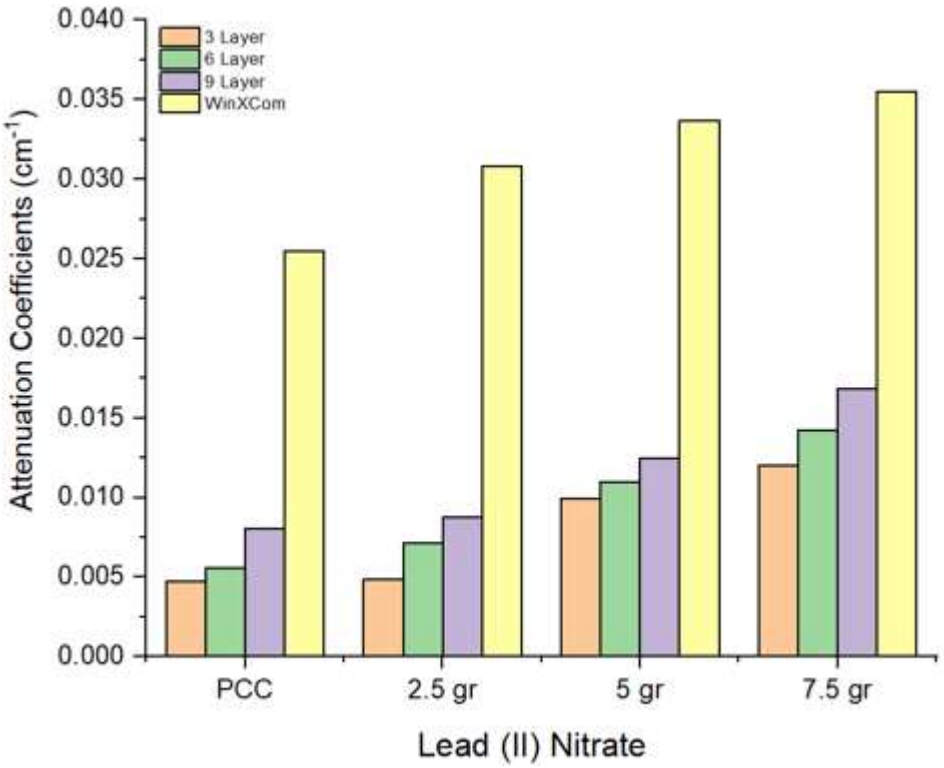

Figure 3. Linear attenuation coefficient values of wallpapers coated with $Pb(NO_3)_2$ obtained by applying 4 MeV energy electrons

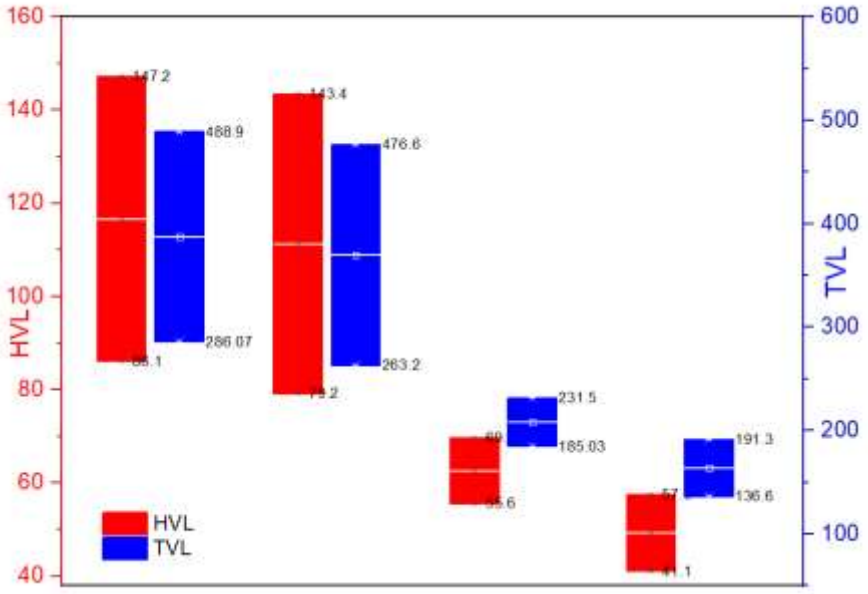

Figure 4. The comparison of HVL and TVL values of $Pb(NO_3)_2$

Table 3. Calculated HVL and TVL values of $Pb(NO_3)_2$

Thickness	HVL	TVL
PCC Thickness		
0.192	147.2	488.9
0.196	124.5	413.8
0.206	86.1	286.0
2.5 g Thickness		
0.187	143.4	476.6
0.211	96.8	321.6
0.216	79.2	263.2
5.0 g Thickness		
0.212	69.7	231.5
0.221	62.9	209.2
0.231	55.6	185.03
7.5 g Thickness		
0.201	57.6	191.3
0.207	48.7	161.8
0.224	41.1	136.6

4. Conclusion

In this study, the absorption coefficients of Lead (II) Nitrate ($Pb(NO_3)_2$) doped wallpapers were calculated and its radiation shielding properties were examined. Linear absorption coefficients obtained using 4 MeV energy electrons have been increased as the thickness of the material covered in the wallpaper increased. HVL and TVL values decreased due to these linear absorption coefficients. As can be seen from these results, radiation shielding materials can be derivable by using $Pb(NO_3)_2$. Lead (II) nitrate can be used for shielding in controlled or uncontrolled areas where radiation is used by mixing various percentages in building materials such as wallpapers or cement as examined in this study.

Acknowledgement

I would like to thank to valuable contributions to this study to Prof. Dr. Ahmet TUTUŞ, Assoc. Prof. Dr. Serhan URUŞ, Lecturer MSc. Selami EKEN and MSc. Ruken ÖZBEK.

References

[1] Martin J.E. 2008. Physics for Radiation Protection: A Handbook. 2nd Edition, Completely Revised and Enlarged, Wiley, USA, 844 p.
[2] Institute of Medicine. 1996. Radiation in Medicine: A Need for Regulatory Reform. Washington, DC: The National Academies Press. https://doi.org/10.17226/5154.
[3] Krane K.S. 1988. Introductory Nuclear Physics. John Wiley & Sons Inc., USA, 858 p.
[4] Arnikar H.J. 1982. Essentials of nuclear chemistry. Wiley Eastern, New Delhi, 335 p.
[5] Varian. 2012. Varian Medical Systems, Clinac, On-Board Imager and Rapidarc, Are Registered Trademarks, and Exact and Laserguard Are Trademarks of Varian Medical Systems. https://www.varian.com/sites/default/files/resource_attachments/Clinac.pdf (Erişim Tarihi: 13.12.2019).
[6] Altman M., Westerly D., Wen N., Zhao B., Miften M., Chetty I.J., Solberg T. 2013. Commissioning of the Varian True Beam linear accelerator: A multi-institutional study. Medical Physics, 40 (3): 031719-15.
[7] PTW-Freiburg and Ptw-New York. 2017. Advanced Markus, Bragg Peak, Curiementor, Diamentor, Farmer, Markus, Nomex, Octavıus, Pin Point, Roos. https://www.ptwdosimetry.com/overview-pages/detectors-for-absolute-dosimetry/?L=0 (Erişim Tarihi: 13.12.2019).
[8] Agar O. 2018. Investigation on Gamma Radiation Shielding Behaviour of CdO–WO3–TeO2 Glasses from 0.015 to 10 MeV. Cumhuriyet Science Journal, 39 (4): 983-990.
[9] Gerward L., Guilbert N., Jensen K.B., Levring H. 2004. WinXCom-a program for calculating X-ray attenuation coefficients. Radiation Physics Chemistry 71: 653–654.

Araştırma Makalesi / Research Article

Examining Nonstandard Higgs Couplings via Photon-Photon Fusion at FCC

Gülistan AKKAYA SELÇİN*

Bitlis Eren University, Faculty of Science, Physics Department, Bitlis
(ORCID: 0000-0003-4720-6631)

Abstract
In this paper, the constraints on the non-standard HZγ and Hγγ couplings through the exclusive single Higgs production process pp →pγγp →pHp at a future 100 TeV proton-proton collider have been examined. As the signal, H→γγ and H→Zγ decay channels of the Higgs boson have been considered. Taking into account three different acceptance regions of 0.015<ξ<0.15, 0.0015< ξ <0.5, 0< ξ <1-$\frac{m_p}{E}$ and integrated luminosity of L_{int} = 3000 fb^{-1}, it has been found 95% C.L. sensitivity constraints on these couplings. Similar calculations have been made at the LHC and discussed the improvement which is provided by a future 100 TeV proton-proton collider with respect to LHC.

Key words: Higgs couplings, single Higgs production, 100 TeV proton-proton collider.

FCC'de Foton-Foton Füzyonu Yoluyla Anormal Higgs Bağlaşımları'nın İncelenmesi

Öz
Bu çalışmada, 100 TeV proton-proton çarpıştırıcısında, harici tek Higgs üretimi olan pp →pγγp →pHp süreci üzerinden anormal HZγ ve Hγγ bağlaşımlarının sınırları incelenmiştir. Sinyal olarak, Higgs bozonunun H→γγ ve H→Zγ bozounum kanalları ele alınmıştır. Üç farklı akseptans bölgesi 0.015<ξ<0.15; 0.0015< ξ <0.5; 0< ξ <1-$\frac{m_p}{E}$ ve integre edilmiş luminosite L_{int} = 3000 fb^{-1} değerleri dikkate alınarak, bu bağlaşımların %95 güvenilirlik düzeyindeki duyarlılık limitleri bulunmuştur. Aynı hesaplar LHC için de yapılmış ve gelecekte kurulması planlanan 100 TeV proton-proton çarpıştırıcısının LHC'ye göre sağladığı iyileştirme yorumlanmıştır.

Anahtar kelimeler: Higgs bağlaşımları, tek Higgs üretimi, 100 TeV proton-proton çarpıştırıcısı.

1. Introduction

The physics potential of a future 100 TeV proton-proton collider has been discussed recently by the physics community and the interest in the subject is growing rapidly [1-3]. Such a very high energetic machine has a great potential to probe the new physics. The predictions of the SM have been confirmed by previous and present experiments. The last great confirmation of the SM is the discovery of the Higgs boson [4,5]. The next step is to study the properties of Higgs boson and its couplings to other SM particles. These studies will confirm the SM and will be useful for new physics beyond SM. The future 100 TeV proton-proton collider provides an ideal venue to measure non-standard couplings of the Higgs boson. Phenomenological studies on non-standard Higgs couplings in a future 100 TeV collider have been rapidly growing in the literature [1,3,6-12]. In this article we consider exclusive single Higgs production process pp →pγγp →pHp in a 100 TeV proton-proton collider. A schematic diagram of this reaction is given in Figure 1.

*Sorumlu yazar: gakkaya@beu.edu.tr
Geliş Tarihi: 15.10.2019, Kabul Tarihi: 19.12.2019

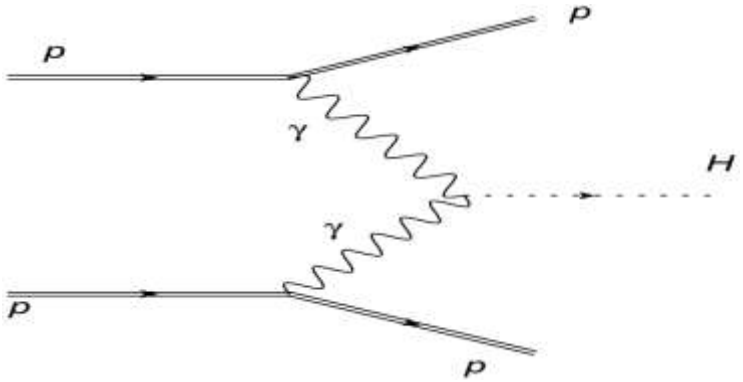

Figure 1. Exclusive single Higgs boson production through photon-photon fusion in a pp collision.

In such a reaction, incoming protons emit two quasi-real photons which have a very low virtuality and then these photons interact each other to produce a Higgs boson. Initial protons do not dissociate into partons becouse the virtuality of emitted photons are very low. This production provide a very clean experimental environment which is free from serious uncertainties coming from parton jets, because there aren't any proton remnants. This circumstance makes it easy to detect the signal that we want to measure. Furthermore, photon-induced processes are electromagnetic in nature, free from complicated QCD backgrounds. The exclusive production was studied experimentally at the Large Hadron Collider (LHC) and also at the former hadron collider Fermilab Tevatron [13-24]. It was verified that complementary to deep inelastic hadron collisions, photon-induced processes via equivalent photons can be studied in a hadron collider. Therefore, it is interesting to investigate such photon-induced processes in the future proton collider.

2. The cross section and non-standard HZγ and Hγγ couplings

The single Higgs can be produced through the interaction of two equivalent photons emitted from the incoming proton beams. Although the Higgs boson does not couple minimally to two photons, Hγγ vertex gets SM contributions from one-loop level. There may be also new physics contributions which modify this vertex. Hence, in principle these new physics contributions can be probed by measuring the production cross section. However, Higgs bosons cannot be detected directly by the detectors. It can be detected from its decay products. Final-state particles' invariant mass measurement will confirm the existence of on-mass-shell Higgs bosons. As the signal,we consider H→γγ and H→Zγ decay channels of the Higgs boson. Taking into account the narrow width approximation for the processes γγ→ H→ Zγ and γγ→ H→ γγ the cross section can be calculated easily:

$$\sigma(\gamma\gamma\rightarrow \mathrm{H}\rightarrow\gamma\gamma) = \frac{8\pi^2}{m_H}\frac{\Gamma_{\gamma\gamma}{}^2}{\Gamma_{\mathrm{total}}}\delta(s-m_H^2) \quad (1)$$

$$\sigma(\gamma\gamma\rightarrow \mathrm{H}\rightarrow \mathrm{Z}\gamma) = \frac{8\pi^2}{m_H}\frac{\Gamma_{\gamma\gamma}\Gamma_{\mathrm{Z}\gamma}}{\Gamma_{\mathrm{total}}}\delta(s-m_H^2) \quad (2)$$

where $\Gamma_{\mathrm{z}\gamma}$ and $\Gamma_{\gamma\gamma}$ represent the decay width of H→ Zγ and H→γγ respectively, Γ_{tot} is the Higgs boson's total decay width, and *s* is the Mandelstam parameter of the initial state photon pair. During numerical calculations, Higgs boson's total decay width is taken to be $\Gamma_{\mathrm{tot}} = 6.1$ MeV [25]. The total cross section of the main process pp →pγγp →pHp→ pγγ(Zγ)p in the proton-proton collision can be obtained by integrating the cross section for sub-processes over the equivalent photon distribution functions:

$$\sigma\,(\mathrm{pp}\rightarrow \mathrm{p}\gamma\gamma\mathrm{p}\rightarrow \mathrm{pHp}\rightarrow \mathrm{p}\gamma\gamma(\mathrm{Z}\gamma)\mathrm{p}) = \int_{x_{min}}^{x_{max}} dx_1 \int_{x_{min}}^{x_{max}} dx_2\; f_\gamma(x_1) f_\gamma(x_2)\; \sigma\left(\gamma\gamma\rightarrow \mathrm{H}\rightarrow \gamma\gamma(\mathrm{Z}\gamma)\right) \quad (3)$$

Here, $f_\gamma(x_{1(2)})$ is the equivalent photon distribution function, $x_{1(2)}$ is the fraction that denotes the ratio between the emitted equivalent photon and incoming proton energies ; $x_{1(2)} = \frac{E_{\gamma_{1(2)}}}{E_p}$. After appropriate change of variables and using the Dirac delta functional in the cross sections Eq.(1) and Eq.(2), the two-dimensional integral in Eq.(3) is reduced to the following one-dimensional integral:

$$\sigma\,(pp \rightarrow p\gamma\gamma p \rightarrow pHp \rightarrow p\gamma\gamma(Z\gamma)p) = \frac{8\pi^2}{m_H}\frac{{\Gamma_{\gamma\gamma}}^2(\Gamma_{Z_\gamma}/\Gamma_{\gamma\gamma})}{\Gamma_{\text{total}}} \times \int_{Max\left(\frac{{m_H}^2}{4E_p x_{max}}, E_p\, x_{min}\right)}^{E_p x_{max}} \frac{dy}{4y} f_\gamma(y) f_\gamma\left(\frac{{m_H}^2}{4y}\right) \quad (4)$$

Here, *y* is the one of the equivalent photon's energy. The *x* parameter's lower and upper bounds can be found easily from the kinematical constraints; $0< x <1-\frac{m_p}{E_p}$. At high energetic collisions the x parameter can be assumed to be equal to the momentum fraction loss $\xi= (|\vec{p}|-|\vec{p}'|)/\vec{p}$ of the intact scattered protons. In this formula, $\vec{p}$ represents the incoming proton's momentum and $\vec{p}\,'$represents the intact scattered proton's momentum. After emission of the elastic photon, protons deviate lightly from the beam direction and can't be detected by the central detectors. The lost energy signature that arises from this situation called the large rapidity gap. The large rapidity region's lost energy signature is used to identify the exclusive processes. Furthermore, very forward detectors can detect the intact scattered protons.The detection of intact protons in the very forward detectors provides an accurate identification of an exclusive process. The LHC is designed to equip with very forward detectors [15, 16, 26]. We assume that a similar very forward detector equipment will be installed on the future proton-proton collider. The very forward detectors have a limited range. They cannot detect all scattered protons in the kinematically allowed interval, $0< \xi <1-\frac{m_p}{E_p}$. The upper and lower limits of forward detector's ranges which called the forward detector acceptances are ξ_{max} and ξ_{min} respectively. During numerical calculations, in addition to the whole region $0< \xi <1-\frac{m_p}{E_p}$, we will take into account forward detector acceptances of $0.0015< \xi <0.5$ and $0.015<\xi<0.15$. In this paper we work in a model independent framework and concern with non-standard Higgs couplings to gauge bosons. Thus we take into account the total effective lagrangian as follows [27-34]:

$$\mathcal{L}_{eff} = \mathcal{L}_{SM} + \sum_n \frac{f_n}{\Lambda^2}\,\mathcal{O}_n + \ \ldots \quad (5)$$

Here, the first term is the SM lagrangian of dimension four and the second term constitutes the contribution of new physics which deviations in the HV_1V_2 couplings $(V_i = W, Z, \gamma)$ from SM predictions. Also , $\mathcal{O}_n$'s are the operators that consist of Higgs-boson fields or vector-boson, Λ is the scale of new physics and f_n denote non-standard couplings Taking into account the $\mathcal{O}_n$ operators to be P and C even, there are five dimension- six operators that alter the Higgs boson couplings to γ and Z. The exact expressions of these operators can be found in [27, 28, 34]. They are given as:

$O_{ww} = \phi^t\, W\mu\nu\, W^{\mu\nu}\, \phi$
$O_W = (D_\mu \phi)^+\, W^{\mu\nu}\, (D_\nu \phi)$
$O_{BB} = \phi^t B_{\mu\nu} B^{\mu\nu} \phi$

$O_B = (D_\mu \phi)^+ B^{\mu\nu} (D_\nu \phi)$

$O_{BW} = \phi^t B_{\mu\nu} W^{\mu\nu} \phi$ (6)

where ϕ is the scalar doublet, $D_\mu$is the covariant derivative, $W_{\mu\nu} = i\frac{g}{2}(\vec{\sigma}.\overrightarrow{W_{\mu\nu}})$ and $B_{\mu\nu} = i\frac{g'}{2}\overrightarrow{B_{\mu\nu}}$. Here g and g' are the $SU(2)_L$ and $U(1)_Y$ gauge couplings. And σ are the pauli matrices.

After electroweak symmetry breaking the effective lagrangian written for the new physics in Eq. (5) is expressed with the physical fields. Taking into account HZγ and Hγγ vertices, it can be expressed as follows:

$$\mathcal{L}_{eff}^{(NP)} = g_{H\gamma\gamma} H A_{\mu\nu} A^{\mu\nu} + g_{HZ_\gamma}^{(1)} A_{\mu\nu} Z^{\mu} \partial^{\nu} H + g_{HZ_\gamma}^{(2)} H A_{\mu\nu} Z^{\mu\nu} \quad (7)$$

where $V_{\mu\nu} = \partial_\mu V_\nu - \partial_\nu V_\mu$ with Z field and V=A (photon) . $g_{H\gamma\gamma}$, $g_{HZ_\gamma}^{(1)}$ and $g_{HZ_\gamma}^{(2)}$ are the non-standard couplings which involve f_n appearing in the effective lagrangian (5) before symmetry breaking as;

$$g_{H\gamma\gamma} = -\left(\frac{g_{mw}}{\Lambda^2}\right) \sin\theta_w^2 \left(\frac{f_{BB+} f_{ww-f_{Bw}}}{2}\right)$$
$$g_{HZ\gamma}^1 = \left(\frac{g_{mw}}{\Lambda^2}\right) \sin\theta_w \left(\frac{f_w - f_B}{2\cos\theta_w}\right)$$
$$g_{HZ\gamma}^2 = \left(\frac{g_{mw}}{\Lambda^2}\right) \frac{\sin\theta_w}{2\cos\theta_w} \left[2\sin\theta_w^2 f_{BB-} 2\cos\theta_w^2 f_{ww} + (\cos\theta_w^2 - \sin\theta_w^2) f_{Bw}\right] \quad (8)$$

where s= $\sin\theta_w$, c= $\cos\theta_w$, θ_w is the Weinberg angle and m_w is the mass of the W boson.

Hγγ and HZγ vertices disappear at the tree-level in the SM but they appear at one-loop level. At high energies ($\sqrt{s} \gg m_H$) these one-loop contributions can be expressed with the following effective lagrangian [35, 36]:

$$\mathcal{L}_{eff}^{(SM)} = g_{H\gamma\gamma}^{(SM)} H A_{\mu\nu} A^{\mu\nu} + g_{HZ_\gamma}^{(SM)} H A_{\mu\nu} Z^{\mu\nu} \quad (9)$$

where, $g_{H\gamma\gamma}^{(SM)} = \frac{2\alpha}{9\pi\nu}$ and $g_{HZ_\gamma}^{(SM)} = \frac{\alpha}{4\pi\nu\sin\theta_W}(5.508 - 0.004i)$. Here, ν is the electroweak vacuum expectation value and α is the fine structure constant. Therefore during the calculations we consider;

$$\mathcal{L}'_{eff} = \mathcal{L}_{eff}^{(SM)} + \mathcal{L}_{eff}^{(NP)} = g'_{H\gamma\gamma} H A_{\mu\nu} A^{\mu\nu} + g_{HZ_\gamma}^{\prime(1)} A_{\mu\nu} Z^{\mu} \partial^{\nu} H + g_{HZ_\gamma}^{\prime(2)} H A_{\mu\nu} Z^{\mu\nu} \quad (10)$$

where

$$g'_{H\gamma\gamma} = g_{H\gamma\gamma} + g_{H\gamma\gamma}^{(SM)}$$
$$g_{HZ_\gamma}^{\prime(1)} = g_{HZ_\gamma}^{(1)}$$
$$g_{HZ_\gamma}^{\prime(2)} = g_{HZ_\gamma}^{(2)} + g_{HZ_\gamma}^{(SM)} \quad (11)$$

The decay width of H→ Zγ and H→ γγ can be expressed in the terms of $g'_{H\gamma\gamma}$, $g_{HZ_\gamma}^{\prime(1)}$ and $g_{HZ_\gamma}^{\prime(2)}$ as follows:

$$\Gamma_{\gamma\gamma} = \frac{g_{H\gamma\gamma}^{\prime 2} m_H^3}{4\pi} \quad (12)$$

$$\Gamma_{Z\gamma} = (g_{H\,z\gamma}^{\prime(1)} + 2g_{H\,z\gamma}^{\prime(2)})^2 \frac{(m_H^2 - m_z^2)^3}{32\pi m_H^3} \quad (13)$$

In Figure 2- Figure 4, taking into account H→Zγ decay of the produced Higgs bosons, the cross section of main process pp →pγγp →pHp→ pZγp is plotted as a function of non-standard couplings $g_{H\gamma\gamma}$, $g_{HZ_\gamma}^{(1)}$ and $g_{HZ_\gamma}^{(2)}$ for the kinematically allowed interval of 0< ξ <1-$\frac{m_p}{E_p}$ and for 0.015< ξ <0.15 and 0.0015< ξ <0.5.

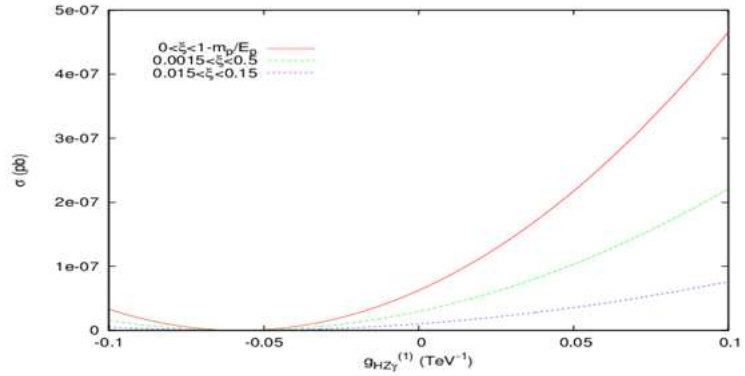

Figure 2. The cross section of pp →pγγp →pHp→ pZγp as a function of the non-standard $g_{HZ\gamma}^{(1)}$ coupling at a 100 TeV collider. Other non-standard couplings are assumed to be zero.

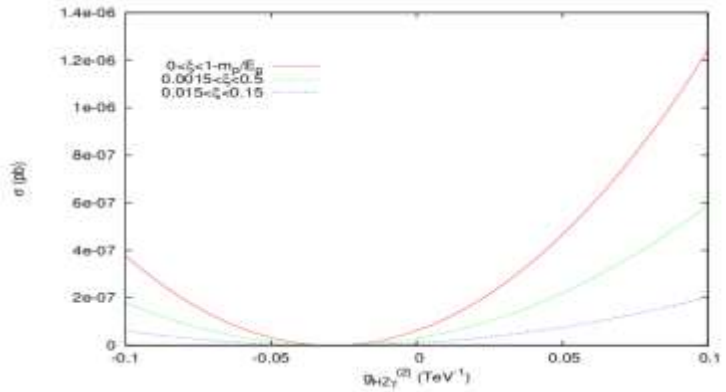

Figure 3. The cross section of pp →pγγp →pHp→ pZγp as a function of the non-standard $g_{HZ\gamma}^{(2)}$ coupling at a 100 TeV collider. Other non-standard couplings are assumed to be zero.

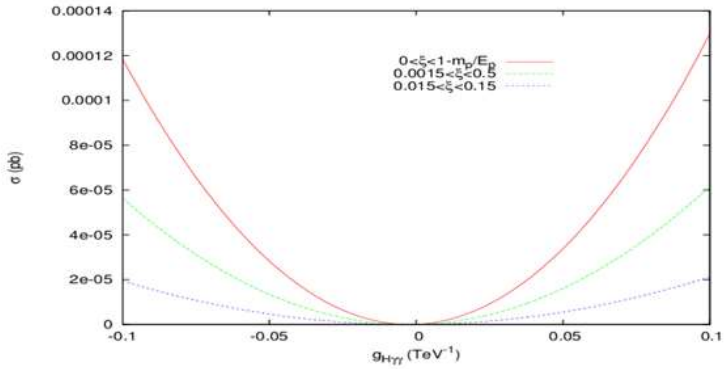

Figure 4. The cross section of pp →pγγp →pHp→ pZγp as a function of the non-standard $g_{H\gamma\gamma}$ coupling at a 100 TeV collider. Other non-standard couplings are assumed to be zero.

Similarly, in Figure 5, taking into account H→γγ decay and the same acceptances mentioned above, we plot the cross section of main process pp →pγγp →pHp→ pγγp as a function of non-standard $g_{H\gamma\gamma}$ coupling.

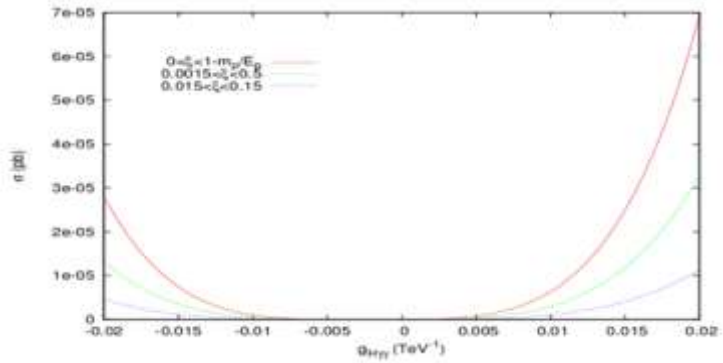

Figure 5. The cross section of pp →pγγp →pHp→ pγγp as a function of the non-standard $g_{H\gamma\gamma}$ coupling at a 100 TeV collider. Other non-standard couplings are assumed to be zero.

In Figure 2- Figure 5, the cross section for the whole region (0< ξ <1- $\frac{m_p}{E_p}$) increases more rapidly as a function of non-standard coupling comparing with the those for forward detector acceptances. This is reasonable since, the initial γγ system's center-of-mass energy increases as the ξ interval increases. In order to obtain a definite result we perform a statistical analysis. We use Poisson analysis because the SM events' number is less than 1. Then we obtain 95% C.L. sensitivity constraints on non-standard coupling parameters. For the number of events we use the formula $N = \sigma \times L_{int}$, where σ is the cross section given in Eq.(3) and L_{int} is the integrated luminosity. The process, pp →pγγp →pHp→ pγγp receives contributions only Hγγ from vertex. Therefore, in this case only non-standard $g_{H\gamma\gamma}$ coupling is restricted. The corresponding bounds on $g_{H\gamma\gamma}$ is given in Figure 6 for future 100 TeV proton-proton collider with $L_{int} = 3000\ fb^{-1}$.

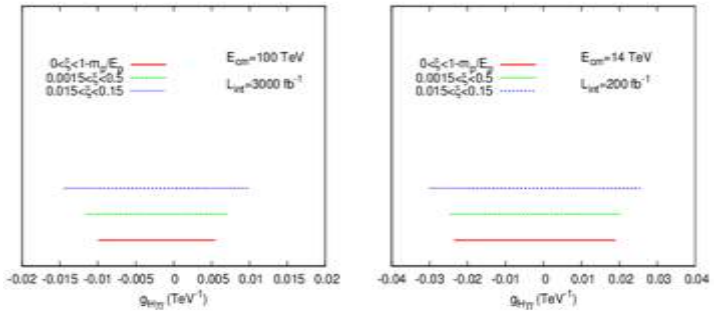

Figure 6. In the left panel 95% C.L. sensitivity constraints on the coupling $g_{H\gamma\gamma}$ are given for the $\sqrt{s} = 100\ TeV$ and $L_{int} = 3000\ fb^{-1}$. In the right panel, for the LHC ($\sqrt{s} = 14\ TeV,\ L_{int} = 200 fb^{-1}$) similar constraints are given. H→γγ decay channel is considered as the signal.

This luminosity value has been proposed for future 100 TeV proton-proton collider and used in similar studies. For example, see [1]. For a comparison, we do a similar analysis for the LHC ($\sqrt{s} = 14\ TeV, L_{int} = 200 fb^{-1}$). However, the process pp →pγγp →pHp→ pZγp receives contributions both from Hγγ and HZγ vertices. Therefore, in this case we have to analyze three independent couplings $g_{H\gamma\gamma}, g^{(1)}_{HZ\gamma}$ and $g^{(2)}_{HZ\gamma}$. For simplicity, we assume that only two of the couplings are free but the remaining one is zero. In Figure 7- Figure 9, we present 95% C.L. constraints on $g^{(2)}_{HZ\gamma} - g_{H\gamma\gamma}, g^{(1)}_{HZ\gamma} - g_{H\gamma\gamma}$ and $g^{(2)}_{HZ\gamma} - g^{(1)}_{HZ\gamma}$ respectively.

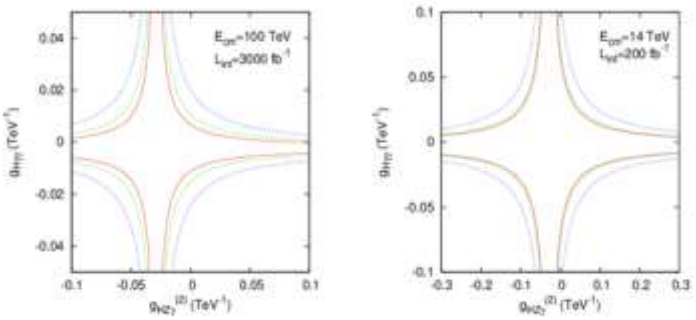

Figure 7. The 95% C.L. sensitivity constraints on $g^{(2)}_{HZ\gamma} - g_{H\gamma\gamma}$ for 100 TeV pp collider (left panel) and LHC (right panel). H→Zγ decay channel is considered as the signal. The solid line shows the bounds for the whole interval 0< ξ <1- $\frac{m_p}{E_p}$. The dotted and dashed lines indicate the bounds for 0.015< ξ <0.15 and 0.0015< ξ <0.5 , respectively.

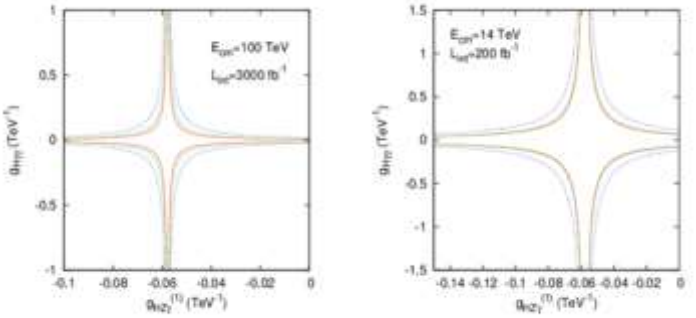

Figure 8. The 95% C.L. sensitivity constraints on $g^{(1)}_{HZ\gamma} - g_{H\gamma\gamma}$ for 100 TeV pp collider (left panel) and LHC (right panel). H→Zγ decay channel is considered as the signal. The solid line shows the bounds for the whole interval 0< ξ <1- $\frac{m_p}{E_p}$. The dotted and dashed lines indicate the bounds for 0.015< ξ <0.15 and 0.0015< ξ <0.5 respectively.

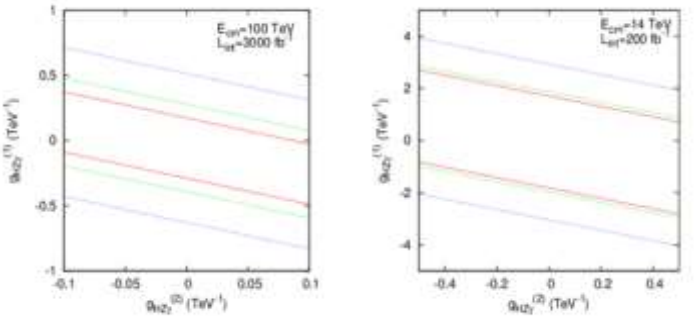

Figure 9. The 95% C.L. sensitivity constraints on $g^{(2)}_{HZ\gamma} - g^{(1)}_{HZ\gamma}$ for 100 TeV pp collider (left panel) and LHC (right panel). H→Zγ decay channel is considered as the signal. The solid line shows the bounds for the whole interval 0< ξ <1- $\frac{m_p}{E_p}$. t The dotted and dashed lines indicate the bounds for 0.015< ξ <0.15 and 0.0015< ξ <0.5, respectively.

3. Conclusions

We investigate the potential of the exclusive single Higgs boson production process at a future 100 TeV proton-proton collider to examine non-standard HZγ and Hγγ couplings. We get the sensitivity constraints on them and compare with the corresponding constraints of LHC. We observe from Figure

6 that future 100 TeV proton-proton collider with integrated luminosity of $L_{int} = 3000\ fb^{-1}$ enable us to improve sensitivities on non-standard Higgs bounds by roughly a factor of 2.5 with respect to LHC. Also in Figure 7-Figure 9 one can simply see that at a future 100 TeV proton-proton collider the sensitivity bounds on these couplings are roughly 4.5 times better than LHC limits. Thus, we conclude that a considerable improvement is achieved at a future 100 TeV proton-proton collider to probe non-standard Higgs constraints.

References

[1] Arkani-Hamed N., Han T., Mangano M., Wang L.T. 2016. Physics Opportunities of a 100 TeV Proton-Proton Collider. Physics Reports, 652: 1-49.

[2] Mangano M.L., Zanderighi G., Aguilar Saavedra J.A., Alekhin S., Badger S., Bauer C.W., Becher T., Bertone V., Bonvini M., Boselli S., Bothmann E., et al. 2017. Physics at the FCC-hh, a 100 TeV pp collider. Cern Yellow Report, 3: 1-254.

[3] Contino R., Curtin D., Katz A., Mangano M.L., Panico G., Ramsey-Musolf M.J., Zanderighi G., Anastasiou C., Astill W., Bambhaniya G., et al. 2017. Physics at a 100 TeV pp collider: Higgs and EW symmetry breaking studies. Cern Yellow Report, 3: 255-440.

[4] Aad G., Abajyan T., Abbott B., Abdallah J., Abdel Khalek S., Abdelalim A.A., Abdinov O., Aben R., Abi B., Abolins M., et al. 2012. Observation of a new particle in the search for the Standard Model Higgs boson with the ATLAS detector at the LHC. Physics Letters B, 716: 1-29.

[5] Chatrchyan S., Kharchatryan V., Sirunyan A.M., Tumasyan A., Adam W., Aguilo E., Bergauer T., Dragicevic M., Erö J., Fabjan C., et al. 2012. Observation of a new boson at a mass of 125 GeV with the CMS experiment at the LHC. Physics Letters B, 716: 30-61.

[6] Taheri Monfared S., Fayazbakhsh S., Mohammadi Najafabadi M. 2016. Exploring anomalous HZγ couplings in γ-proton collisions at the LHC. Physics Letters B, 762: 301-308.

[7] Cao O.H., Li G., Yan B., Zhang D.M., Zhang H. 2016. New measurement of antineutrino oscillation with the full detector configuration at Daya Bay. Physical Review Letters, 115: 11.

[8] Barr A.J., Dolan M.J., Englert C., Ferreira de Lima D.E., Spannowsky M. 2015. Future of High Energy Physics; The - Some Aspects. Journal of High Energy Physics, 1502: 016.

[9] Degrande C., Khoze V.V., Mattelaer O. 2016. Multi-Higgs-boson production in gluon fusion at 100 TeV. Physical Review D, 94: 085031.

[10] Fuks B., Kim J.H., Lee S.J. 2016. Multi-Higgs Production and Unitarity in Vector-Boson Fusion at Future Hadron Colliders. Physical Review D, 93: 035026.

[11] Baglio J., Djouadi A., Quevillon J. 2016. Prospects for Higgs physics at energies up to 100 TeV. Reports on Progress in Physics, 79: 116201.

[12] Papaefstathiou A., Sakurai K. 2016. Future of High Energy Physics; The - Some Aspects. Journal of High Energy Physics, 1602: 006.

[13] Albrow M.G., DeRoeck A., Khoze V.A., Lämsä J., Norbeck E., Onel Y., Orava R., Ryskin M.G. 2009. Forward physics with rapidity gaps at the LHC. Journal of Instrumentation, 4: P10001.

[14] Albrow M.G., Appleby R.B., Arneodo M., Atoian G., Azhgirey I.L., Barlow R., Bayshev I.S., Beaumont W., Bonnet L., Brandt A. 2009. The FP420 R&D project: Higgs and New Physics with forward protons at the LHC. Journal of Instrumentation, 4: T10001.

[15] ATLAS Collaboration. 2011. Letter of Intent for the Phase-I Upgrade of the ATLAS Experiment. CERN-LHCC-2011-012.

[16] CMS and TOTEM collaboration. 2014. CMS-TOTEM Precision Proton Spectrometer. CERN-LHCC-2014-021.

[17] Chatrchyan S., Kharchatryan V., Sirunyan A.M., Tumasyan A., Adam W., Aguilo E., Bergauer T., Dragicevic M., Erö J., Fabjan C., et al. 2012. Exclusive photon-photon production of muon pairs in proton-proton collisions at sqrt(s) = 7 TeV. Journal of High Energy Physics, 1201: 052.

[18] Chatrchyan S., Kharchatryan V., Sirunyan A.M., Tumasyan A., Adam W., Aguilo E., Bergauer T., Dragicevic M., Erö J., Fabjan C., et al. 2012. Search for exclusive or semi-exclusive γγ production and observation of exclusive and semi-exclusive e^+e^- production in pp collisions at s√=7s=7 TeV. Journal of High Energy Physics, 1211: 080.

[19] Chatrchyan S., Kharchatryan V., Sirunyan A.M., Tumasyan A., Adam W., Aguilo E., Bergauer T., Dragicevic M., Erö J., Fabjan C., et al. 2013. Differential branching fraction and angular analysis of the decay. Journal of High Energy Physics, 1307: 116.

[20] Khachatryan V., Sirunyan A.M., Tumasyan A., Adam W., Asilar E., Bergauer T., Brandstetter J., Brondolin E., Dragicevic M., Erö J. et al. 2016. Evidence for exclusive $\gamma\gamma \rightarrow W + W -$ production and constraints on anomalous quartic gauge couplings in pp collisions at $s\sqrt{=7}$ and 8 TeV. Journal of High Energy Physics, 1608: 119.

[21] Aaboud M., Aad G., Abbott B., Abdallah J., Abdinov O., Abeloos B., Aben R., AbouZeid O.S., Abraham N.L., Abramowicz H. 2016. Measurement of exclusive gamma gamma -> W+W- production and search for exclusive Higgs boson production in pp collisions at root s=8 TeV using the ATLAS detector. Physical Review D, 94: 032011.

[22] Abulencia A., Adelman J., Affolder T., Akimoto T., Albrow M.G., Ambrose D., Amerio S., Amidei D., Anastassov A., Anikeev K. et al. 2007. Observation of Exclusive Electron-Positron Production in Hadron-Hadron Collisions. Physical Review Letters, 98: 112001.

[23] Aaltonen T., Adelman J., Akimoto T., Albrow M.G., Alvarez Gonzalez B., Amerio S., Amidei D., Anastassov A., Annovi A., Antos J. et al. 2009. Search for Exclusive Z-Boson Production and Observation of High-Mass $p^{-}p \rightarrow p\gamma\gamma^{-}p \rightarrow pl+l-^{-}p$ Events in $p^{-}p$ Collisions at $\sqrt{s}$=1.96 TeV. Physical Review Letters, 102: 222002.

[24] Aaltonen T., Adelman J., Akimoto T., Albrow M.G., Alvarez Gonzalez B., Amerio S., Amidei D., Anastassov A., Annovi A., Antos J. et al. 2009. Observation of exclusive charmonium production and $\gamma\gamma \rightarrow \mu + \mu -$ in $p\bar{p}$ collisions at s=1.96 TeV. Physical Review Letters, 102: 242001.

[25] Barger V., Ishida M., Keung W.Y. 2012. Total width of 125 GeV Higgs boson. Physical Review Letters, 108: 261801.

[26] Tasevsky M. 2015. AIP Conference Proceedings: Status of the AFP project in the ATLAS experiment, Cern, Geneva, Switzerland. 8 December 2014; Institute of Physics, Academy of Sciences of the Czech Republic: Na Slovance, Prague, Czech Republic, p. 4.

[27] Buchmuller W., Wyler D. 1986. Effective lagrangian analysis of new interactions and flavour conservation. Nuclear Physics B, 268: 621-653.

[28] Corbett T., Eboli O.J.P., Gonzalez-Fraile J., Gonzalez-Garcia M.C. 2012. Constraining anomalous Higgs interactions. Physical Review D, 86: 075013.

[29] Corbett T., Eboli O.J.P., Gonzalez-Fraile J., Gonzalez-Garcia M.C. 2013. Robust Determination of the Higgs Couplings: Power to the Data. Physical Review D, 87: 015022.

[30] Masso E., Sanz V. 2013. Limits on anomalous couplings of the Higgs boson to electroweak gauge bosons from LEP and the LHC. Physical Review D, 87: 033001.

[31] De Rujula A., Gavela M.B., Hernandez P., Masso E. 1992. The Selfcouplings of vector bosons: Does LEP-1 obviate LEP-2. Nuclear Physics B, 384: 3-58.

[32] Hagiwara K., Ishihara S., Szalapski R., Zeppenfeld D. 1993. Low energy effects of new interactions in the electroweak boson sector. Physical Review D, 48: 2182-2203.

[33] Gonzalez-Garcia M.C. 1999. Anomalous Higgs Couplings. International Journal of Modern Physics A, 14: 3121-3156.

[34] Leung C.N., Love S.T., Rao S.Z. 1986. Low-energy manifestations of a new interactions scale: Operator analysis. Physics C, 31**:** 433-437.

[35] Donoghue J.F., Golowich E., Holstein B.R. 1992. Dynamics of the Standard Model. Edited by Cambridge University Press, UK, 201.

[36] Farina M., Grossman Y., Robinson D.J. 2015. Probing CP Violation in $h \rightarrow Z\gamma$ with Background Interference. Physical Review D, 92: 073007.

Araştırma Makalesi / Research Article

Proton-proton Collision at High Energies

Mohsun ALIZADE*, Azar AHMADOV

Baku State University, Department of Theoretical Physics, Baku, Azerbaijan
(ORCID: 0000-0002-9664-5465) (ORCID: 0000-0003-0662-5549)

Abstract
The presented work effective section of neutralino birth calculated for proton-proton collision at high energies. Proton-proton collision is considered in parton model and Feynman diagram was used in calculations. One of possible process: a process with γ photon formation was considered. It is shown that an effective section of process with unpolarized and polarized protons is different. The ratio of effective sections of process with unpolarized and polarized protons is $1-\lambda_1\lambda_2$. The energy spectrum of neutralino born has been studied. The spectrum has an asymmetric shape and is shallow towards lower energies. The maximum value of the spectrum increases exponentially as the energy of proton collision increases.

Keywords: Proton-proton collision, Polarization, Quarks, Feynman diagram, Cross section, Phase volume.

Yüksek Enerjilerde Proton-proton Çarpışması

Öz
Bu çalışmada yüksek enerjili proton-proton çarpışmalarında nötrino oluşumunun etkin kesiti hesap edilmiştir. Proton-proton çarpışmaları parton modeli ile incelenmiş ve hesaplarda Feynman diyagramları uygulanmıştır. Mümkün proseslerden birisi olarak γ foton oluşumu dikkate alınmıştır. Kutuplaşmış ve kutuplaşmamış protonlarla gerçekleşen proseslerin etkin kesitlerinin farklı olduğu gösterilmiştir. Bu iki etkin kesitlerin oranının $1-\lambda_1\lambda_2$ olduğu belirlenmiştir. Nötrino oluşumunun enerji spektrumu incelenmiştir. Spektrumun asimetrik şekile sahip olduğu ve yüksek enerjilere doğru daraldığı görülmüştür. Proton çarpışma enerjisi yükseldikce spektrumun maksimum değerinin eksponansiyel olarak yükseldiği belirlenmiştir.

Anahtar kelimeler: Proton proton çarpışması, Kutuplaşma, Kuark, Feynman'ın diagramı, Etkili bir oran, Faz hacim.

1. Introduction

At present work proton - proton collisions in quark model is investigated. These investigations give the possibility will receive information on properties of quarks, on the nature of the gluon field, and etc. At very high energies, the proton turns out to be filled mainly with gluons, and quarks and antiquarks in it are noticeably smaller. Protons and antiprotons in such conditions look almost the same, and therefore there is no special difference what to push protons with protons (as on LHC) or protons with antiprotons (as on the Tevatron Collider) [1-3].

When two protons collide, it does not necessarily mean that each parton hits something inside the oncoming proton. Usually everything is simpler one quark from one proton collides with someone from an oncoming proton, and the rest of the partons just fly by. Occasionally occurs especially hard process in which the colliding bullets get a strong cross shot. These cartridges are emitted with a large transverse momentum. Sometimes there is a hard collision, and then in addition to the standard hadrons background fly narrow streams of high-energy hadrons - hadrons jets [4-7].

*Sorumlu yazar:mohsunalizade@yahoo.com
Geliş Tarihi: 20.10.2019, Kabul Tarihi: 19.12.2019

Processing the results of proton-proton collisions on hadrons colliders and comparing them with theoretical predictions also has its own peculiarities in comparison with other types of colliders. They relate to the following two aspects [1-4]:

1. In a typical collision of two protons, many (several tens) hadrons are born, many of them flying out at very small angles and avoiding detection ("flying into the tube"). Catch brand all born particles, and especially to recover some of them born, rarely.
2. Theoretical calculations are usually carried out at the level of cartridges, and hadrons are detected in the experiment. The process of transformation of a set of cartridges into a set of hadrons is not yet amenable to theoretical calculations from first principles. It has to be modeled based on both the theory and the data of previous experiments. Therefore, the connection between theory and experiment is not as direct as, for example, in electron-positron collisions.

The collision of spin-polarized protons leads to the formation of pines - neutral particles, the trajectory of which depends on the properties of gluons in the proton [8-10].

In angular moment the proton exists and the third component is the contribution of orbital angular moment. The physical meaning of this magnitude is that, like electrons in an atom, gluons and quarks can rotate within a proton. It is much more difficult to estimate this value experimentally. In addition, theoretical physicists are ambiguous in their interpretation of this value, which has caused serious disputes in the scientific environment It is known that the effect of higher-order contributions to cross section usually increases with increment of colliding energy and would be more significant at very high energies

In the experiment, scientists encountered proton beams with clearly defined spin directions. In the first series of collisions, the backs in the tufts were co-directed. One of the tufts was then "turned over" and monitored for how the nature of the fragments changed from particle collision. In particular, physicists monitored the rate of birth in the collisions of neutral pioneers. Gluons are actively involved in this process, so if their contribution to proton spin is significant, beam "preloading" will lead to significant changes in the properties of the pines - their pulses and paths [11,12].

Spin is one of the most fundamental properties of elementary particles. This dictates symmetry behavior in space-time transformation. This is additional, so in high-energy experiments it is possible to use degrees of freedom to study, aspects of the interaction of elementary particles that we will not be able to study in experiments with non-polarized particle [13].

Experimental search for supersymmetric particles is one of the main tasks of the experimental program on hadron colliders, especially on the Large Hadron Collider (LHC), after the recent discovery of the Higgs boson with a mass of about 126 GeV is consistent with the MSSM-predicted range for the mass of the lightest Higgs scalar h_0 [14,15].

Among all supersymmetric models, the minimum supersymmetric standard model (MSSM) is one of the most motivated and well-studied extensions of the standard model. MSSM predicts many new particles such as Sleeptons, Squares, gluinos, light/heavy neutral scalar (CP-even) higgs bosons, pseudoscalar (CP-odd) Higgs boson A_0, and a pair of charged Higgs bosons, four neutrally and two chargino. Moreover, pair production of neutralino/chargino begins to be questioned as a channel of discovery of supersymmetry [16,17].

At present work we considered unpolarized and polarized proton collision with birth of neutralino. Calculated effective section of neutralino formation and its energy spectrum.

2. Calculations

We considered reaction of collision of protons in two cases: a) process unpolarized protons, b) process polarized protons (figure 1), found her effective section, phase volume is analyzed.

2.1. Process Production of Neutralino at Collision of UnpolarizedProtons (fig.1a)

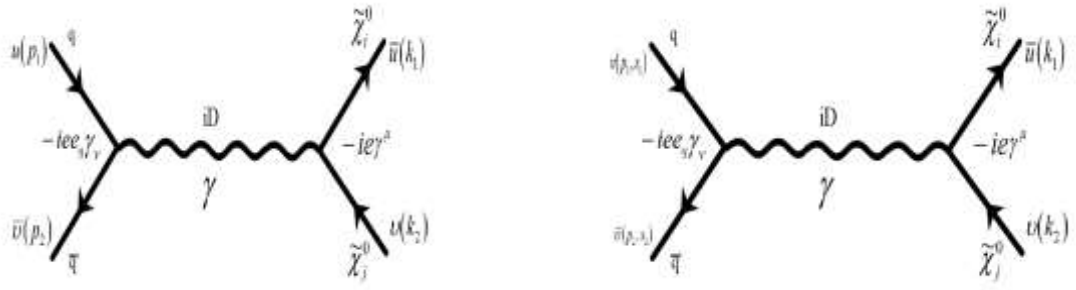

a *b*

Figure 1. Feynman diagram of process of collision unpolarized protons (a) and polarized protons (b) with the formation neutralino

We denote p_1, p_2, q_1, q_2 - pulses of initial and final particles. m_1, m_2 - mass of initial particles, M_{q_1}, M_{q_2} - mass of washed-up particles.

$$pp \to \tilde{\chi}_i^0 \tilde{\chi}_j^0; \quad (i, j = 1,2)$$
$$q(p_1)\bar{q}(p_2) \to \tilde{\chi}_i^0(k_1)\tilde{\chi}_j^0(k_2), \quad (i, j = 1,2,3,4)$$

Mandelstam's variables are:

$$s = (p_1 + p_2)^2 = (k_1 + k_2)^2$$
$$t = (p_1 - k_1)^2 = m_{\tilde{\chi}_i^0}^2 - 2p_1k_1 \Rightarrow 2p_1k_1 = \left(m_{\tilde{\chi}_i^0}^2 - t\right)$$
$$u = (p_1 - k_2)^2 = m_{\tilde{\chi}_j^0}^2 - 2p_1k_2 \Rightarrow 2p_1k_2 = \left(m_{\tilde{\chi}_j^0}^2 - u\right)$$

Propagator of this process is: $iD = \dfrac{-i}{k^2 + i\varepsilon}\left[g_{\mu\nu} + \dfrac{(\xi - 1)k_\mu k_\nu}{k^2}\right]$. All calculation has been carried out in Feynman calibration: $\xi = 1 \Rightarrow iD = \dfrac{-ig_{\mu\nu}}{k^2}$.

In this case transition matrix of process will be:

$$M = \bar{u}(k_1)(-ie\gamma^\mu)\upsilon(k_2)\left(\frac{-ig_{\mu\nu}}{k^2}\right)\bar{\upsilon}(p_2)(-iee_q\gamma_\nu)u(p_1) = \frac{ie^2e_q}{k^2}\left[\bar{u}(k_1)\gamma^\mu\upsilon(k_2)\right]\left[\bar{\upsilon}(p_2)\gamma_\nu u(p_1)\right]g_{\mu\nu}$$

and Hermit conjugate of *M* will be:

$$M^+ = \frac{-ie^2e_q}{k^2}\left[\bar{\upsilon}(k_2)\gamma_{\mu'}u(k_1)\right]\cdot\left[\bar{u}(p_1)\gamma_{\nu'}\upsilon(p_2)\right]g_{\mu'\nu'}$$

Then

$$|M|^2 = MM^+ = \frac{e^4e_q^2}{k^4}\left[\bar{u}(k_1)\gamma^\mu\upsilon(k_2)\right]\cdot\left[\bar{\upsilon}(p_2)\gamma_\nu u(p_1)\right]g_{\mu\nu}\left[\bar{\upsilon}(k_2)\gamma_{\mu'}u(k_1)\right]\cdot\left[\bar{u}(p_1)\gamma_{\nu'}\upsilon(p_2)\right]g_{\mu'\nu'}$$

We denote: $u(k_1)\bar{u}(k_1)=\left(\hat{k}_1+m_{\tilde{\chi}_i^0}\right)$, $u(p_1)\bar{u}(p_1)=\frac{1}{2}(\hat{p}_1+m_1)$, $\upsilon(k_2)\bar{\upsilon}(k_2)=\left(\hat{k}_2-m_{\tilde{\chi}_j^0}\right)$, $\upsilon(p_2)\bar{\upsilon}(p_2)=\frac{1}{2}(\hat{p}_2-m_2)$ and moreover at high energies $E>>m$ particles can be considered massless ($m_1=0; m_2=0$)then obtain:

$$|M|^2=\frac{e^4e_q^2}{4k^4}\left[\gamma^\mu\hat{k}_2\gamma_{\mu'}\hat{k}_1-m_{\tilde{\chi}_j^0}\gamma^\mu\gamma_{\mu'}\hat{k}_1+\gamma^\mu\hat{k}_2m_{\tilde{\chi}_i^0}\gamma_{\mu'}-m_{\tilde{\chi}_j^0}\gamma^\mu m_{\tilde{\chi}_i^0}\gamma_{\mu'}\right]\cdot\left[\gamma^\mu\hat{p}_1\gamma_{\mu'}\hat{p}_2\right]$$

Knowing that: $Tr\left[\gamma^\mu\gamma^\mu\gamma^\mu\right]=0$ and $\hat{k}_1=\gamma_\mu k_1$ obtain following expression:

$$|M|^2=\frac{2e^4e_q^2}{k^4}\left[4(p_1k_2)(p_2k_1)+4(k_2p_2)(k_1p_1)+2m_{\tilde{\chi}_j^0}m_{\tilde{\chi}_i^0}(p_1p_2)\right]=$$

In the last expression we denote: $2p_1k_2=\left(m^2_{\tilde{\chi}_j^0}-u\right)$, $2p_2k_1=\left(m^2_{\tilde{\chi}_i^0}-u\right)$, $2k_2p_2=\left(m^2_{\tilde{\chi}_j^0}-t\right)$, $2k_1p_1=\left(m^2_{\tilde{\chi}_i^0}-t\right)$, $2(p_1p_2)=s$ finally obtain:

$$|M|^2=\frac{2e^4e_q^2}{k^4}\left[\left(m^2_{\tilde{\chi}_j^0}-u\right)\left(m^2_{\tilde{\chi}_i^0}-u\right)+\left(m^2_{\tilde{\chi}_j^0}-t\right)\left(m^2_{\tilde{\chi}_i^0}-t\right)+m_{\tilde{\chi}_j^0}m_{\tilde{\chi}_i^0}s\right] \quad (1)$$

Differential cross section of collision is:

$$\frac{d\sigma}{dQ}=N_c\frac{\delta_{ij}g^4\lambda_{ij}}{2304\pi^2s^2}|M|^2$$

where

$$\lambda_{ij}=\frac{1}{2}\sqrt{\left(s-m^2_{\tilde{\chi}_i^0}-m^2_{\tilde{\chi}_j^0}\right)^2-4m^2_{\tilde{\chi}_i^0}m^2_{\tilde{\chi}_j^0}}$$

After integration we obtain:

$$\sigma=\frac{\lambda_{ij}}{1152\pi^2s^2}|M|^2\int_{-\pi}^{\pi}\sin\theta d\theta\int_0^{2\pi}d\varphi$$

In the end we obtain

$$\sigma=\frac{\lambda_{ij}}{288\pi s^2}|M|^2 \quad (2)$$

2.2. Process Production of Neutralino at Collision of Polarized Protons (fig.1b)

$$pp\to\tilde{\chi}_i^0\tilde{\chi}_j^0 \;;\; (i,j=1,2)$$
$$q(p_1,s_1)\bar{q}(p_2,s_2)\to\tilde{\chi}_i^0(k_1)\tilde{\chi}_j^0(k_2) \;;\; (i,j=1,2,3,4)$$

We use the definition of Mandelstam's variables, propagator and Feynman calibration as in section *a*, and polarization of protons was been taked as [18].
Thus transition matrix of process is:

$$M_{pol}=\bar{u}(k_1)(-ie\gamma^\mu)\upsilon(k_2)\left(\frac{-ig_{\mu\nu}}{k^2}\right)\bar{\upsilon}(p_2,s_2)(-iee_q\gamma_\nu)u(p_1,s_1)=\frac{ie^2e_q}{k^2}\left[\bar{u}(k_1)\gamma^\mu\upsilon(k_2)\right]\cdot\left[\bar{\upsilon}(p_2,s_2)\gamma_\nu u(p_1,s_1)\right]g_{\mu\nu}$$

and correspondingly Hermit conjugate of $M_{pol}$is

$$M^{+}_{pol} = \frac{-ie^2 e_q}{k^2}\left[\bar{\upsilon}(k_2)\gamma_{\mu'}u(k_1)\right]\cdot\left[\bar{u}(p_1,s_1)\gamma_{\nu'}\upsilon(p_2,s_2)\right]g_{\mu'\nu'}$$

$$|M|^{+}_{pol} = M_{pol}M^{+}_{pol} = \frac{e^4 e_q^2}{k^4}\left[\bar{u}(k_1)\gamma^{\mu}\upsilon(k_2)\right]\cdot\left[\bar{\upsilon}(p_2,s_2)\gamma_{\nu}u(p_1,s_1)\right]g_{\mu\nu}\left[\bar{\upsilon}(k_2)\gamma_{\mu'}u(k_1)\right]\cdot\left[\bar{u}(p_1,s_1)\gamma_{\nu'}\upsilon(p_2,s_2)\right]g_{\mu'\nu'}$$

We denote: $u(k_1)\bar{u}(k_1) = \left(\hat{k}_1 + m_{\tilde{\chi}^0_i}\right)$, $u(p_1,s_2)\bar{u}(p_1,s_2) = \frac{1}{2}(1-\lambda_1\gamma_5)\hat{p}_1$,

$\upsilon(k_2)\bar{\upsilon}(k_2) = \left(\hat{k}_2 - m_{\tilde{\chi}^0_j}\right)$, $\upsilon(p_2,s_2)\bar{\upsilon}(p_2,s_2) = \frac{1}{2}(1+\lambda_2\gamma_5)\hat{p}_2$

$$|M|^2_{pol} = \frac{e^4 e_q^2}{4k^4}\left[\gamma^{\mu}\left(\hat{k}_2 - m_{\tilde{\chi}^0_j}\right)\gamma_{\mu'}\left(\hat{k}_1 + m_{\tilde{\chi}^0_i}\right)\right]\cdot\left[\gamma^{\mu}(1-\lambda_1\gamma_5)\hat{p}_1\gamma_{\mu'}(1+\lambda_2\gamma_5)\hat{p}_2\right]$$

Athighenergies $E >> m$ particles can be consideredmassless ($m_1 = 0; m_2 = 0$) and take into account $Tr\left[\gamma^{\mu}\gamma^{\mu}\gamma^{\mu}\right] = 0$ and $\hat{k}_1 = \gamma_{\mu}k_1$ obtain following expression:

$$|M|^2_{pol} = \frac{e^4 e_q^2}{4k^4}\left[8(2(p_1k_2)2(p_2k_1)+2(p_2k_2)2(p_1k_1))-8\lambda_1\lambda_2(2(p_1k_2)2(p_2k_1)+2(p_2k_2)2(p_1k_1))+16m_{\tilde{\chi}^0_j}m_{\tilde{\chi}^0_i}(1-\lambda_1\lambda_2)(p_1p_2)\right]$$

In the last expression we denote: $2p_1k_2 = \left(m^2_{\tilde{\chi}^0_j} - u\right)$, $2p_2k_1 = \left(m^2_{\tilde{\chi}^0_i} - u\right)$, $2k_2p_2 = \left(m^2_{\tilde{\chi}^0_j} - t\right)$, $2k_1p_1 = \left(m^2_{\tilde{\chi}^0_i} - t\right)$, $2(p_1p_2) = s$ and at the end we get

$$|M|^2_{pol} = \frac{2e^4 e_q^2}{k^4}\left[\left(m^2_{\tilde{\chi}^0_j} - u\right)\left(m^2_{\tilde{\chi}^0_i} - u\right)+\left(m^2_{\tilde{\chi}^0_j} - t\right)\left(m^2_{\tilde{\chi}^0_i} - t\right)+m_{\tilde{\chi}^0_j}m_{\tilde{\chi}^0_i}s\right]\cdot(1-\lambda_1\lambda_2) \qquad (3)$$

Thus, we obtain following expression for cross section of process collision polarized protons:

$$\left(\frac{d\sigma}{dQ}\right)_{pol} = N_c\frac{\delta_{ij}g^4\lambda_{ij}}{2304\pi^2 s^2}|M|^2_{pol}$$

where

$$\lambda_{ij} = \frac{1}{2}\sqrt{\left(s - m^2_{\tilde{\chi}^0_i} - m^2_{\tilde{\chi}^0_j}\right)^2 - 4m^2_{\tilde{\chi}^0_i}m^2_{\tilde{\chi}^0_j}}$$

$$\sigma_{pol} = \frac{\lambda_{ij}}{1152\pi^2 s^2}|M|^2_{pol}\int_{-\pi}^{\pi}\sin\theta d\theta\int_0^{2\pi}d\varphi = 4\pi\frac{\lambda_{ij}}{1152\pi^2 s^2}|M|^2_{pol}$$

$$\sigma_{pol} = \frac{\lambda_{ij}}{288\pi s^2}|M|^2_{pol} \qquad (4)$$

3. Energy spectrum of born neutralino

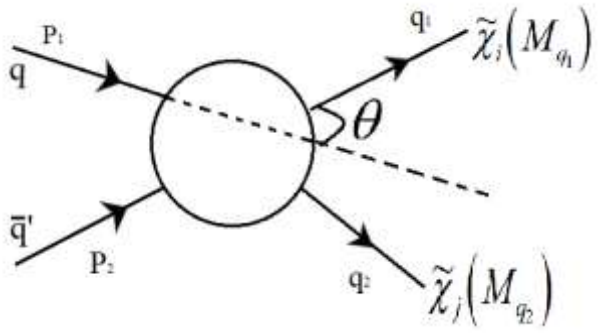

Fig.2 Energetically diagram of born neutralino.

we denote: $c' \equiv \cos\theta = \cos\left(q_1 \wedge p_1\right),\ k \equiv \cos\varphi = \cos\left(p_1 \wedge p_2\right),\ r \equiv \cos\psi = \cos\left(p_2 \wedge q_1\right)$

Use momentum and energy conservation laws:

$$\overrightarrow{p_1} + \overrightarrow{p_2} = \overrightarrow{q_1} + \overrightarrow{q_2} \qquad E_1 + E_2 - E_{q_1} - E_{q_2} = 0$$
$$\overrightarrow{q_2} = \overrightarrow{p_1} + \overrightarrow{p_2} - \overrightarrow{q_1}$$

Thus

$$p_1^0 + p_2^0 - \sqrt{\overrightarrow{q_1^2} + M_{q_1}^2} - \sqrt{\left(\overrightarrow{p_1} + \overrightarrow{p_2} - \overrightarrow{q_1}\right)^2 + M_{q_2}^2} = 0$$

$$E_1 + E_2 - \sqrt{\overrightarrow{q_1^2} + M_{q_1}^2} = \sqrt{\left(\overrightarrow{p_1} + \overrightarrow{p_2} - \overrightarrow{q_1}\right)^2 + M_{q_2}^2}$$

$$\left(E_1 + E_2 - \sqrt{\overrightarrow{q_1^2} + M_{q_1}^2}\right)^2 = \left(\overrightarrow{p_1} + \overrightarrow{p_2} - \overrightarrow{q_1}\right)^2 + M_{q_2}^2$$

$$E_1^2 + E_2^2 + \left(\overrightarrow{q_1^2} + M_{q_1}^2\right) + 2E_1E_2 - 2\left(E_1 + E_2\right)\sqrt{\overrightarrow{q_1^2} + M_{q_1}^2} = \overrightarrow{p_1}^2 + \overrightarrow{p_2}^2 + \overrightarrow{q_1}^2 + 2p_1p_2k - 2p_1q_1c' - 2p_2q_1r + M_{q_2}^2$$

where: $E_1^2 = \overrightarrow{p_1}^2 c^2 + m_1^2 c^4$; $\quad c = 1 \Rightarrow E_1^2 = \overrightarrow{p_1}^2 + m_2^2$, $\quad E_2^2 = \overrightarrow{p_2}^2 c^2 + m_2^2 c^4$;
$c = 1 \Rightarrow E_2^2 = \overrightarrow{p_2}^2 + m_2^2$

aftersimplification we obtain:

$$\left(m_1^2 + m_2^2 + M_{q_1}^2 - M_{q_2}^2\right) + 2\left(E_1E_2 - p_1p_2k\right) + 2\left(p_1c' + p_2r\right)\overrightarrow{q_1} = 2\left(E_1 + E_2\right)\sqrt{\overrightarrow{q_1}^2 + M_{q_1}^2}$$

Squeeze the last equation and we obtain following quadratic equation in $\overrightarrow{q_1}$:

$$4\left(\left(p_1c' + p_2r\right)^2 - \left(E_1 + E_2\right)^2\right)\overrightarrow{q_1}^2 + 4\left(p_1c' + p_2r\right)\left(\left(m_1^2 + m_2^2 + M_{q_1}^2 - M_{q_2}^2\right) + 2\left(E_1E_2 - p_1p_2k\right)\right)\overrightarrow{q_1} + \left(m_1^2 + m_2^2 + M_{q_1}^2 - M_{q_2}^2\right)^2 +$$
$$+ 4\left(E_1E_2 - p_1p_2k\right)^2 + 4\left(m_1^2 + m_2^2 + M_{q_1}^2 - M_{q_2}^2\right)\left(E_1E_2 - p_1p_2k\right) - 4\left(E_1 + E_2\right)^2 M_{q_1}^2 = 0$$

$$a\overrightarrow{q_1}^2 + b\overrightarrow{q_1} + c = 0$$

where

$$a = 4\left(\left(p_1c'+p_2r\right)^2 - \left(E_1+E_2\right)^2\right)$$

$$b = 4\left(p_1c'+p_2r\right)\left(\left(m_1^2+m_2^2+M_{q_1}^2-M_{q_2}^2\right)+2\left(E_1E_2-p_1p_2k\right)\right)$$

$$c = \left(m_1^2+m_2^2+M_{q_1}^2-M_{q_2}^2\right)^2+4\left(E_1E_2-p_1p_2k\right)^2+4\left(m_1^2+m_2^2+M_{q_1}^2-M_{q_2}^2\right)\left(E_1E_2-p_1p_2k\right)-4\left(E_1+E_2\right)^2M_{q_1}^2 =$$

$$= \left(\left(m_1^2+m_2^2+M_{q_1}^2-M_{q_2}^2\right)+2\left(E_1E_2-p_1p_2k\right)\right)^2-4\left(E_1+E_2\right)^2M_{q_1}^2$$

The discriminante of equation is

$$D = 16c'^2\left(2E_1E_2+m_1^2+m_2^2+M_{q_1}^2-M_{q_2}^2\right)^2p_1^2-16\left(-4\left(E_1E_2\right)^2M_{q_1}^2+2\left(E_1E_2\right)^2+\left(m_1^2+m_2^2+M_{q_1}^2-M_{q_2}^2\right)^2\right)x$$

$$x\left(\left(E_1+E_2\right)^2+c'p_1\right)$$

We will look for solutions in which the discriminate is greater from zero and the roots are non-negative

4. Results and Discussion

Cross section of collision (expressions (2) and (4)) unpolarized and polarized protons has been evaluated. Data for calculation was been take from [19,20].

In the fig.3 the dependence of cross section of proton-proton collision on its energy has been presented. As see cross section of process is increased with increasing of energy of protons. Increasing of cross section with increasing energy of colliding protons can be explained as: at high speeds (energy) of protons probability of collision is increased. As see difference between cross sections unpolarized and polarized cases is increased at high energies. Cross section of collision weakly depends on the change in mass of neutralino. However, there is a slight difference for different neutralino at √s=10Tev.

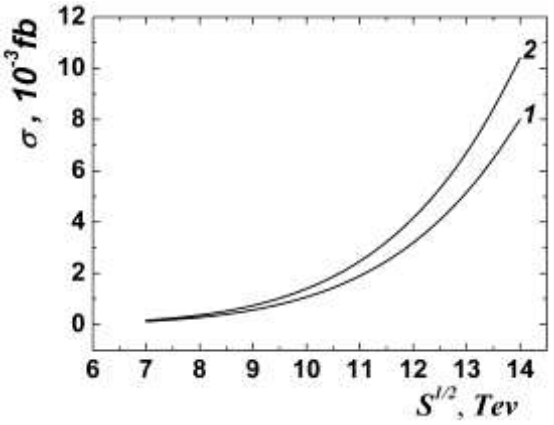

Figure 3. The dependence of cross section of collision unpolarized (1) and polarized protons (2) on its energy.

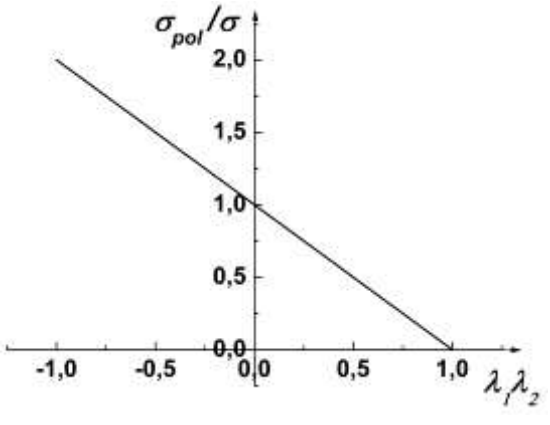

Figure 4. The dependence relationship between effective sections of collision polarized and unpolarized protons on $\lambda_1\lambda_2$.

In the fig.4 is presented thedependence relationship between effective sections of collision polarized and unpolarized protons on $\lambda_1\lambda_2$. As can be seen from the graph at $\lambda_1\lambda_2 = 1$ we get $\sigma_{pol}/\sigma = 0$. However, this does not mean that the total effective section of the proton-proton collision is zero. The present work we considered the formation neutralino by *v* photon (s - channel). In addition to this process of neutralino can birth by means of Z^0 and *W* bosons, the effective cross-section of these processes is different from zero.

The value of q_1 does not depend on the cosine of the scattering angle- θ and it is constant. The dependence of q_1 on the energy of colliding protons is presented in figure 5. The energy value corresponding to the maximum value of q_1 can simply be mathematically determined from the conditions $E_1 + E_2 = const_1$ and $E_1E_2 = const_2$. Consequently it is equal approximately to $E_1 = const_1 /2$.

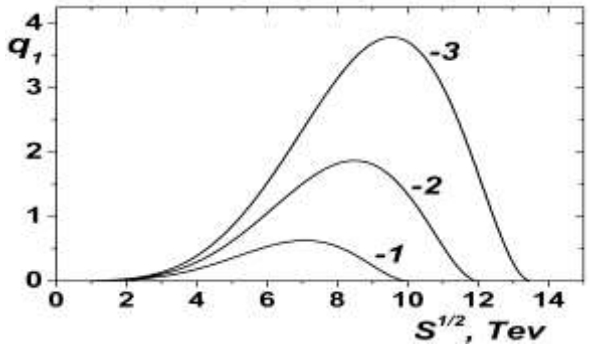

Figure 5. The dependence energy spectrum of q_1 at differentenergycollision of protons: $E_1 < E_2 < E_3$

Expressions (1) and (3) differ by a factor $(1-\lambda_1\lambda_2)$. As see polarization of protons influenced to cross section of collision. Depending on the values of $\lambda_1$and λ_2, the values of the effective cross section change. The value of the effective cross section not only depends on the polarization degree of individual beams, but also on the mutual polarization of the colliding proton beams.

As known, thedegree of polarization is determinedbytheexpression: $\lambda = \frac{|n\uparrow - n\downarrow|}{n\uparrow + n\downarrow}$. The spins of the colliding protons can have the following directions along the axis of theircollision: a)$p_1\uparrow$ $p_2\uparrow$, b) $p_1\uparrow$ $p_2\downarrow$, c) $p_1\downarrow$ $p_2\downarrow$ d) $p_1\downarrow$ $p_2\uparrow$.

The direction of the spin affects the effective cross section for proton collisions. Therefore, the effective cross section can increase and decrease depending on the mutual direction of the colliding protons.

Indeed, in the absence of polarization of one or both beams of colliding protons $\lambda_1\lambda_2=0$ expression (3) coincides with (1). $\lambda_1\lambda_2=0$ may be in these cases: a) $\lambda_1=0$, $\lambda_2=0$ or b) $\lambda_1=0$, $\lambda_2\neq0$ or $\lambda_1\neq0$, $\lambda_2=0$).

In addition, for the same value of $\lambda_1\lambda_2$ for different values of the products λ_1 and λ_2, the effective cross section for the collision of polarized protons is the same. The physical meaning of this is obvious. Consider the simple case when the first proton beam has a degree of polarization $\lambda_1$and the second beam has λ_2. If the degree of polarization of the beams is naturally changed, the value of the effective cross section will not change. Consider when the product $\lambda_1\lambda_2$ is equal to some number, for example, $\lambda_1\lambda_2 = 0.12$. These values can be obtained in 2 cases: a)$\lambda_1 = 0.3$, $\lambda_2 = 0.4$, and b) $\lambda_1 = 0.2$, $\lambda_2 = 0.6$. In the other case, for $\lambda_1\lambda_2 = 0.18$, a) $\lambda_1 = 0.2$, $\lambda_2 = 0.9$, and b) $\lambda_1 = 0.3$, $\lambda_2 = 0.6$ can be. The physical meaning of this is unclear and requires further explanation.

We suggested that the rest of the contribution could be made by gluons, whose angular moment was neglected in early calculations. In order to measure it, it was necessary to set an experiment in which the properties of "nuclear glue" would play a decisive role.

The QCD effects in the associated production of $\chi^{\pm}\chi^0$ in the MSSM within the mSUGRA scenario at both the Tevatron and the LHC, including the NLO SUSY QCD corrections and the NLL threshold resummation effects are considered in [15]. Comparing our results with [15] showed that they are agree.

All calculations were carried out with the help a package of the Mathematica-10 program, program calculation of cross section, solution of equation were written in FORTRAN algorithmic language, and figures are constructed by means of the Origin 9.5 software package.

5. Conclusions

1. The value of q_1 does not depend on the cosine of the scattering angle θ. Neutralino born have a spherically symmetric distribution.
2. The energy spectrum of the born neutralino is Gaussian like. The maximum of the energy spectrum corresponds to the value $E_1 = SQ/2$
3. The effective cross section of the process with the formation of various neutralinos, despite their different masses, does not differ. Therefore, experiments to study the effective cross section with the formation of neutralinos will not make it possible to distinguish between different neutralinos. This requires additional experiments.
4. The effective collision cross section with polarized protons is different than unpolarized protons.

References

[1] https://nplus1.ru/news/2016/02/18/gluons-protons-angular-moment.
[2] http://www.dslib.net/atom-jadro/issledovanie-spektra-jeffektivnyh-mass-dvuh-protonov-iz-reakcii-p-np-p.html.
[3] The ALIICE Collaboration K_0s K_0s correlations in pp collisions at √s = 7 TeV, 2012. arXiv: hep-ex/1206.2056v1.
[4] The ALIICE Collaboration Production of pions, kaons and protons in pp collisions at √s = 900 GeV, 2012. arXiv:hep-ph/0610012.
[5] Anferov V.A., Blinov B.B., KantsyrevD.Yu., Krisch A.D., Sivers D.W., Arbor Ann., Chu M., Schwandt P., von Przewosk B., Grishin N. 2000. Spin flipping a stored polarized proton beam with an rf dipole, Physical Review, special topics - Accelerators and beams, 3: 041001.
[6] Haber H.E., Kane G.L. 1985. The search for supersymmetry probing physics beyond the standard model. Physics Reports, Review Section of Physics Letters, 117 (2): 75-263. https://doi.org/10.1016/0370-1573(85)90051-1.
[7] Debovea J., Fuksb Bn., Klasena M. 2008. Gaugino-pair production in polarized and unpolarized hadron collisions. arXiv: hep-ph/0804.0423v2.
[8] Ahmadov A.I., Demirci M. 2013. Single neutralino production at the LHC. ArXiv: hep-ph/ 1307.3777v1.
[9] Demirci M., Ahmadov A.I. 2014. Search for neutralino pair production at the CERN LHC. Physical Review. (D 89): 075015.
[10] The ATLAS Experiment at the CERN Large Hadron Collider 2008. ATLAS Collaboration, JINST, 3: S08003.
[11] ATLAS Collaboration, 2013. Report No. ATLAS-CONF-2013-047.
[12] CMS Collaboration, 2013. Report No. CMS-PAS-SUS-13-012.
[13] De Roeck A., Gehrmann T. 1997. Physics with Polarized Protons at HERA, Introduction to the Proceedings of the Workshop on Physics with Polarized Protons at HERA", DESY.
[14] Baer H., Mustafayev A., Summi H., Tata X. 2007. Mixed higgsino dark matter from a large SU(2) gaugino mass. Journal High Energy Physics, 1-42.
[15] Li C.S., Li Sh., Yang L.L. 2008. Thershold Resummatic effects in the associate production of chargino and neutralino at the Hadron Colliaders. arXiv: hep-ph/0707.3962v4.
[16] Bper W., Ehrer R., Kazakov D.I. 2014. Redictions of SUSU masses in the Minimnal Supersymmetric Grand Unified Theory. IEKP-AK / 94-05, HEP_PH- 9405342.
[17] Fuks B., Klasen M., Lamprea D.R., Rothering M. 2016. Precision predictions for direct gaugino and slepton production at the LHC. Nuclear and Particle Physics Proceedings, 273–275.
[18] Okun L.B. 1990. Leptoni I kvarki, M.Nauka, Moscow, 346p.
[19] http://nuclphys.sinp.msu.ru/introduction/particltab.htm.
[20] http://pdg.lbl.gov.

Araştırma Makalesi / Research Article

Bitlis'te Yetişen Bazı Tıbbi ve Aromatik Bitkilerin Radyo İzotop Aktivite Konsantrasyonları

Sultan ŞAHİN BAL[1*], Fikriye GÖNÜLTAŞ[1], Önder KILIÇ[1], Murat KURŞAT[2], Ayşegül DEMİR YETİŞ[3]

[1]Bitlis Eren Üniversitesi, Fizik Bölümü, Bitlis
[2]Bitlis Eren Üniversitesi, Biyoloji Bölümü, Bitlis
[1]Bitlis Eren Üniversitesi, Çevre Mühendisliği Bölümü, Bitlis
(ORCID: 0000-0001-7896-0771) (ORCID:0000-0002-8514-7399) (ORCID:0000-00018948-3413)
(ORCID:0000-0002-0861-4213) (ORCID:0000-0003-4745-2445)

Öz
Bu çalışmada, Bitlis'te yetişen bazı bitkilerde doğal olarak bulunan radyo izotop konsantrasyon seviyeleri belirlendi. Numuneler, NaI(Tl) gama ışını spektrometresi kullanılarak analiz edildi. Bu bitkilerde, ^{226}Ra radyo izotop aktivite konsantrasyon seviyelerinin 12,45 ± 2,53 Bq/kg ile 92,08 ± 5,34 Bq/kg arasında, ^{232}Th radyo izotop konsantrasyon seviyelerinin 23,10 ± 4,42 Bq/kg ile 88,00 ± 6,68 Bq/kg arasında, ^{40}K radyo izotop konsantrasyon seviyelerinin 42,57 ± 5,15 Bq/kg ile 533 ± 7,78 Bq/kg arasında değiştiği görülmüştür.

Anahtar kelimeler: Tıbbi ve Aromatik Bitkiler, Radyo Çekirdek, Bitlis.

The Radioisotope Activity Concentrations of Some Medical and Aromatic Plants Growing in Bitlis

Abstract
In this study, the levels of radioisotope activity concentration naturally found in some plants growing in Bitlis were determined. The samples are analyzed using NaI(Tl) gamma ray spectrometry. In these plants, it is seen that the levels of ^{226}Ra radioisotope activity concentration between 12.45 ± 2.53 Bq/kg and 92.08 ± 5.34 Bq/kg, the levels of ^{232}Th activity concentration between 23.10 ± 4.42 Bq/kg and 88.00 ± 6.68 Bq/kg, the levels of ^{40}K radioisotope activity concentration between 42.57 ± 5.15 Bq/kg and 533.48±7.78 Bq/kg are changed.

Keywords: Medicinal and Aromatic Plants, Radioisotope, Bitlis.

1. Giriş

Doğal radyo-çekirdekler, dünyanın oluşumundan bu yana; dünyanın bileşenleri olmuştur ve dünya ortamında doğal olarak yayılmıştır. Doğal ortamda, uranyum ve toryum serisine ait radyoizotoplar ve ^{40}K içeren birçok doğal olarak oluşan radyo-çekirdek vardır. Bu doğal radyo-çekirdekler toprakta, tortuda, suda, bitkilerde ve havada bulunur. Çevresel radyoaktivite ve gama radyasyonu nedeniyle; dış kaynaklı radyasyona maruz kalma, temel olarak dünyadaki her bir bölgenin jeolojik koşullarına, toprak ve sediment oluşumlarına bağlıdır [1, 2].

Herhangi bir bölgenin jeolojik ve coğrafi koşulları; radyo-çekirdek konsantrasyonunun seviyesini etkileyerek, farklı kısa ve uzun ömürlü radyo-çekirdeklerin dünyanın biyo-matrislerini kirletmesine neden olur [3, 4].

Canlı organizmalar genellikle doğal veya insan yapımı kaynaklardan yayılan arka plan (background) radyasyona sürekli olarak maruz kalırlar. Radyasyonun etki türleri deterministik ve

*Sorumlu yazar: sahin.sultan@gmail.com
Geliş Tarihi: 28.10.2019, Kabul Tarihi: 19.12.2019

stokastik etkilerdir. Canlı organizmalara radyasyondan gelen etkiler; genellikle stokastik etki kategorisine girer [5].

Geleneksel olarak genellikle şifa bulmak ya da tatlandırmak amacıyla kullanılan şifalı bitkiler; radyoaktif içerikleri açısından incelenen yenilebilir bitkiler grubuna dahil edilmez, çünkü tüketimlerinden dolayı doğrudan radyoaktif madde alımı önemsiz kabul edilmiştir. Yüksek konsantrasyonlarda doğal radyo-çekirdek içeren bir şifalı bitki, uzun süre boyunca yaygın olarak kullanıldığında sağlık sorunlarına neden olabilir [6].

Bu çalışmada, Bitlis bölgesinde yetişen, genellikle tatlandırıcı ve şifa bulmak amacıyla sıkça tüketilen bazı bitki örneklerinin radyoaktivite konsantrasyon seviyeleri tespit edilmiştir.

2. Materyal ve Metot

2.1. Bitlis'in Genel Jeolojisi

Bitlis Metamorfik kuşağı boyunca çeşitli stratigrafik kesitler mevcuttur. Asidik karakterli magma çıkışları, granit, granitik gnayslar, andezitler, dasitler ile bazik karakterli bazaldik lavlar bulunmaktadır (Şekil 1) [7].

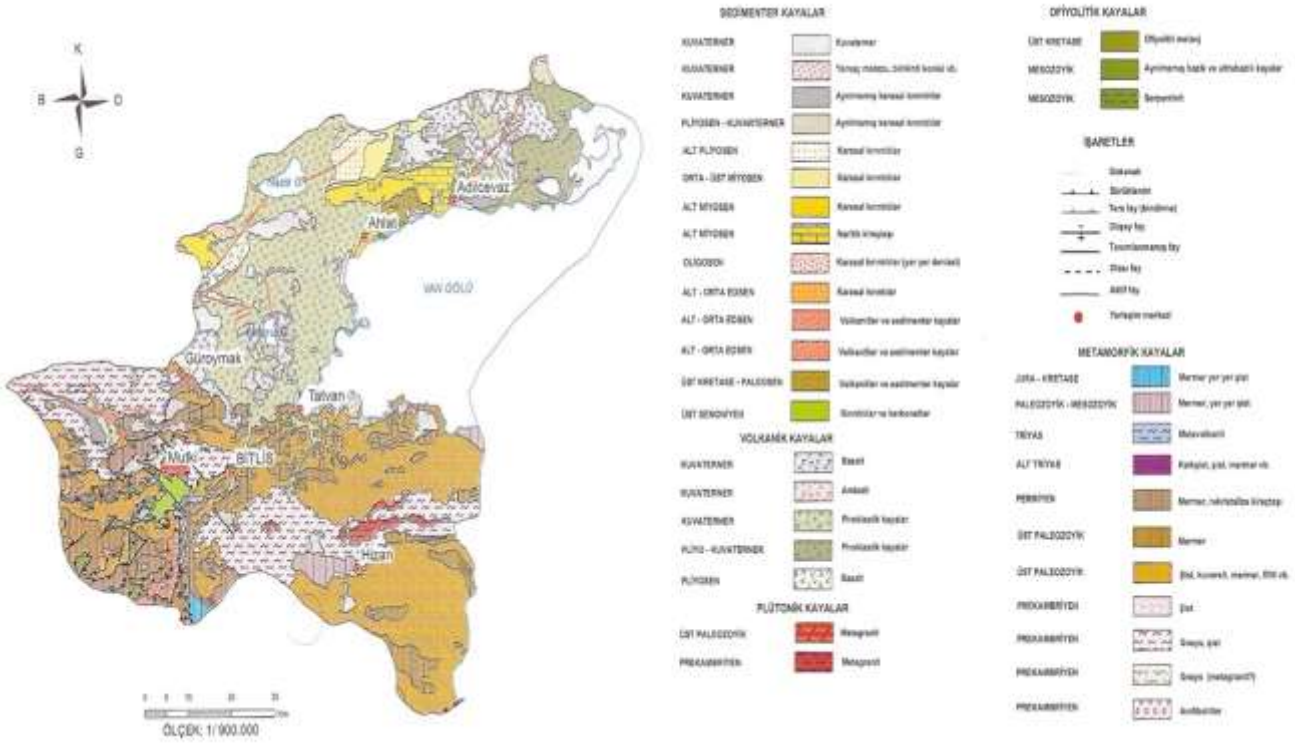

Şekil 1. Bitlis'in jeolojik haritası

2.2. Aktivite Ölçümleri

Tamamen nemden arındırmak amacıyla, bitki örnekleri alüminyum folyalara sarıldı ve 80 ^{0}C'de etüv içerisinde yaklaşık 24 saat bekletildi. Örnek kapları içine konulan bitki örnekleri, yaklaşık 30 gün boyunca radyoaktif dengenin sağlanması için bekletildi.

Örnekler, ORTEC marka 3x3-inç boyutunda kristal Talyum (TI) katkılı NaI sintilatörlü, 0,5 MeV de % 2 ve 2 MeV de % 1,3 verime sahip gama detektöründe 86400 s sayıldı. Bitki örneklerinin analizinde ^{226}Ra aktivitesi için; ^{214}Bi'nin 609,312 keV'lik fotopiki kullanılmıştır. ^{232}Th aktivitesi için; ^{228}Ac'nin 911,205 keV'lik fotopiki kullanılmıştır.^{40}K aktivitesi için ise 1461,83 keV'lik fotopik kullanılmıştır. Aşağıdaki denklem kullanılarak aktivite hesabı yapılmıştır [8, 9].

$$A = \frac{C}{\varepsilon \times t \times M} \quad (1)$$

Yukarıdaki denklemde; A, radyoizotop konsantrasyonu (Bq/kg), C, net pik alanı (sayım), ε, verim, t, sayım süresi (86400 s), M, numune kütlesidir (kg).

3. Bulgular ve Tartışma

Şifalı bitki örneklerinin ^{226}Ra, ^{232}Th ve ^{40}K radyo-çekirdek aktivite konsantrasyonları Tablo 1'de verilmiştir. Şifalı bitki örneklerinin, ^{226}Ra radyo-çekirdek aktivite konsantrasyonun; 12,45 ± 2,53 Bq/kg (B01) ile 92,08 ± 5,34 Bq/kg (B03) arasında, ^{232}Th radyo-çekirdek aktivite konsantrasyonun 23,10 ± 4,42 Bq/kg (B11) ile 88,00 ± 6,68 Bq/kg (B04) arasında, ^{40}K'ın ise radyo-çekirdek aktivite konsantrasyonun; 42,57 ± 5,15 Bq/kg (B07) ile 533,48 ± 7,78 Bq/kg (B12) değerleri arasında değiştiği görülür.

Tablo 1. Bazı tıbbi ve aromatik bitki örneklerinin ^{226}Ra, ^{232}Th ve ^{40}K radyo-çekirdek aktivite konsantrasyonları

Numune	Numune Adı	Lokasyon	^{226}Ra (Bq/kg)	^{232}Th (Bq/kg)	^{40}K (Bq/kg)
B01	Sarı civanperçemi	Tatvan	12,45±2,53	48,57±6,76	252,26±5,19
B02	Boz otu	Tatvan	41,06±1,81	66,17±3,65	413,00±6,39
B03	Isırgan otu	Tatvan	92,08±5,34	63,21±2,81	469,84±7,59
B04	Deve dikeni	Tatvan	74,74±3,87	88,00±6,68	451,07±6,40
B05	Şirker	Tatvan	38,99±2,22	74,40±6,89	147,18±4,13
B06	Kekik	Tatvan	35,44±1,74	59,77±3,72	308,82±5,85
B07	Boz otu	Tatvan	42,71±2,05	46,95±3,39	42,57±5,15
B08	Yabani tere	Tatvan	32,34±4,36	41,10±1,91	323,63±5,52
B09	Gelincik	Ahlat	51,54±2,25	75,11±3,99	398,34±5,97
B10	Sarı civanperçemi	Adilcevaz	34,09±1,44	66,74±4,75	432,75±6,63
B11	Pıtrak	Güroymak	59,93±3,01	23,10±4,42	439,75±6,59
B12	Taş turşusu	Güroymak	23,26±5,37	65,87±3,05	533,48±7,78
B13	Sarı civanperçemi	Ahlat	18,88±1,08	36,81±4,70	253,72±4,65

Şekil 2 incelendiğinde; ^{40}K radyo-çekirdek aktivite konsantrasyonlarının, ^{226}Ra ve ^{232}Th radyo-çekirdek aktivite konsantrasyonlarından fazla olduğu görülmektedir. B07 numaralı bitki örneğinde, her üç radyo-çekirdek aktivite konsantrasyonunun hemen hemen aynı değere sahip olduğu görülmektedir. B03 ve B11 numaralı bitki örneklerinde, ^{226}Ra radyo-çekirdeği aktivite konsantrasyonunun ^{232}Th radyo-çekirdek aktivite konsantrasyonundan fazla olduğu görülmektedir. Diğer bitki örneklerinde, ^{232}Th radyo-çekirdek aktivite konsantrasyonları ^{226}Ra radyo-çekirdek aktivite konsantrasyonlarından daha fazladır.

Bu çalışmada tespit edilen radyo-çekirdek aktivite konsantrasyonları, literatürde yapılan benzer çalışmalar (Tablo 2) ile karşılaştırıldığında; Radyum ve Toryum radyoaktivite konsantrasyon değerlerinin diğer çalışmalarda tespit edilen değerlerin çok üstünde olduğu görülmektedir. Potasyum radyoaktivite konsantrasyon değerlerinin ise, diğer çalışmalarla hemen hemen aynı değer aralıklarında olduğu görülmektedir. Bitkilerdeki radyoaktivite konsantrasyon değerleri; doğrudan toprak ve sudaki radyoaktivite konsantrasyon seviyelerine bağlıdır. Bununla beraber; bölgenin jeolojik oluşumuna, bitkinin yetiştiği ortamın atmosferik faktörlerine, bitkinin biyolojik ve kimyasal özelliklerine ve daha birçok dış etkene de bağlıdır.

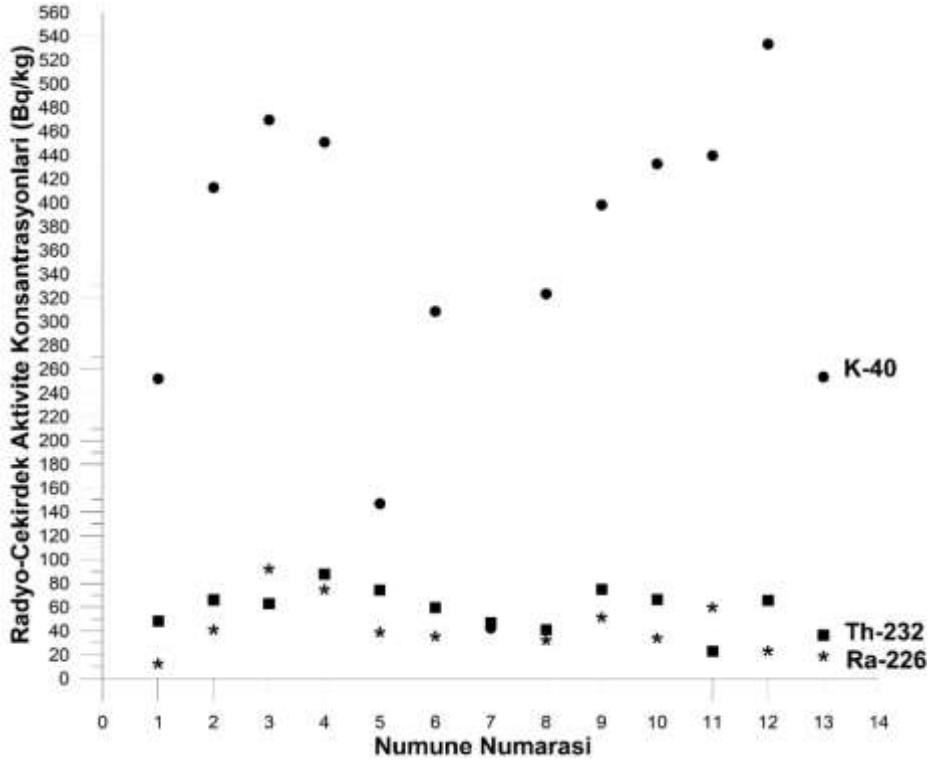

Şekil 2. Bazı tıbbi ve aromatik bitki örneklerinin ^{226}Ra (∗), ^{232}Th (■) ve ^{40}K (•) radyo-çekirdeklerinin aktivite konsantrasyonları

Tablo 2. Literatürdeki bazı çalışma örnekleri [6, 10-13]

Lokasyon	Bitki Türü	^{226}Ra (Bq/kg)	^{232}Th (Bq/kg)	^{40}K (Bq/kg)
Nijerya	Tıbbi	25,02	35,09	171,72
Güney Hindistan	Tıbbi	6,34	5,05	1895,25
Brezilya	Tıbbi	15,85	4,35	-
Nijerya	Sebze	8,75	20,13	263,88
Malezya	Pirinç	4,15	3,04	272,23
Bitlis (Bu çalışma)	Tıbbi	42,89	58,14	343,57

4. Sonuç ve Öneriler

Bu çalışmada, Bitlis'te yetişen 13 tıbbi ve aromatik bitki örneklerinin ^{226}Ra, ^{232}Th ve ^{40}K radyo-çekirdek aktivite konsantrasyonları belirlenmiştir.

(i) B01 (Tatvan), B10 (Adilcevaz) ve B13 (Ahlat) bitki örnekleri aynı tür (Achillea Biebersteinii Afan-Sarı civan perçemi) bitkilerdir. Bununla birlikte; B02 (Tatvan-Küçüksu Köyü) ve B07 (Tatvan-Han Elmalı Köyü) bitki örnekleri de kendi aralarında aynı tür (Marrubium Parviflorum-Boz otu) bitkilerdir. Fakat, her iki bitki türü örnekleri; farklı radyo-çekirdek aktivite konsantrasyon değerlerine sahiptir.

(ii) Bitki örneklerinin radyoaktivite konsantrasyon değerleri; lokasyona, jeolojik yapıya, bitki türüne, bitkinin kimyasal özelliklerine, bitkinin beslendiği suya vb. faktörlere göre değişmektedir.

(iii) ^{226}Ra ve ^{232}Th radyo-çekirdek aktivite konsantrasyon değerleri literatürdeki benzer çalışmalarda tespit edilen değerlerden daha yüksektir.

(iv) ^{40}K radyo-çekirdek aktivite konsantrasyon değerleri, literatürdeki benzer çalışmalarda tespit edilen değerler arasındadır.

Kaynaklar

[1] Aközcan S. 2012. Distribution of Natural Radionuclide Concentrations in Sediment Samples in Didim and Izmir Bay (Aegean Sea-Turkey). Journal of Environmental Radioactivity, 112: 60-63.

[2] Issa S.A.M., Uosif M.A.M., Tammam M., Elsaman R. 2014. A Comparative Study of the Radiological Hazard in Sediments Samples from Drinking Water Purification Plants Supplied from Different Sources. Journal of Radiation Research and Applied Sciences, 7: 80-94.
[3] UNSCEAR. 2000. Sources and effects of ionising radiation. United Nations Scientific Committee on the Effects of Atomic Radiation., United Nations, New York.
[4] Chandrashekara K., Radhakrishna A.P., Somashekarappa H.M. 2015. Concentration of Natural and Artificial Radionuclides in *Mesua Ferea* Auct Linn - A Medicinal Plant. Life Sciences International Research Journal, 2 (2): 219-223.
[5] Boumala D., Belafrites A., Tedjani A., Mavon C., Groetz J.E. 2019. Annual Effective Dose and Excess Life Timecancer Risk Assessment from Tobacco plants. Perspectives in Science, 12 (100394): 1-4.
[6] Sussa F.V., Damatto S.R., Alencar M.M., Mazzilli B.P., Silva P.S.C. 2013. Natural Radioactivity Determination in Samples of Peperomia Pellucida Commonly Used as a Medicinal Herb. Journal of Environmental Radioactivity, 116: 148-151.
[7] Işık E. 2010. Bitlis Şehrinin Sismik Performans Analizi. Sakarya Üniversitesi, Fen ve Teknoloji Enstitüsü, Doktora Tezi Sakarya.
[8] Ortec. 2010. Katı-Hal Dedektörü Kullanma Kılavuzu, USA.
[9] Gönültaş F. 2016. Bitlis'te Yetişen Bazı Tıbbi ve Aromatik Bitkilerde Radyoizotop Aktivite Konsantrasyonlarının Belirlenmesi. Bitlis Eren Üniversitesi, Fen Bilimleri Enstitüsü, Yüksek Lisans Tezi, 52s, Bitlis.
[10] Njinga R.L., Jonah S.A., Gomina M. 2015. Preliminary Investigation of Naturally Occurring Radionuclides in Some Traditional Medicinal Plants Used in Nigeria. Journalof Radiation Research and Applied Sciences, 8: 208-215.
[11] Chandrashekara K., Somashekarappa H.M. 2016. Estimation of Radionuclides Concentration and Average Annual Committed Effective Dose Due to Ingestion for Some Selected Medicinal Plants of South India. Journal of Radiation Research and Applied Sciences, 9: 68-77.
[12] Okeji M.C., Kenneth K.A., Felicitas U.I. 2012. Natural Radioactivity in Cultivated Land in the Vicinity of a Phosphate Fertilizer Plant in Nigeria. Radiation Physics and Chemistry, 81: 1823–1826.
[13] Alsaffar M. S., Jaafar M. S., Kabir N. A., Ahmad N. 2015. Distribution of ^{226}Ra, ^{232}Th and ^{40}K in Rice Plant Components and Physico-Chemical Effects of Soil on Their Transportation to Grains. Journal of Radiation Research and Applied Sciences, 8: 300-310.

Araştırma Makalesi / Research Article

Investigation of the Collimator Effect on the 3″x3″ NaI(Tl) Detector System by the FLUKA code

Zehra Nur KULUÖZTÜRK[1*], Nilgün DEMİR[2]

[1]*Bitlis Eren University, Vocational School of Health Services, Bitlis, Turkey*
[2]*Bursa Uludağ University, Physics Department, Bursa, Turkey*
(ORCID:0000-0003-0929-5987)(ORCID:0000-0003-2245-8461)

Abstract
The efficiency of the 3″x3″ NaI(Tl) detector and gamma attenuation calculations were investigated under the different collimation parameters. In this purpose, photon beams with 511 and 1332 keV energy were collimated by using Pb collimator with different diameters. This system was defined by the FLUKA Monte Carlo code; the detector efficiency and gamma attenuation coefficients were simulated.

Keywords: 3″x3″ NaI(Tl) Detector, Collimator simulations, FLUKA.

FLUKA kodu ile 3″x3″ NaI(Tl) Detektör Sistemine Kolimatör Etkisinin İncelenmesi

Öz
3″x3″ NaI(Tl) detektörünün verimliliği ve gama zayıflatma hesaplamaları farklı kolimasyon parametreleri altında incelenmiştir. Bu amaçla, 511 ve 1332 keV enerjili foton demetleri, farklı çaplarda Pb kolimatörü kullanılarak kolime edildi. Bu sistem FLUKA Monte Carlo kodu ile tanımlandı; detektör verimliliği ve gama zayıflama katsayıları simüle edildi.

Anahtar kelimeler: 3″x3″ NaI(Tl) detektörü, Kolimatör simülasyonları, FLUKA.

1. Introduction

Investigation of the absorption of gamma rays on material, that is to know the gamma absorption coefficient of the material, is essential not only for radiation physics studies but also for studies in medicine, industry, and biology. Gamma attenuation coefficient calculations have been reported in numerous studies using experimental and theoretical methods [1-7]. The gamma attenuation coefficient depends on the characteristics of the absorber and the energy of the gamma source. In order to avoid significant differences between the gamma attenuation coefficients obtained from different methods, the most appropriate parameters should be determined when making measurements and calculations. One of the most critical parameters taken into consideration for this is the suitable collimation and transport of the beam. Since the gamma sources used in the gamma attenuation coefficient measurements have an isotropic distribution, the beam must be collected correctly and reached to the absorbent material and the detector. When the transmitted beam is collected correctly, and a narrow beam is obtained, a large number of scattered photons are prevented from reaching the detector. The studies related to beam collimation have been presented using various absorber materials and detector systems at different energies [8-11].

The scintillation detectors, which are based on the principle that the gamma rays entering the detector are transformed into visible light photons by the so-called scintillator crystal, are often preferred in radiation investigations because of their high efficiency of measurement and ability to operate at room

*Sorumlu yazar: znkuluozturk@beu.edu.tr
Geliş Tarihi: 07.11.2019, Kabul Tarihi: 20.12

temperature. For this purpose, 3″x3″ NaI(Tl) detector was modeled to investigate the effect of beam collimation in this study. The effect of photon beam collimation on the gamma attenuation coefficient and the full energy peak efficiency of the 3″x3″ NaI(Tl) detector system was theoretically calculated depending on the collimator diameter and the energy of the photon beam. The beam properties, geometry system, physical quantities, formulations, and approaches required for calculations were modeled using FLUKA code.

2. Material and Method

2.1. Theory

In this section, some theoretical formulations are described for the efficiency of the 3″x3″ NaI(Tl) detector and the mass attenuation coefficients determined using this detector. For the quantitative evaluation of the simulation model, the full energy peak efficiency was calculated by the following equation [12];

$$E_{\text{full-energy peak}} = \frac{N_{FEP}}{N} \tag{1}$$

where N_{FEP} and N represent the net count in the full-energy peak corresponding to energy and the number of photons emitted by the source of energy, respectively.

The mass attenuation coefficient which determines the probability of interaction of the photon with the material have been calculated for investigated samples by the following equation based on the Beer-Lambert law;

$$I = I_0 e^{-\mu x} \tag{2}$$

I_0, I and x are the attenuated photon intensity, incident photon intensity and the thickness of the material (cm), respectively.

2.2. Simulation details

The FLUKA code, written in the Fortran programming language and used in the Linux operating system, was developed to calculate particle transport and the interaction of particles with matter [13]. The FLUKA code can simulate electromagnetic and hadronic interactions and particle transport in any target material for 60 different particles. The code is often used in current studies of nuclear physics such as detector design, target design, dose, and shielding calculations.

The details of the 3″x3″ NaI(Tl) detector that modeled by FLUKA code are given in Figure 1. The geometry was modeled with a cylindrical scintillation crystal of 7.62 cm x 7.62 cm with a case of 0.5 mm of aluminum. The space between the case and the crystal was filled with MgO of 0.185 cm thickness. The SiO_2 layer after the crystal is 0.3 cm thick. The detector geometry has been taken from previously reported detector efficiency study [14].

In the simulation, monoenergetic point sources with 511 keV and 1332 keV energy were placed 8 cm away from the detector using BEAM and BEAMPOS cards. The collimator is designed as a lead metal with a cylindrical geometry of 4 cm thickness. The detector layers and their contents are defined in the input file by using MATERIAL, COMPOUND, and ASSIGNMA commands, respectively.

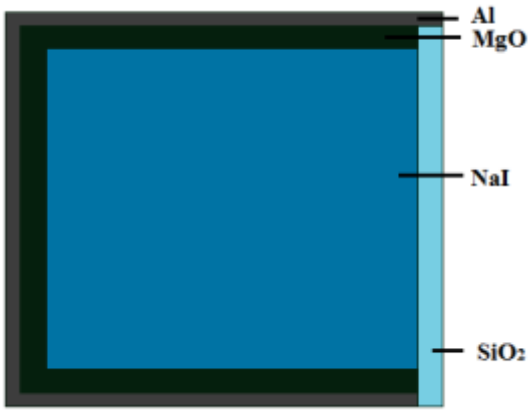

Figure 1. Geometry of 3″x3″ NaI(Tl) detector

The geometry in Figure 2 was modeled and displayed from the geometry editor in the FLAIR interface to calculate the detector efficiency [15]. Figure 2 (a) and Figure 2 (b) show the geometries of the largest (10 mm) and smallest (3 mm) diameter collimators used for this study, respectively. Figure 3 is setup for simulation of the gamma absorption coefficient consisting of an isotropic point source, Pb collimator, absorber material and NaI(Tl) detector. In this study, Aluminum (Al) metal has been chosen as the absorber material. DETECT scoring card was used to investigate the effect of beam collimation. In the FLUKA code, the DETECT card calculates the amount of deposited energy in the detection bin. In addition, the USRBIN card was used for photon fluence calculations in the simulation environment and in the NaI(Tl) detector. All simulation results were obtained by running 10 cycles of 10^5 particles.

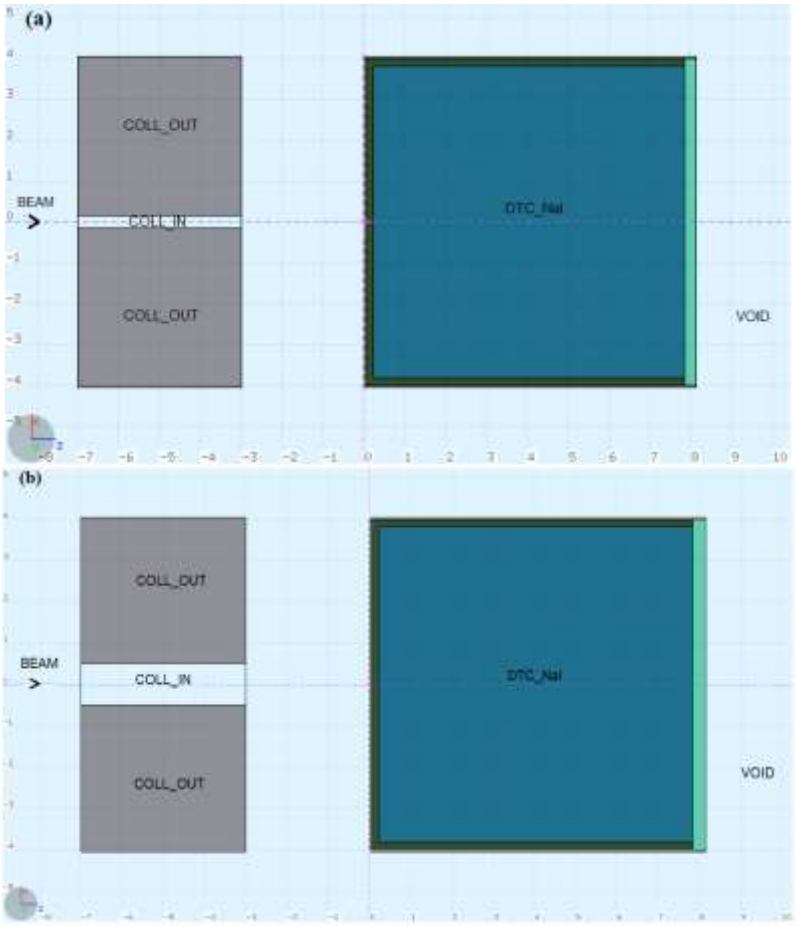

Figure 2. FLUKA geometry with (a) 3 mm and (b) 10 mm diameter collimator for efficiency calculation

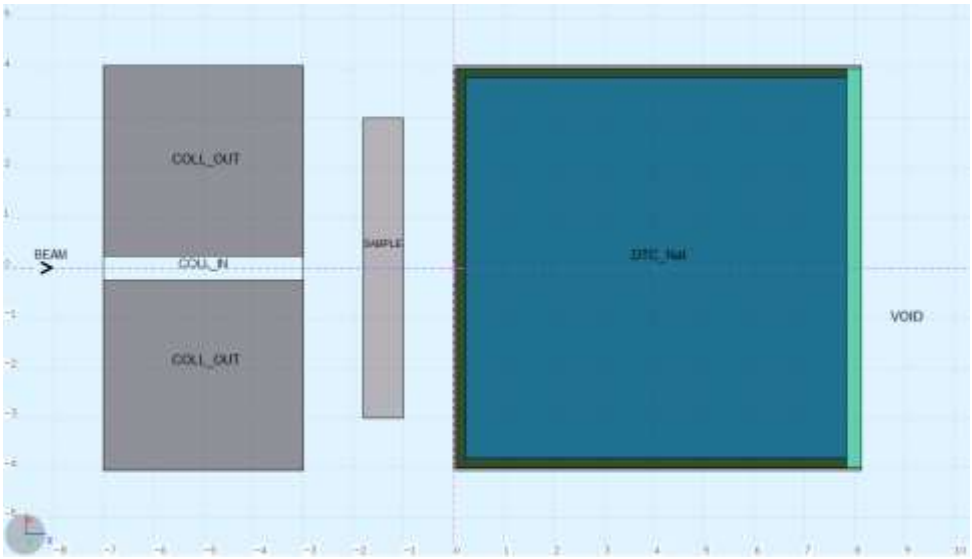

Figure 3. FLUKA geometry with 5 mm diameter collimator for gamma attenuation coefficient calculation

3. Results and Discussion

3.1. Investigation of collimator effect on detector efficiency

In order to investigate the effect of collimator on efficiency in NaI(Tl) detector system, 511 keV and 1332 keV gamma energies and collimators of 3 mm, 5 mm, 7 mm, and 10 mm diameter were used. The variation of the full energy peak efficiency of the detector as a function of the collimator diameter is shown in figure 4 for 511 keV and 1332 keV gamma energy. As the diameter of the collimator increases, the number of photons entering the collimator increases. Therefore, full energy peak efficiency increased due to equation 1. Detector efficiency decreases when the energy increases in the efficiency curve of the NaI(Tl) detector [16]. However, when the beam collimation is performed, as shown in Figure 4, the number under the full energy peak at 1332 keV is higher than 511 keV. Only the highest diameter 10 mm diameter collimator yields almost the same efficiency values in two energies.

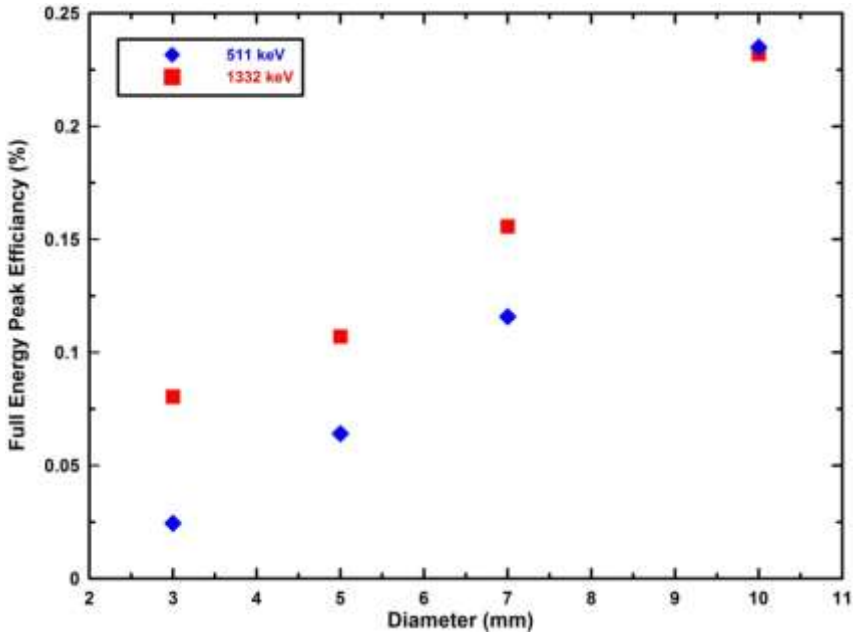

Figure 4. Full energy peak efficiencies calculated by FLUKA code as a function of collimator diameter for 511 keV and 1332 keV gamma energies

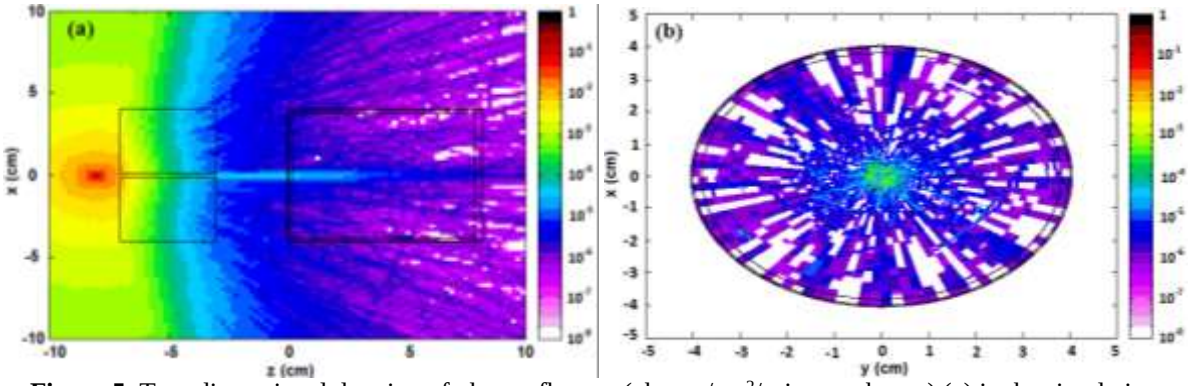

Figure 5. Two-dimensional drawing of photon fluence (photon/cm^2/primary photon) (a) in the simulation volume and (b) in the NaI(Tl) detector for 511 keV photon beam and the collimator with 3 mm diameter

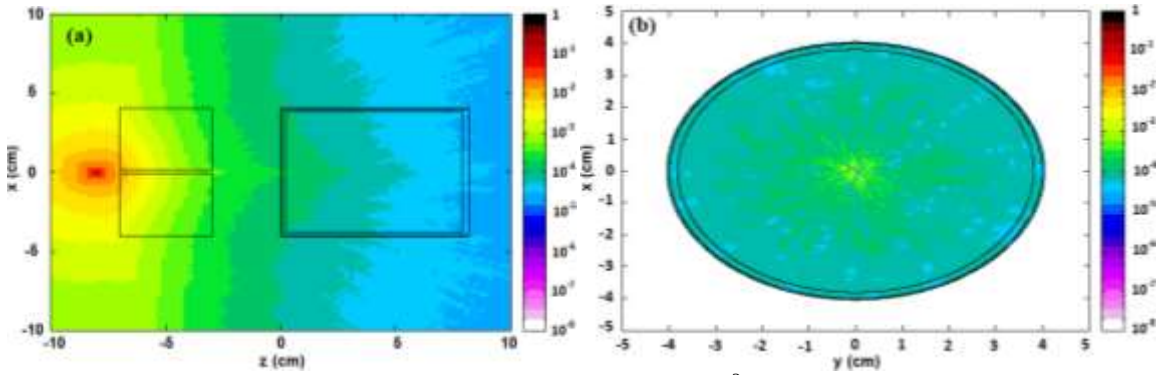

Figure 6. Two-dimensional drawing of photon fluence (photon/cm^2/primary photon) (a) in the simulation volume and (b) in the NaI(Tl) detector for 1332 keV photon beam and the collimator with 3 mm diameter

The variation of photon fluence in the simulation volume of 10x10x10 cm^3 and in the detector is given in Figure 5 and Figure 6 for 511 keV and 1332 keV photon beam, respectively. The color scale on the right side of the drawings shows the change of photon fluence. When the fluence values reaching the detector after passing through the collimator are compared, it is seen that the fluence value of the 511 keV photon beam is less than the 1332 keV photon control fluence value. This shows that the 511 keV photon beam is more likely to be absorbed in the lead collimator. As a result, it is understood that the 1332 keV energy beam reaching the detector by making elastic and inelastic scattering from the 3 mm diameter collimator in Figures 5 and 6 is more likely to interact with the detector crystal. This explains the fact that the detector efficiency of the 1332 keV photon beam is higher than the 511 keV photon beam.

3.2. Effect of beam collimation on gamma attenuation coefficient

The details of the geometry used for the calculation of the linear attenuation coefficient are given in Figure 3. The linear attenuation coefficient was calculated from the slope of the graph of ln (I_0/I) obtained from FLUKA code against different thicknesses of the Al up to 1 cm. Table 1 shows the linear attenuation coefficients calculated for the Al and the 511 keV and 1332 keV energies. Variation of linear attenuation coefficient depending on collimator diameters of 3, 5, 7, and 10 mm was investigated. The reason for comparison with XCOM values is to show that the value range of linear attenuation coefficient calculated by FLUKA code for different collimator diameters is compatible with XCOM [17] which, is a database that calculates the mass attenuation coefficient at 1 keV-1 GeV photon energy.

It is seen from the results in Table 1 that the variation due to the collimator diameter is very small and although not all diameters, the attenuation coefficient is higher in low diameters. In addition, the results are in agreement with the XCOM values. The purpose of beam collimation is to make the isotropic distribution of the gamma source into a narrow beam and to minimize the scattering of photons reaching the detector. However, the change in linear attenuation coefficients is since all photons producing elastic and inelastic scattering are counted below the full energy peak.

Table 1. Linear attenuation coefficients (cm^{-1}) calculated from collimators with diameters of 3, 5, 7 and 10 mm for Al

Absorber material	Energy (keV)	Linear attenuation coefficients, μ (cm^{-1})				
		3 mm	5 mm	7 mm	10 mm	XCOM
Al	511	0.2371	0.2334	0.2749	0.2183	0.2259
	1332	0.1283	0.1382	0.1229	0.1394	0.1437

4. Conclusion and Suggestions

The details of the simulation defined by FLUKA code to examine the effect of beam collimation on the NaI (Tl) detector system are given in Figure 1-3. The effect of collimator diameter on the number below the full energy peak was investigated. It was observed that full energy peak efficiency increased with the increasing diameter of the collimator. It was determined that full energy peak efficiency in small collimator diameters was less than 1332 keV at 511 keV. Linear attenuation coefficients for Al metal and varying collimator diameters were calculated by FLUKA code. Although a narrow beam was obtained, changes in linear attenuation coefficients were observed due to scattering after interacting with the absorber material. As a result, it has been shown that geometric design plays an important role in the studies using NaI(Tl) detector system.

The using of collimator minimizes scattering by making the point source with the isotropic distribution into a pencil beam. However, the radius and length of the collimator used must be carefully selected as this will affect the number of photons entering the detector. Absorption of the low-energy radiation source through the collimator may result in unexpected reductions in detector efficiency. Scattering occurs after the collimated beam and the target material interact. Since these scattered photons are also detected in the detector system, the use of a secondary collimator can prevent this. In addition to this study, in future studies such a system can be constructed with different collimator designs and materials and its effect with the FLUKA code can be investigated.

References

[1] Akkurt I., Akyıldırım H., Mavi B., Kilincarslan S., Basyigit C. 2010. Photon attenuation coefficients of concrete includes barite in different rate. Annals of Nuclear Energy, 37: 910–914.

[2] Erdem M., Baykara O., Doğru M., Kuluöztürk F. 2010. A novel shielding material prepared from solid waste containing lead for gamma ray. Radiation Physics and Chemistry, 79: 917–922.

[3] Demir N., Akar Tarim U., Gurler O. 2017. Application of FLUKA code to gamma-ray attenuation, energy deposition and 35öşe calculations. International Journal of Radiation Research, 15 (1): 123-128.

[4] Medhat M.E., Demir N., Tarim Akar U., Gurler O. 2014. Calculation of gamma-ray mass attenuation coefficients of some Egyptian soil samples using Monte Carlo methods. Radiation Effects & Defects in Solids, 169 (8): 706–714.

[5] Ozyurt O., Altinsoy N., Karaaslan Ş.İ., Bora A., Buyuk B., Erk İ. 2018. Calculation of gamma ray attenuation coefficients of some granite samples using a Monte Carlo simulation code. Radiation Physics and Chemistry, 144: 271–275.

[6] Tekin H.O. 2016. MCNP-X Monte Carlo Code Application for Mass Attenuation Coefficients of Concrete at Different Energies by Modeling 3 × 3 Inch NaI(Tl) Detector and Comparison with XCOM and Monte Carlo Data. Hindawi Publishing Corporation Science and Technology of Nuclear Installations, 7 pages.

[7] Tekin H.O., Singh V.P., Manici T., Altunsoy E.E. 2017. Validation of MCNPX with Experimental Results of Mass Attenuation Coefficients for Cement, Gypsum and Mixture. Journal of Radiation Protection and Research, 42 (3): 154-157.

[8] Sidhu G.S, Singh K., Singh P.S., Mudahar G.S. 1999. Effect of collimator size and absorber thickness on gamma ray attenuation measurements for bakelite and perspex. Pramana – J. Phys., 53 (5).

[9] Ladhaf B.M., Pawar P.P. 2016. Effect of Absorber Concentration and Collimator Size on Gamma Ray Attenuation Measurements. International Journal of Engineering Technology Science and Research, 3 (3).
[10] Çelik N., Özen S.A., Demirtas Ö.F., Çevik U. 2018. The effect of energy resolution of detection instrument on mass attenuation coefficient Journal of Instrumentation, 13: P10012.
[11] Çelik N., Çevik U., Çelik A. 2012. Effect of detector collimation on the measured mass attenuation coefficients of some elements for 59.5–661.6 keV gamma-rays. Nuclear Instruments and Methods in Physics Research B, 281: 8–14.
[12] Tam H.D., Yen N.T.H., Tran L.B., Chuong H.D., Thanh T.T. 2017. Optimization of the Monte Carlo simulation model of NaI(Tl) detector by Geant4 code. Applied Radiation and Isotopes, 130: 75–79.
[13] Ferrari A., Sala P.R., Fasso A., Ranft J. 2005. FLUKA: a multi-particle transport code. CERN-2005-10, INFN/TC_05/11, SLAC-R-773.
[14] Shi H.-X., Chen B.-X., Li T.-Z., Yun D. 2002. Precise Monte Carlo simulation of gamma-ray response functions for an NaI(Tl) detector. Applied Radiation and Isotopes, 57: 517–524.
[15] Vlachoudis, V. 2009. FLAIR: A Powerful but User Friendly Graphical Interface for FLUKA. Proc. Int. Conf. on Mathematics, Computational Methods & Reactor Physics, Saratoga Springs, New York.
[16] Akkurt I., Gunoglu K., Arda S.S. 2014. Detection Efficiency of NaI(Tl) Detector in 511–1332 keV Energy Range. Science and Technology of Nuclear Installations, 2014: 5 pages.
[17] Berger M. J., Hubbell J.H. NBSIR 87-3597. 1987. Photon cross sections on a personal computer. National Institute of Standards, Gaithersburg, MD, USA.

Araştırma Makalesi / Research Article

The Determination of the Total Efficiency for NaI(Tl) Detector by GATE Simulation

Nuray YAVUZKANAT[1*], Didem GÜNGÜR[2], Sezai YALÇIN[1]

[1]Bitlis Eren University, Department of Physics, Bitlis
[2]Bitlis Eren University, Graduate School of Natural and Applied Sciences, Bitlis
(ORCID: 0000-0001-5055-9185) (ORCID: 0000-0003-2742-1094) (ORCID: 0000-0001-6779-9230)

Abstract
In this study the total efficiency of the NaI(Tl) detector have been calculated by using Geant4 based GATE simulation program. The simulation was performed using point and disc isotropic gamma-ray sources at various distance between source and detector in the photon energy range 50-3000 keV. Results were compared with different analytical and Monte Carlo calculations obtained in the time of the periods 1958-2018. The calculated and simulated data indicated good agreement with finding more sensitive GATE simulation result in the lower energy range from 50 keV to 150 keV.

Keywords: NaI(Tl), Total Efficiency, Geant4, GATE.

NaI(Tl) Dedektörünün GATE Simülasyon Programıyla Toplam Veriminin Belirlenmesi

Öz
Bu çalışmada Geant4 tabanlı GATE simulasyon programı kullanılarak NaI(Tl) detektörünün toplam verimi hesaplanmıştır. Simulasyon, 50-3000 keV foton enerji aralığında çeşitli kaynak-detektör uzaklıklarında izotropik nokta ve disk gama ışını kaynağı kullanılarak gerçekleştirilmiştir. Sonuçlar, 1958-2018 periyodu boyunca elde edilen farklı analitik ve Monte Carlo hesaplamaları sonuçları ile karşılaştırılmıştır. Hesaplanan ve GATE simulasyonuyla elde edilen sonuçların birbiriyle uyumlu çıkmasının yanında, bu çalışmada 50 keV ile 150 keV arasındaki düşük enerjideki gamalar için çok daha hassas sonuçlar bulunmuştur.

Anahtar kelimeler: NaI(Tl), Toplam Verim, Geant4, GATE.

1. Introduction

Scintillation detectors are the main class of radiation detectors used in many areas (eg in high energy physics, nuclear physics, nuclear medicine, industry, security, geology, astrophysics, agriculture, radiation measurement of environmental samples, etc.) [1-4]. Hofstadter in 1948 firstly showed that thallium-activated sodium iodide crystals (NaI(Tl)) combining with PMTs (Photomultiplier Tubes) used as an efficient detector to measure gamma-rays and other ionizing radiations [5]. Therefore, NaI(Tl) is the first solid-state detector used as a gamma-ray spectrometer in the 50s and after that time it is still the most common gamma-ray detector system [6]. NaI(Tl) is a highly popular detector due to its good efficiency, wide operating temperature range, low consumption and low costs, as well as in-suit radioactivity measurements [7,8]. Today it is the most important part of nuclear medicine (used in mammography, gamma cameras, and positron emission tomography) as well as astrophysics. The NaI (T1) detectors are also used in the measurement of the environmental radioactivity in the marine as used in the Fukushima nuclear accident [9].

*Sorumlu yazar: nyavuzkanat@beu.edu.tr
Geliş Tarihi: 20.11.2019, Kabul Tarihi:19.12.2019

The most important properties of the radiation detector are the detector response function, the total efficiency (TE), the full energy peak efficiency (FEPE) and the detector resolution. It is necessary to determine the detector properties to make gamma- ray measurements over a wide energy range. In the gamma-ray activity measurement, there are two critical properties in detector efficiency; total efficiency and full energy peak energy efficiency. To measure the absolute activities from the gamma-ray source over a wide energy range, the total efficiency needs to be known. The total efficiency is described by four different methods as experimental, empirical, analytical and Monte Carlo approach [10]. It is necessary to use standard sources to determine the total efficiency in the experimental method. These standard sources are quite expensive and require time to prepare in the laboratory [11]. It is also difficult to find standard gamma sources in the desirable energy range. Instead of the determination of the total detector efficiency by the experimental method, it is easy to fit the measurement values by analytical function or use the computer program based on the gamma-rays interactions with the detector [12]. One of the important analytical methods calculates the efficiency via identifying the average chord length which is called Mean Chord Length (MLC) [13,14]. In addition to experimental and computer-based calculations, new published analytical studies are directly calculated the detector efficiency for various detector-source arrangements [10,15-17].

Monte Carlo (MC) simulation method, used in many fields from the medical physics to particle physics and keeps its popularity. Nowadays it is widely used to calculate the application parameters such as the activity measurement, the detector efficiency, coincidence summing corrective factor in gamma-ray spectroscopy. Well-known multi-purpose MC codes are PENELOPE, MCNP, Geant4, GATE, FLUKA, EGS, etc. [18].

GATE is an advanced open- source software developed by international collaborations and dedicated to the medical applications and radiotherapy. Recently it plays a key role in terms of designing new medical devices, acquisition protocols, quality control systems of the medical imaging devices and image reconstructions. It is also used in the characterization of the detector system which is the most important part of the positron emission tomography (PET), etc. GATE runs with Geant4 simulation toolkit which is the validated physics models, complex geometrical volume description and powerful 3D visualization (such as Qt mode) [8, 19-23].

In this study, the total efficiency of the NaI(Tl) detector was obtained using the Geant4 based GATE simulation program. The simulation code was modeled for 3”x3” and 2”x2” cylindrical NaI(Tl) detector systems and obtained the output as a root file for every gamma-ray energy from 50 keV to 3000 keV. A simulated energy spectrum was used to calculate the total efficiency of the detector and compared the result with published results by using analytical and MC calculations. Founded the total efficiency values with GATE simulation were found to agree with the literature.

2. Material and Method

Modeled GATE (Geant4 Application for Tomographic Emission) Simulation

We simulated the photon detection efficiency of the NaI(Tl) detector with Geant4 based GATE simulation program. The simulation was performed using the different shapes of the sources at various distances (between source and detector) in the photon energy range 50-3000 keV. The versions of the GATE and Geant4 were 8.0 and 10.3 respectively. Firstly, a cylindrical NaI(Tl) detector was defined as a three-inch length and three-inch diameter. The point source was positioned at 0.001, 0.5 and 10 cm distance from the detector surface. The disc source was also determined in the simulation with a radius of 3.18 cm and located at 3 and 10 cm away from the detector surface. Moreover, 2”x2” NaI(Tl) detector was also defined in the simulation and calculated the total efficiencies of the detector for 0.001, 5 and 10 cm detector-source distance to compare the result with the current publication. Simulation setup and disc source visualization in Geant4 is shown in Figure 1.

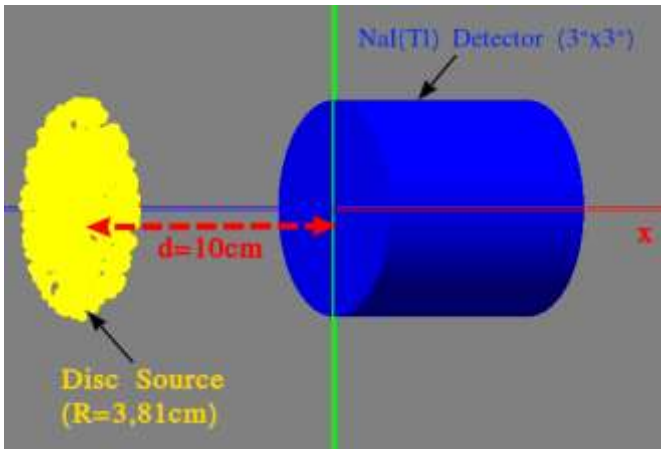

Figure 1. Geant4 visualization of the simulation setup for detecting gamma-rays emitting from disc source. Blue cylinder volume was defined for NaI(Tl) scintillation material with the size of 3"x3". Yellow points represent the disc source with radius of R=3.81 cm

In Figure 2, gamma-rays irradiated from the disc source located at 10 cm distance from the detector. Short red lines represent the travel distance of the electron that occurs after the interaction between scintillation and gamma-rays. Green long lines classically represent the photons in the Geant4.

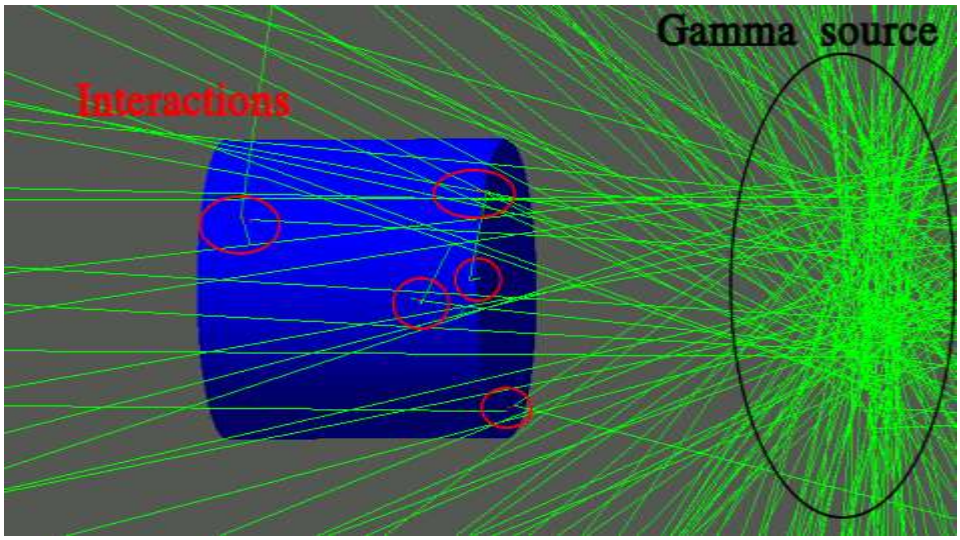

Figure 2. Green lines which is coming from the disc source (showing with black circle in the fig.) represent gamma rays in Geant4 simulation. Red circles in the figure show the interactions between scintillation and gamma-rays. Red lines indicate the electrons in the Geant4 simulation. In the simulation, detector volume was also capsuled with thin aluminum layer

Secondly, the physics list was chosen according to the photons energy range, therefore the physics-list builder name was called emstandard (electromagnetic physics-list) provided by the Geant4. After defining the system, source, digitization, and readout parameters, lastly, we described the data output as a root file that give all functionalities to achieve big data processing, numerical analysis and storage [30]. All occurred data outputs in the simulation were analyzed by ROOT software. The energy spectrum was obtained from the GATE simulation by recording all the interactions and the deposit energy of the detector crystal. Total efficiencies were calculated using the following equation:

$$TotalEfficiency = \frac{N_D}{N} \quad (1)$$

where N_D is the number of the detected photons by the scintillation, and N represents the number of photons emitted by the source. The net count of the emitted photons was stabilized with one million gamma-rays for each different case in the simulation. Detected photon number was found from the energy spectrum and all results were listed in the Table 1 and Table 2.

3. Result and Discussion

The total gamma efficiencies of the NaI(Tl) detector for the disk and point sources were evaluated at a different detector-source distances in the various energy ranges from 50 keV to 3000 keV. The total photon efficiencies for the disk and point sources obtained from the GATE simulation were compared with the calculated efficiencies by various analytical Monte Carlo approaches over the time period (between 1958 and 2018). In Table 1, there is a comparison between simulation with GATE and analytical calculations for NaI(Tl) detector's photon efficiency. In that part of the simulation, the disc source radius was defined as a 3.81 cm and located at two different positions (3 and 10 cm away from the detector surface). The analytical calculations and simulation results showed in good agreement. Especially, present work results consistent with the hybrid Monte Carlo method results calculated by [3]. Figure 3 shows that comparison between this work with different analytical methods and Monte Carlo techniques in terms of the total photon efficiencies for NaI(Tl) scintillator in the energy range between 50 keV and 3000 keV. In the Figure 3 (b) there is a slight discrepancy over the 1332 keV between this work and others (exception of the [3] and [27] works).

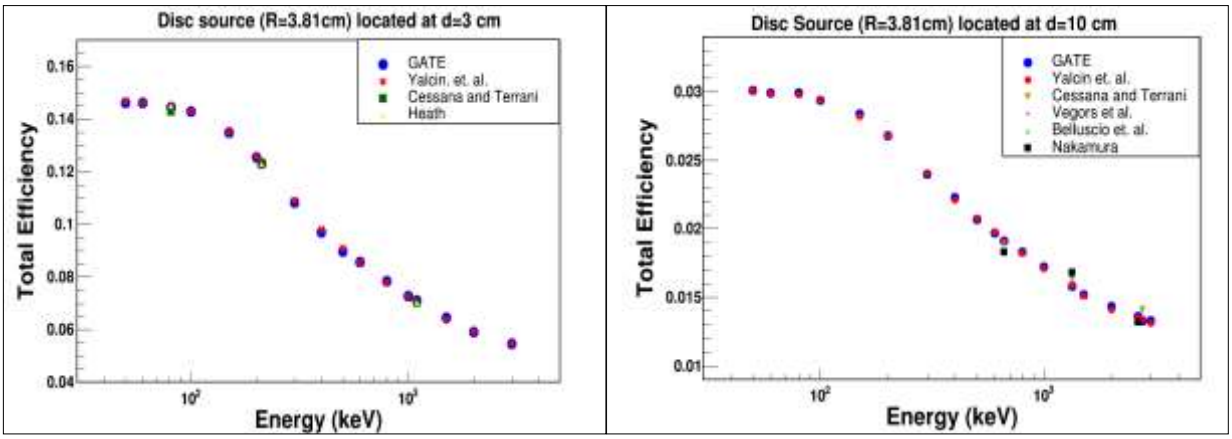

Figure 3. Total photon efficiency for a 3"x3" NaI(Tl) scintillator with a 3.18 cm radius disc source positioned at (a) 3 cm and (b) 10 cm distance between source and the detector surface

In Table 2, Geant4 based GATE simulation result for point source is compared with an analytical and different types of Monte Carlo calculations in total photon efficiency of the NaI(Tl) detector. The point source was positioned at three different places with 0.001, 0.5 and 10 cm away from the detector. The analytical calculation (except Mean Chord Length) and different types of Monte Carlo calculations consistent with GATE simulation results. Figure 4 also indicates that the comparison between this study and different analytical methods or Monte Carlo techniques. In the Figure 4 (a), (b) and (c), the divergence between MCL method results and other values rises from the position of 0.001cm to 10 cm. It is obvious that present work with obtained GATE simulation in the lower energies is having more precisely calculation than other studies, because their values are identical until the 200 keV energy. It is clearly seen in Figure 3 and Figure 4 that the total photon efficiency decreases with increasing the distance between the detector and the source. It causes most likely changing the solid angle by reducing the detector source distance, therefore, more photons interact with the scintillation.

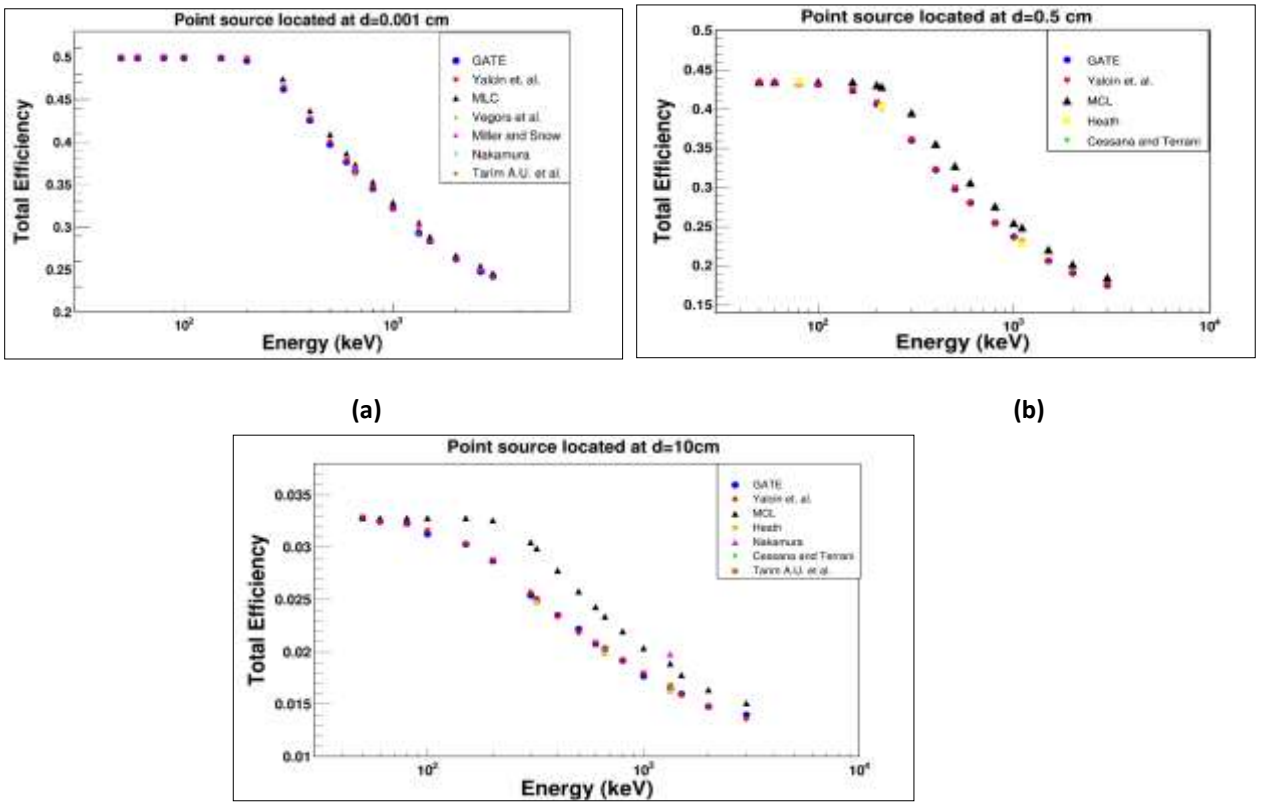

Figure 4. Total efficiency for a 3"x3" NaI(Tl) scintillator with a point source positioned at **(a)** 0.001 cm **(b)** 0.5 cm and **(c)** 10 cm distance between source and the detector surface

Table 1. Total counting efficiency values for a 3" x 3" NaI(Tl) detector with disc source (R=3.81 cm) located at d=3 and 10 cm

Energy (keV)	Total Efficiency									
	Present Work		Yalcin et al.[3]		Cessana A. and Terrani M.[24]		Nakamura T. [25]	Belluscio et al. [26]	Heath R.L. [28]	Vegors et al.[27]
	3	10	3	10	3	10	10	10	3	10
50	0.1462	0.0301	0.1466	0.0301	-	-	-	-	-	-
60	0.1462	0.0299	0.1462	0.0299	-	-	-	-	-	-
80	-	0.0299	-	0.0298	-	-	-	-	-	-
81	0.1445	-	0.1448	-	0.143	-	-	-	0.145	-
100	0.1429	0.0294	0.1428	0.0294	-	-	-	-	-	-
150	0.1348	0.0284	0.1352	0.0282	-	-	-	-	-	-
200	0.1255	0.0268	0.1257	0.0268	-	-	-	-	-	-
212	0.1231	-	0.1236	-	0.123	-	-	-	0.123	-
300	0.1084	0.024	0.1090	0.0241	-	-	-	-	-	-
400	0.0971	0.0223	0.0979	0.0221	-	-	-	-	-	-
500	0.0898	0.0207	0.0908	0.0208	-	-	-	-	-	-
600	0.0857	0.0197	0.0855	0.0198	-	-	-	-	-	-
661	-	0.0191	-	0.0191	-	0.0191	0.0183	0.019	-	-
800	0.0784	0.0183	0.078	0.0182	-	-	-	-	-	-
1000	0.0728	0.0172	0.0726	0.0171	-	-	-	-	-	-
1100	0.0711	-	0.0711	-	0.0701	-	-	-	0.0702	-
1332	-	0.0158	-	0.0159	-	0.0164	0.0168	0.0164	-	0.0156
1500	0.0646	0.0152	0.0639	0.0151	-	-	-	-	-	-
2000	0.0591	0.0143	0.0591	0.0141	-	-	-	-	-	-
2620	-	0.0136	-	0.0135	-	-	0.0132	-	-	0.0133
2750	-	0.0133	-	0.0134	-	0.0141	-	0.0141	-	-
3000	0.0546	0.0133	0.0546	0.0131	-	-	-		-	-

Table 2. Total counting efficiency values for a 3" x 3" NaI(Tl) detector with point source located at d=0.001, 0.5 and 10 cm

Energy (keV)	Total Efficiency																					
	Present Work			Özmutlu C. and Ortaovalı A.Z. [13]			Yalcin et al.[3]			Tarım A.U. et al. [4]		Nakamura T. [25]		Cessana A. and Terrani M.[24]		Heath R.L. [28]		Belluscio et al. [26]	Miller and Snow[29]	Vegors et al.[27]
	0.001	0.5	10	0.001	0.5	10	0.001	0.5	10	0.001	10	0.001	10	0.5	10	0.5	10	10	0.001	0.001
50	0.4990	0.4347	0.0328	0.4999	0.4349	0.0328	-	-	-			-	-	-	-	-	-	-	-	-
60	0.4990	0.4345	0.0325	0.4999	0.4349	0.0328	-	-	-			-	-	-	-	-	-	-	-	-
80	0.4992	0.4335	0.0323	0.4999	0.4349	0.0328	-	0.4333	-			-	-	0.435	-	0.435	-	-	-	-
100	0.4995	0.4318	0.0313	0.4999	0.4349	0.0328	-	-	-			-	-	-	-	-	-	-	-	-
150	0.4991	0.4240	0.0303	0.4999	0.4349	0.0328	-	-	-			-	-	-	-	-	-	-	-	-
200	0.4957	0.4068	0.0287	0.4984	0.4312	0.0326	-	-	-			-	-	-	-	-	-	-	-	-
212	-	0.4022	-	-	0.4289	-	-	0.4013				-	-	0.404	-	0.403	-	-	-	-
300	0.4625	0.3601	0.0254	0.4732	0.3954	0.0305	-	-	-			-	-	-	-	-	-	-	-	-
320	-	-	0.0249	-	-	0.0299	-	-	0.0249			-	-	-	0.0251	-	0.0247	0.025	-	-
400	0.4257	0.3226	0.0235	0.4374	0.3557	0.0278	-	-	-			-	-	-	-	-	-	-	-	-
500	0.3975	0.2980	0.0222	0.4095	0.3277	0.0258	-	-	-			-	-	-	-	-	-	-	-	-
600	0.3770	0.2808	0.0208	0.387	0.3063	0.0243	-	-	-			-	-	-	-	-	-	-	-	-
661	0.3660	-	-	0.3741	-	-	0.3646	-	-	0.3652	0.0202	0.367	-	-	-	-	-	-	0.370	0.362
662	-	-	0.0203	-	-	0.0234	-	-	0.0202			-	0.0183	-	0.0201	-	0.0198	0.019	-	-
800	0.3453	0.2546	0.0192	0.3537	0.276	0.022	-	-	-			-	-	-	-	-	-	-	-	-
1000	0.3227	0.2376	0.0177	0.3298	0.255	0.0204	-	-	-			-	-	-	-	-	-	-	-	-
1100	-	0.2292	-	-	0.249	-	-	0.2281	-			-	-	0.229	-	0.228	-	-	-	-
1330	-	-	0.0165	-	-	0.0189	-	-	0.0164			-	0.0168		0.0165		0.0162	0.0164	-	-
1332	0.2929	-	-	0.3057	-	-	0.2930	-	-	0.2990	0.0168	0.296	-	-	-	-	-	-	0.302	0.293
1500	0.2841	0.2066	0.0160	0.2895	0.2208	0.0178	-	-	-			-	-	-	-	-	-	-	-	-
2000	0.2628	0.1910	0.0148	0.2671	0.2023	0.0164	-	-	-			-	-	-	-	-	-	-	-	-
2620	0.2478	-	-	0.255	-	-	0.2476	-	0.0140			0.249	-	-	-	-	-	-	0.250	0.248
3000	0.2424	0.1755	0.0140	0.2464	0.1855	0.0151	-	-	-			-	-	-	-	-	-	-	-	-

In figure 5 there is a comparison between recently published efficiency values obtained from a simple computational Monte Carlo algorithm (developed by Tarım et. al.) and Geant4 based GATE simulation results. In this part of the simulation 2"x2" cylindrical NaI(Tl) detector system was defined and three different source-detector distance was used (0.001, 5 and 10 cm). It is clearly seen that the calculated and simulated values of the efficiencies for NaI(Tl) detector indicated good agreement.

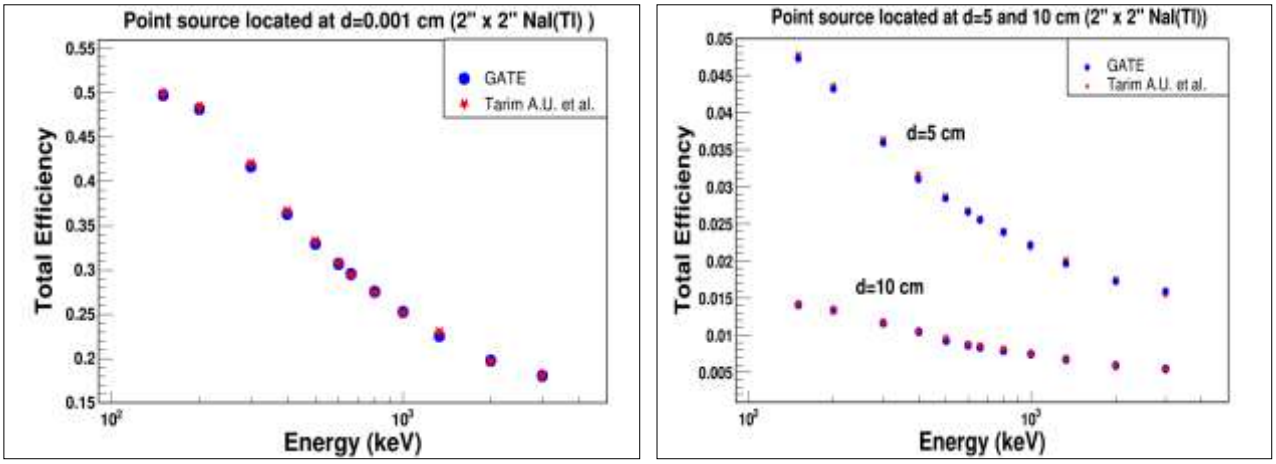

(a) **(b)**

Figure 5. Total efficiency for a 2"x2" NaI(Tl) scintillation detector with a point source positioned at **(a)** 0.001 cm **(b)** 5 cm and 10 cm distance between source and the detector surface

4. Conclusion

In this study, the total efficiency of the cylindrical NaI(Tl) (3" x 3") and (2" x 2") detectors have been calculated for isotropic point and disc gamma-rays source by using Geant4 based GATE simulation program. To compare our results with other different analytical and Monte Carlo calculation results we have evaluated the efficiencies in the photon energy range 50-3000 keV and for 0.001 cm, 3 cm, 5 cm and 10 cm distance between the source and the detector. The results are shown in table 1, table 2 and figures the agreement is quite good in the whole energy range. However, we can say that Geant4 gives more sensitive results in the low energetic photon (between 50 and 200 keV).

References

[1] Zazubovich S. 2001. Physics of halide scintillators. Radiation Measurements, 33 (5): 699-704.

[2] Mouhtia I., Elaniquea A., Messousb M.Y., Benahmedb A., McFeec J.E., Elgouba Y., Griffithd P. 2019. Characterization of CsI(Tl) and LYSO(Ce) scintillator detectors by measurements and Monte Carlo simulations. Applied Radiation and Isotopes, 154 (108878): 1-7.

[3] Yalcin S., Gurler O., Kaynak G., Gundogdu O. 2007. Calculation of total counting efficiency of a NaI(Tl) detector by hybrid Monte-Carlo method for point and disc sources. Applied Radiation and Isotopes, 65: 1179-1186.

[4] Tarım Akar U., Gürler O., Yalçın S. 2018. A Quick Method to Calculate NaI(Tl) Detector Efficiency Depending on Gamma ray Energy and Source-to-detector Distance. Celal Bayar University Journal of Science, 14 (2): 195-199.

[5] Hofstadter R. 1949. The Detection of Gamma-Rays with Thallium-Activated Sodium Iodide Crystals. Physical Review, 75 (5): 796-810.

[6] Pilakouta M., Pappa F.K., Patiris D.L., Tsabaris C., Kalfas C.A. 2018. A methodology for expanding the use of NaI(Tl) based spectrometry in environmental radioactivity measurements. Applied Radiation and Isotopes, 139: 159-168.

[7] Zhang Y., Li C., Liu D., Zhang Y., Liu Y., 2015. Monte Carlo simulation of a NaI(Tl) detector for in situ radioactivity measurements in the marine environment. Applied Radiation and Isotopes, 98: 44-48.
[8] Duc Tam H., Hai Yen N.T., Tran, L.B., Dinh Chuong, H., Thien Thanh, T. 2017. Optimization of the Monte Carlo simulation model of NaI(Tl) detector by Geant4 code. Applied Radiation and Isotopes, 130: 75–79.
[9] Wang J., Zhang Y., Liu D., Wu B., Zhang Y., Jiang H., 2018. Automated spectra analysis of in situ radioactivity measurements in the marine environment using NaI(Tl) detector. Applied Radiation and Isotopes, 141: 88–94.
[10] Hamzawy A., 2010. Simple analytical formula to calculate γ-ray cylindrical detectors efficiencies. Nuclear Instruments and Methods in Physics Research Section A, 624 (1): 124-129.
[11] Chuong H.D., Nguyen Q.H., Nguyen T.M.L., Nguyen V.H. 2019. Validation of gamma scanning method for optimizing NaI(Tl) detector model in Monte Carlo simulation. Applied Radiation and Isotopes, 149: 1-8
[12] Zikovsky L., Chah B. 1988. A computer program for calculating Ge(li) detector counting efficiencies with large volume samples. Nuclear Instruments and Methods in Physics Research, A263 (2-3): 483-486.
[13] Özmutlu C., Ortaovalı A.Z. 1976. Calculation of total and full energy peak efficiencies of Ge(Li) and NaI(Tl) detectors by introducing the mean chord length. Nuclear Instruments and Methods, 149-155.
[14] Selim Y.S., Abbas M.I., Fawzy M.A. 1998. Analytical calculation of the efficiencies of gamma scintillators. Part I: Total efficiency for coaxial disk sources. Radiation Physics and Chemistry, 53: 589-592.
[15] Abbas M.I. 2010, A new analytical method to calibrate cylindrical phoswich and LaBr3(Ce)scintillation detectors. Nuclear Instruments and Methods in Physics Research A, 621: 413-418.
[16] Abbas M.I., Noureddeen S. 2011. Analytical expression to calculate total and full-energy peak efficiencies for cylindrical phoswich and lanthanum bromide scintillation detectors. Radiation Measurement, 46: 440-445
[17] Pomme S. 2009. Detection efficiency calculation for photons, electrons and positrons in a well detector. Part I: Analytical model. Nuclear Instruments and Methods in Physics Research A, 604: 584-591.
[18] Lépy M.C. et al. 2019. A benchmark for Monte Carlo simulation in gamma-ray spectrometry. Applied Radiation and Isotopes, 154 (108850): 1-7
[19] Ashrafi S., Anvarian S., Sobhanian S. 2006. Monte-Carlo modeling of a NaI(Tl) scintillator. Journal of Radioanalytical and Nuclear Chemistry, 269 (1): 95–98.
[20] Garnett R., Prestwich W.V., Atanackovic J., Wong M., Byun S.H. 2017. Characterization of a LaBr3(Ce) detector for gamma-ray spectrometry for CANDU power reactors. Radiation Measurements, 106: 628-631.
[21] Zhang J., Zhang P., Zhang Y., Yang J., Yuan G., Song X., Li X., Zhou Y. 2019. Geant4 simulation study on detection efficiencies of the Compton suppression system at the HL-2A tokamak. Applied Radiation and Isotopes, 150: 63-69.
[22] Wirawan R., Angraini L.M., Qomariyah N., Waris A., Djamal M. 2020. Gamma backscattering analysis of flaw types and orientation based on Monte Carlo Geant4 simulations. Applied Radiation and Isotopes, 155 (108924): 1-7.
[23] Open Gate Collaboration "Users Guide V8.0 From Wiki OpenGATE". 2018. http://www.opengatecollaboration.org/sites/default/files/GATE-UsersGuideV8.0.pdf (Accessed July 2018).
[24] Cesana A., Terrani M. 1977. Gamma-ray Activity Determination in Large Volume Samples with a Ge-Li Detector. Analytical Chemistry, 49 (8): 1156-1159.
[25] Nakamura T. 1972. Monte Carlo calculation of efficiencies and response functions of NaI(Tl) crystals for thick disk gam-ray sources and its application to Ge(Li) detectors. Nuclear Instruments and Methods, 105: 77-89.

[26] Belluscio M., DeLeo R., Pantaleo A., Vox A. 1974. Efficiencies and response functions of NaI(T1) crystals for gamma rays from thick disk sources. Nuclear Instruments and Methods, 118: 553-563.
[27] Vegors Jr, S.H, Marsden, L.L, Heath, R.L. 1958. Calculated efficiencies of cylindrical radiation detectors. AEC Research and Development Report, 1958, IDO-16370.
[28] Heath R.L. 1964. Scintillation spectrometry. Vol. 1, IDO-16880-1.
[29] Miller W.F., Snow W.J., 1961. NaI and CsI efficiencies and photofractions for gamma-ray detection. Nucleonics, 19 (11): 174.
[30] ROOT Date Analysis Framework user's guide. 2018. https://root.cern.ch/root/htmldoc/guides/users-guide/ROOTUsersGuide.html (Accessed September 2018).

Araştırma Makalesi / Research Article

Evaluation of the Lifetime Cancer Risk Due to Natural Radioactivity in Tap Water Consumed in Nevşehir Province, Turkey

Aybaba HANÇERLİOĞULLARI*, Şeref TURHAN, Aslı KURNAZ

Kastomunu University, Faculty of Science and Letters, Department of Physics, 37150, Kastamonu, Turkey
(ORCID: 0000-0001-7008-480X)(ORCID: 0000-0001-5303-3680) (ORCID: 0000-0002-7910-3461)

Abstract
Ionizing radiations (α-, β- and γ- rays) emitted from radionuclides in waters can produce detrimental biological effects for human health. The excess lifetime cancer risk (ELCR) relates to the probability of developing cancer over a life-time at a given annual exposure dose rate. In this study, the excess lifetime cancer risk was evaluated for adults living in Nevşehir province based on the contents of gross alpha and gross beta in tap water samples collected from various districts in Nevşehir. The values of the excess lifetime cancer risk varied 1.7 x 10^{-4} to 1.3 x 10^{-3} with an average of 5.5 x 10^{-4}. Consequently, the ELCR values via tap water consumption were found below the acceptable limit of 10^{-3} for radiological risk.

Keywords: Tap water, The excess lifetime cancer risk, Nevşehir.

Türkiye Nevşehir İlinde Tüketilen Musluk Suyunda Doğal Radyoaktivite Nedeniyle Yaşam Boyu Kanser Riskinin Değerlendirilmesi

Öz
Sularda radyonüklitlerden yayılan iyonlaştırıcı radyasyonlar (α-, β- ve rays-ışınları) insan sağlığı için zararlı biyolojik etkiler yaratabilir. Yaşam boyu kanser riski (ELCR), verilen yıllık maruz kalınan doz oranında yaşam boyu kanser gelişme olasılığı ile ilişkilidir. Bu çalışmada, Nevşehir ilinde yaşayan yetişkinler için yaşam boyu kanser riski, Nevşehir'in çeşitli ilçelerinden toplanan musluk suyu örneklerinde toplam alfa ve toplam beta içeriğine göre değerlendirilmiştir. Yaşam boyu kanser riskinin değerleri ortalama 5.5 x 10-4 olmak üzere 1.7x10-4 ile 1.3x10-3 arasında değişmiştir. Sonuç olarak, musluk suyu tüketimi yoluyla ELCR değerleri radyolojik risk için kabul edilebilir 10-3 sınırının altında bulunmuştur.

Anahtar kelimeler: Musluk suyu, Yaşam boyu kanser riski, Nevşehir

1. Introduction

Water is a necessary food for human life. Therefore, every effort that is applicable as safe as possible has been made by the WHO and the relevant institutions/organizations of each country to obtain drinking water [1]. Water pollution occurs when undesirable substances enter into water [1]. Diseases due to the pollution of drinking water cause serious problems in humans. Therefore, interventions to enhance the drinking water quality procure important health benefits.

The main sources of water pollution can be grouped into three groups as biological (microbial) pollutants, chemical pollutants, and radiological pollutants [2]. Some of these chemicals are (a) carcinogenic (b) perhaps carcinogenic, (c) possibly carcinogenic, (d) not classifiable as to its carcinogenicity and (e) likely not carcinogenic to humans [1]. Some chemical elements such as uranium, thorium, and potassium naturally occurring in the environment are radioactive [3]. In addition, the world is constantly bombarded by high-energy particles from both the sun and the outside of the solar system

*Sorumlu yazar: aybaba@kastamonu.edu.tr
Geliş Tarihi: 15.10.2019, Kabul Tarihi: 19.12.2019

known as cosmic radiation. Artificial radioactive sources consist of (a) radionuclides used for different purposes in medicine (diagnosis and treatment), agriculture and industrial activities and (b) radionuclides released directly into the atmosphere after a total of 543 atmospheric nuclear weapons conducted between 1945-1980 years and the nuclear power plant accidents [4]. In addition, radon (^{222}Rn) gas, which is a radioactive decay product of radium (^{226}Ra) in drinking water entering into the body through the respiratory tract, may increase the risk of lung cancer over time [4].

Risk evaluation is a method used to evaluate the likelihood that exposure to radionuclides will harm people or the environment. The purpose of this study is to evaluate the radiation risks due to the ingestion of tap water from different sources in Nevşehir province. Therefore, in this study, the annual effective radiation dose and ELCR caused by the natural radioactivity in tap water samples collected from Nevşehir province were estimated.

2. Material and Method

The ELCR was estimated based on the annual effective dose rate using the equation [5]:

$$ELCR = AEDR \times AHL \times FR, \quad (1)$$

where *AEDR* is the effective dose rate, *AHL* is the mean human life of 78 years for Turkish adult person and FR is risk factor given to be 0.057 per Sievert (Sv) for stochastic effects produced low background radiation [6]. In estimation of the ELCR, the values of AEDR were taken from the study performed Turhan et al. [7]. Also, the values of the AEDR varied from 38 to 288 μSv/y (average: 124 μSv/y) [7].

3. Results and Discussion

The excessive lifetime cancer risk due to alpha and beta emitting radionuclides in twenty-one tap water samples collected from Nevşehir city center are given in Table 1. It is seen from Table 1 that The CR values varied from 1.7 x 10^{-4} to 1.3 x 10^{-3} with an average of 5.5 x 10^{-4}. The highest value of the CR was estimated for tap water, TWS1 while the lowest value of the CR was estimated for tap water, TWS5. The ELCR average value is approximately three times lower than the world average of 1.6×10^{-3} while all CR values were below the world average value [3].

4. Conclusions

The aim of this study was to provide information for the Nevşehir region. The results obtained show that the ELCR values are lower than the world's mean value. The present study provides a general background and can be used as a baseline for future investigations.

Table 1. The excess lifetime cancer risk estimated for the tap water samples

Sample code	CR
TWS1	1.3 x 10^{-3}
TWS2	7.1 x 10^{-4}
TWS3	5.2 x 10^{-4}
TWS4	5.6 x 10^{-4}
TWS5	1.7 x 10^{-4}
TWS6	3.8 x 10^{-4}
TWS7	2.7 x 10^{-4}
TWS8	5.5 x 10^{-4}
TWS9	4.7 x 10^{-4}
TWS10	4.2 x 10^{-4}
TWS11	4.3 x 10^{-4}
TWS12	4.8 x 10^{-4}
TWS13	2.7 x 10^{-4}
TWS14	5.4 x 10^{-4}
TWS15	7.1 x 10^{-4}
TWS16	5.7 x 10^{-4}
TWS17	7.6 x 10^{-4}
TWS18	6.8 x 10^{-4}
TWS19	8.0 x 10^{-4}
TWS20	5.1 x 10^{-4}

TWS21	5.0×10^{-4}
Average	5.5×10^{-4}
Standard deviation	2.3×10^{-4}
Standard error	5.0×10^{-5}
Min	1.7×10^{-4}
Max	1.3×10^{-3}

References

[1] WHO (World Health Organization). 2011. Guidelines for Drinking-water Quality. 4th edition, WHO Library Cataloguing-in-Publication Data NLM classification: WA 675, Geneva.

[2] Zriba N. 2019. Determination of Radiological and Chemical Aspects of Packaged Drinking Waters Consumed in Cappadocia region. Kastamonu Üniversitesi, Fen Bilimleri Enstitüsü, Yüksek Lisans Tezi, Kastamonu.

[3] UNSCEAR (United Nations Scientific Committee on the Effects of Atomic Radiation). 2000. Sources and effects of ionizing radiation. United Nations Publication, New York, USA.

[4] Özçıtak E. 2012. Nevşehir ili ve ilçelerinde tüketilen içme ve kaplıca sularındaki radyoaktivitenin ölçülmesi. Nevşehir Ü, Fen Bilimleri Enstitüsü, Fizik Anabilim Dalı, Yüksek Lisans Tezi, Nevşehir.

[5] Ezekiel A.O. 2017. Assessment of excess lifetime cancer risk from gamma radiation levels in Effurun and Warri city of Delta state, Nigeria. Journal of Taibah University for Science, 11: 367-380.

[6] ICRP, 1991. 1990 Recommendations of the international commission on radiological protection. ICRP Publication 60, International Commission on Radiological Protection (ICRP). http://www.icrp.org/publication.asp?id=ICRP+Publication+60.

[7] Turhan Ş., Zriba N.A.E.M., Taşkın H., Yılmaz Z., Bayülken S., Hançerlioğulları A., Kurnaz A. 2019. Radiochemical analysis of bottled drinking waters consumed in Turkey and a risk assessment study. Microchemical Journal, 149.

Araştırma Makalesi / Research Article

Bitlis'te Yetişen Bazı Bitkilerde Radon Konsantrasyonlarının İstatistiksel Olarak Analizi

Sultan ŞAHİN BAL[1*], Önder KILIÇ[1], Fikriye GÖNÜLTAŞ[1], Murat KURŞAT[2], Nazlım Deniz ARAL[3], Seval ŞAHİN[4]

[1]*Bitlis Eren Üniversitesi, Fizik Bölümü, Bitlis*
[2]*Bitlis Eren Üniversitesi, Biyoloji Bölümü, Bitlis*
[3]*Bitlis Eren Üniversitesi, Matematik Bölümü, Bitlis*
[4]*Fırat Üniversitesi, İstatistik Bölümü, Elazığ*
(ORCID: 0000-0001-7896-0771) (ORCID:0000-00018948-3413) (ORCID:0000-0002-8514-7399) (ORCID:0000-0002-0861-4213) (ORCID: 0000-0002-8984-2620) (ORCID: 0000-0003-3467-4137

Öz
Bu çalışmada, Bitlis'te yetişen bazı bitkilerin radon (^{222}Rn) konsantrasyonlarının istatistiksel olarak analizi yapıldı. Radon konsantrasyonları Radosys radon ölçüm sistemi ile belirlendi. PR15 numaralı örneğin (*Urtica*) en yüksek radon konsantrasyonuna (997,67 ±28,90 Bq/m3) ve PR13 numaralı örneğin (*Polygonum cognatum*) en düşük radon konsantrasyonuna (255,70 ± 14,63 Bq/m3) sahip olduğu görülmüştür. Radon konsantrasyon seviyeleri ile lokasyonlar arasındaki ilişki istatiksel olarak incelenmiştir. Bu amaçla, varyans analizi (ANOVA) yöntemi kullanılmıştır.

Anahtar kelimeler: Bitkiler, Radon, İstatistik, Bitlis.

The Analyzing Statistically of Radon Concentrations in Some Plants Growing in Bitlis

Abstract
In this study, the analyzing statistically of radon (^{222}Rn) concentrations of some plant samples growing in Bitlis were made. The radon concentrations were determined with Radosys radon measurement system. It was seen that the sample with number PR15 (*Urtica*) has the highest radon concentration (997.67 ± 28.90 Bq /m^3) and the sample with number PR13 (*Polygonum cognatum*) has the lowest radon concentration (255.70 ± 14.63 Bq /m^3). It has been analyzed as statistically relationship between radon concentration levels with locations. With this purpose, it has been used method of Analysis of Variance (ANOVA).

Keywords: Plants, Radon, Statistic, Bitlis.

1. Giriş

Radon, doğal olarak oluşan, kokusuz, renksiz, tatsız, etkisiz olan doğal bir soy gazdır. ^{238}U, ^{235}U, ^{232}Th gibi doğal olarak oluşan radyo-çekirdeklerin bozunumundan sürekli olarak üretilir. ^{238}U'in bozulmasından üretilen ^{222}Rn izotopu, insan yaşamında maruz kaldığı iç radyasyonun ana kaynağıdır (yaklaşık % 55). ^{226}Ra radyum izotopunun bozunma ürünü olan ve gaz halinde bulunan radyoaktif radon (^{222}Rn), her türlü toprakta ve kayada bulunur. Radyum atomları toprak parçacıklarında bozunur, elde edilen radon atomları hava ile doldurulmuş gözeneklere girer ve daha sonra atmosfere salınmak için difüzyon yolu ile bu boşluktan yayılma ile taşınır [1, 2].

*Sorumlu yazar: sahin.sultan@gmail.com
Geliş Tarihi: 18.11.2019, Kabul Tarihi:19.12.2019

Zemin yüzeyinin birkaç metre içindeki toprak gazındaki radon konsantrasyonları, gözenek alanlarına ve daha sonra atmosfere radon giriş hızlarının belirlenmesinde önemlidir ve bu durum ana kayadaki radyum konsantrasyonuna ve toprağın geçirgenliğine bağlıdır [3].

Bütün canlılar iyonlaştırıcı radyasyona maruz kalır. Karasal radyasyon kaynağı, radyoaktif zincirlerdeki radyo-çekirdeklerin (^{238}U, ^{235}U ve ^{232}Th) bozunumlarından kaynaklanır [4-8]. Bu üç zincir, sırasıyla her biri 3,8235 gün (^{222}Rn), 3,9 s (^{219}Rn) ve 55,6 s (^{220}Rn) yarılanma ömrüne sahip; her zincir farklı bir radon izotopu içerir [8].

Radon (^{222}Rn) atmosferde yaygın olarak bulunur ve doğada en bol bulunan doğal radyoaktif gazdır [9]. Radon ve ürünleri, insan vücuduna solunduktan sonra, vücutta bozunma sırasında oluşan alfa parçacıkları hasarlı dokuların veya hücrelerin iyonlaşmasına neden olan (öncelikle akciğerde), DNA moleküllerinin yapısına zarar verir, hücreyi etkiler rejenerasyon süreci ve kromozomlarda bozulmalara neden olur, böylece kanser oluşma tetiklenir [3]. Uluslararası Kanser Araştırma Ajansı (IARC), radon ve ürünlerini Grup I kanserojen faktörler olarak sınıflandırmış ve Dünya Sağlık Örgütü (WHO), insanlarda 19 kanserojen faktörden biri olarak radonu listelemiştir [10, 11].

Bu çalışmada, Bitlis bölgesinde yetişen, genellikle tatlandırıcı ve şifa bulmak amacıyla sıkça tüketilen bazı bitki örneklerinin radon konsantrasyon seviyeleri belirlenmiş ve bu değerler ANOVA yöntemi kullanılarak istatistiksel olarak incelenmiştir.

2. Materyal ve Metot

2.1. Bitlis'in Genel Jeolojisi

Bitlis, Metamorfit bir yapıya sahiptir. Bitlis Metamorfitleri Epi Metamorfik örtünün Petrografisi: aşağıdan yukarıya doğru metamorfizma derecesi azalan 6 grup ayırtlaşmıştır. Bunlar; Alt yeşil şistler, Muskovitli Kuvarsitler, Kalkşistler, Rekristalize kireçtaşları, Üst yeşil Şistler, Rekrastilize karstik kireçtaşlarıdır [12-14].

2.2. Bitki Örneklerinin Analize Hazırlanması

Kurutulmuş bitki örnekleri, tamamen nemden arındırmak amacıyla alüminyum folyolara sarıldı ve 80 ^{0}C'de etüv içerisinde yaklaşık 24 saat bekletildi. Bu örnekler, 1 litrelik kavanozlar içerisine konuldu. Bu kavanozların kapakları sıkıca kapatılarak hava ile teması önlendi ve dışardan gelebilecek etkileri (ışık vb.) en aza indirmek için alüminyum folyo ile kaplanmıştır. Bitki örnekleri kavanozların içinde yaklaşık 30 gün boyunca radyoaktif dengenin sağlanması için bekletildi (Şekil 1).

Şekil 1. Bitki örneklerinin, radyoaktif dengenin sağlanması ve pozlanmanın olması için bekletilmesi.

2.3. Radon Konsantrasyon Seviyelerinin Belirlenmesi

Radon gazı, 'Sealed Can Tekniği' (Şekil 2) ve katı-hal nükleer iz detektörü (CR-39 (allil diglikol karbonat)) kullanılarak; pasif olarak belirlendi. Yaklaşık bir ay (30 gün) bekletilen bitki örnekleri,

sürekli denge sağlandıktan sonra, 1cmx1cm kesilmiş ve önceden kodlanmış CR-39 detektörleri kavanozlara yerleştirilmiştir [15].

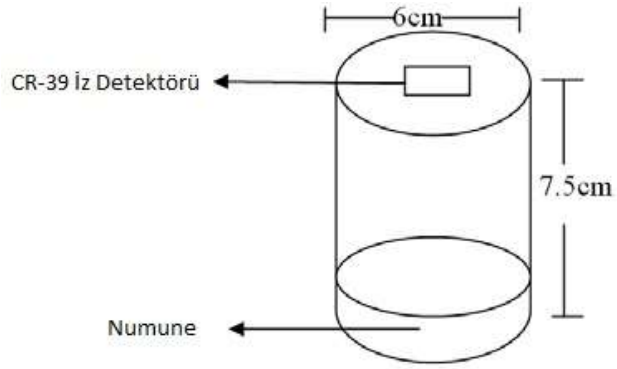

Şekil 2. Kapalı kutu tekniği (Sealed Can Technique)

Detektörler, 30 gün sonunda çıkarılarak ve Radosys cihazının (Şekil 3) kazıma ünitesinde 90 ^{0}C sıcaklıkta 4,5 saat süreyle %25'lik NaOH çözeltisi içerisinde kazındıktan sonra, yaklaşık 20 dakika nötralizasyon işlemine tabi tutuldu.

Şekil 3. RADOSYS radon ölçüm sistemi

Bu işlemden sonra, CR-39 detektörlerine saf su ile banyo işlemi yaptırıldı ve yaklaşık 12 saat dışarıda bekletilerek kurumaları sağlandı. Kuruyan detektörler sistemin mikroskop ünitesinde, her bir algılayıcı üzerinde farklı 9 bölge otomatik olarak seçilerek Radon gazından dolayı alfa parçacıklarının bırakmış olduğu izler (Şekil 4) sayılmıştır [16].

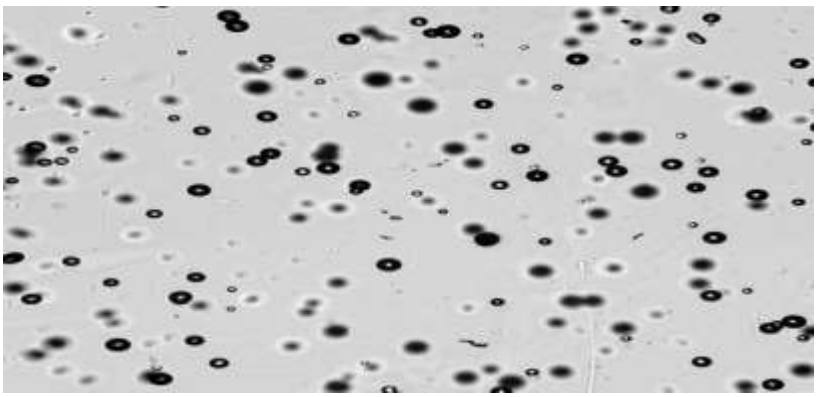

Şekil 4. CR-39 katı hal iz detektörü ve alfa parçacıklarının izleri.

Bitki örneklerinin radon konsantrasyonu aşağıdaki denklem kullanılarak hesaplanmıştır;

$$R(Bq/m^3) = \frac{D\ x\ KF\ x\ 1000}{T} \quad (1)$$

Burada; R, (Bq/m^3) birimi cinsinden Radon konsantrasyonu, D, İz yoğunluğu (iz/mm^2), KF, CR-39 detektörünün kalibrasyon faktörü 44,47 (kBqh/m^3)/(iz/saat) ve T algılayıcının Radona maruz kaldığı süredir (gün) [14-16].

2.4. İstatistiksel Analiz Metodu

Tek yönlü ANOVA, iki veya daha fazla bağımsız grup arasında istatistiksel olarak anlamlı bir fark olup olmadığını analiz etmek için kullanılır. Tek yönlü ANOVA, ilgilendiğimiz gruplar arasındaki ilişkileri karşılaştırır ve ayrıca bu ilişkilerden herhangi birinin diğerlerinden istatistiksel olarak anlamlı farklılık gösterip göstermediğini belirler. Bunun için ilk önce sıfır hipotezi (H_0) uygulandı;

$$H_0: \mu_1 = \mu_2 = \ldots = \mu_k \quad (2)$$

Burada, μ; grup ortalaması ve k; grup numarasıdır [17].

3. Bulgular ve Tartışma

3.1. Radon Konsantrasyon Seviyelerinin Belirlenmesi

Bu çalışmada Bitlis ili ve ilçelerinden alınan olan 25 adet tıbbi ve aromatik bitkinin Radon konsantrasyonları belirlenmiştir ve bu veriler Tablo 1.'de verilmiştir. Şifalı bitki örneklerinin, ^{222}Rn radyo-çekirdek aktivite konsantrasyonun; 255,70 ± 14,63 Bq/m^3 (BR13) ile 997,67 ± 28,90 Bq/m^3 (BR15) arasında değiştiği görülür.

Tablo 1. Bazı tıbbi ve aromatik bitki örneklerinin ^{222}Rn radyo-çekirdek aktivite konsantrasyonları

Numune No	^{222}Rn (Bq/m^3)	Numune No	^{222}Rn (Bq/m^3)
BR01	686,97 ± 23,98	BR14	372,79 ± 17,66
BR02	541,26 ± 21,28	BR15	997,67 ± 28,90
BR03	571,13 ± 21,86	BR16	578,30 ± 22,00
BR04	498,25 ± 20,42	BR17	357,26 ± 17,29
BR05	532,90 ± 21,12	BR18	390,71 ± 18,08
BR06	554,41 ± 21,54	BR19	320,22 ± 16,37
BR07	493,47 ± 20,32	BR20	695,39 ± 24,12
BR08	286,76 ± 15,49	BR21	833,99 ± 26,41
BR09	860,28 ± 26,83	BR22	446,87 ± 19,34
BR10	400,07 ± 20,04	BR23	544,85 ± 21,35
BR11	590,25 ± 22,22	BR24	330,97 ± 16,61
BR12	293,93 ± 21,14	BR25	525,73 ± 20,10
BR13	255,70 ± 14,63		

Tablo 1 ve Şekil 5 incelendiğinde; en yüksek radon konsantrasyon değerine (997,67 ± 28,90 Bq/m^3) Bitlis Merkez lokasyonundan toplanan BR15 numaralı *Achillea biebersteinii Afan* türü bitki örneğinin sahip olduğu, en düşük radon konsantrasyon değerine (255,70 ± 14,63 Bq/m^3) ise Bitlis'in Mutki ilçesinden toplanan *Polygonum cognatum* türü bitki örneğinin sahip olduğu görülmektedir.

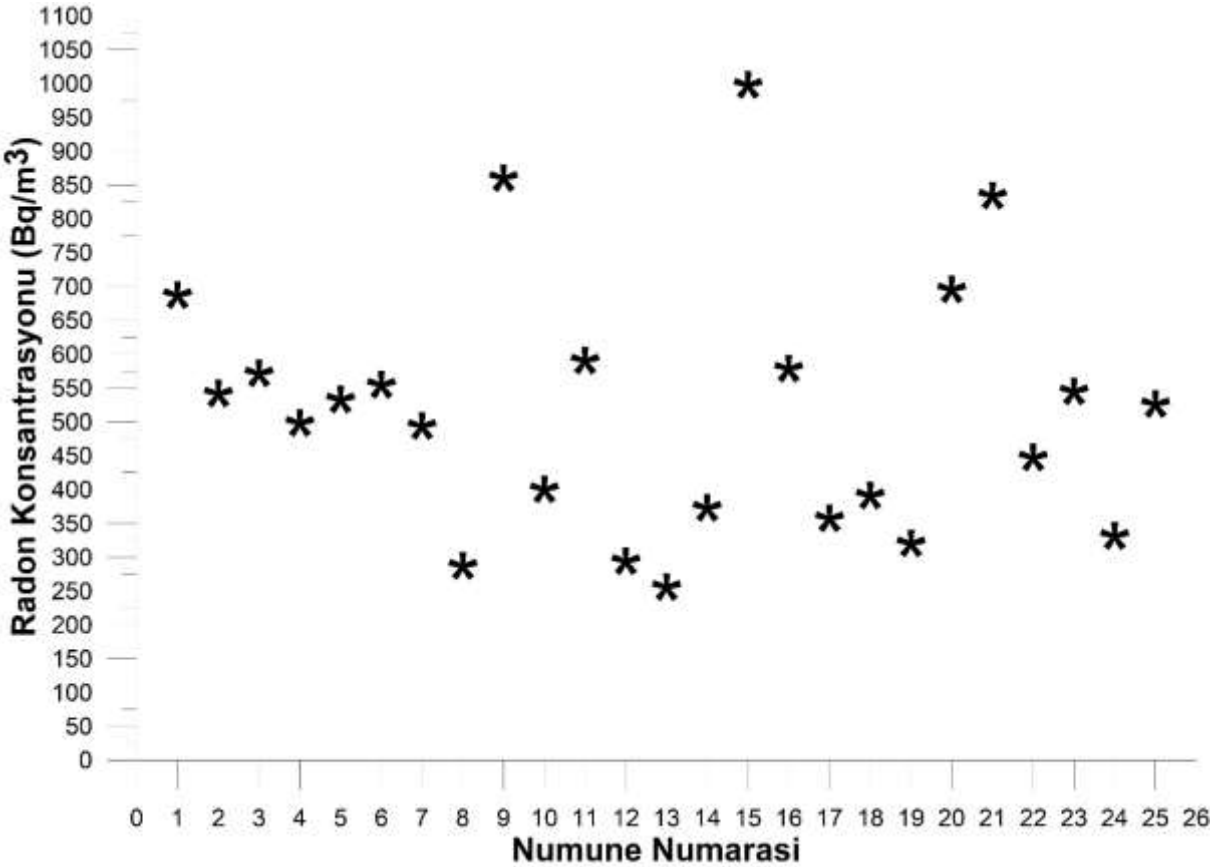

Şekil 5. Bazı tıbbi ve aromatik bitki örneklerinin ^{226}Rn radyo-çekirdeklerinin aktivite konsantrasyonları

Bu çalışmada; BR10 (Mutki) ve BR19 (Tatvan) bitki örnekleri *Salvia* sp. türü bitki örnekleri, BR11 (Mutki) ve BR15 (Bitlis Merkez) bitki örnekleri *Achillea biebersteinii Afan* türünde bitki örnekleri, BR14 (Bitlis, Kampos dağı) ve BR24 (Tatvan) bitki örnekleri ise *Thymus kotschyanus* türünde bitki örnekleridir**.** Bu bitkilerin her bir türün kendi içerisinde de radon konsantrasyon değerlerinin farklı olduğu görülmektedir. Bu durum; bitki örneklerindeki radon konsantrasyon değerlerinin; bölgenin jeolojik oluşumuna, bitkinin yetiştiği ortamın atmosferik faktörlerine, bitkinin beslendiği toprak ve suda mevcut olan radon konsantrasyon seviyelerine vb birçok etkene bağlı olabileceğini göstermektedir.

3.2. Radon Konsantrasyon Seviyelerinin İstatistiksel Olarak Analizi

Bu çalışmada, ek olarak, bitki örneklerinin radon konsantrasyon değerleri ile bitkilerin toplandığı bölgenin birbiri ile ilişkili olup olmadığı istatistiksel olarak incelendi. Bunun için öncelikle sıfır hipotezi oluşturuldu. Sıfır hipotezi; 'bitkinin toplandığı yer ile radon konsantrasyonlarının değerleri arasında fark yoktur' şeklinde kuruldu. Bu hipotezi test etmek için, öncelikle; normallik testi uygulandı (Tablo 2) ve bu sonuca bağlı olarak Tek Yönlü Varyans Analizi (one way ANOVA) yapıldı.

Tablo 2. Radon konsantrasyon değerlerinin normallik testi

		Shapiro-Wilk		
	Lokasyon	İstatistik	df	Sig. (p)
Radon	Bitlis	0,919	11	0,313
	Tatvan	0,922	8	0,447
	Mutki	0,910	4	0,482
	Güroymak			

Numune sayısı, 50'den az olduğu için normallik testinde Shapiro-Wilk testi sonuçları dikkate alındı. Buna göre, p değerleri 0,05 değerinden büyük olduğu için normal dağılıma uymaktadır. Tablo 2 incelendiğinde Güroymak lokasyonuna ait istatistiksel veriler olmadığı görülmektedir. Bunun nedeni ise; Güroymakta toplanan bitki örneği sayısının 2 olmasıdır. Analiz için kullanılan SPSS programı 2

değer için hesaplama yapmamıştır. Radon konsantrasyon değerlerinin normal dağılıma uyması sebebiyle; sıfır hipotezini test etmek için ANOVA yapılabilmektedir.

Tablo 3. Radon konsantrasyon değerlerinin Tek Yönlü Varyans Analizi

	Lokasyon	N	Ortalama	Standart sapma	Minimum	Maksimum	Sig. (p)
Radon	Bitlis	11	$5{,}814.10^2$	202,971	286,760	997,670	0,351
	Tatvan	8	$5{,}11110^2$	180,109	320,220	833,990	
	Mutki	4	$3{,}85010^2$	149,852	255,700	590,250	
	Güroymak	2	$4{,}67810^2$	156,299	357,260	578,300	
	Toplam	25	$5{,}18410^2$	188,339	255,700	997,670	

Tablo 3'de p değeri 0,351 olarak bulundu. Bu değer 0,05 değerinden büyük bir değer olduğu için; sıfır hipotezi kabul edilmiş oldu. Böylece, Tek Yönlü Varyans Analizi (ANOVA)'ya göre; lokasyonlar ile radon konsantrasyon değerleri arasında istatistiksel farkların olmadığı bulundu.

4. Sonuç ve Öneriler

Bu çalışmada, Bitlis'te yetişen 25 tıbbi ve aromatik bitki örneklerinin ^{222}Rn radyo-çekirdek aktivite konsantrasyonları belirlenmiştir. Bu çalışmada elde edilen sonuçlar aşağıda maddeler halinde verilmiştir.

(i) Farklı lokasyonlarda toplanan bitki örneklerinin radon konsantrasyon değerlerinin, farklı seviyelerde olduğu görülmüştür.

(ii) Farklı lokasyonlarda toplanan aynı tür bitki örneklerinin radon konsantrasyon değerlerinin; lokasyona bağlı olarak değiştiği görülmüştür.

(iii) ^{222}Rn radyo-çekirdek aktivite konsantrasyon değerlerinin; bu çalışmadaki verilere göre, istatistiksel olarak lokasyona bağlı olarak değişmediği görülmüştür. Ancak, literatüre göre, radonun geldiği ailelere bağlı olarak; ana radyo-çekirdeğin aktivite değerinin lokasyon, jeolojik yapı, atmosferik etkiler vb. faktörlere göre değiştiği görülmüştür [18-22].

(iv) Bu çalışmada, daha fazla radon konsantrasyon değerinin (N= 25'den daha fazla) istatistiksel olarak analizi yapılsaydı; literatüre uygun daha farklı bir sonuç bulunabilirdi.

Kaynaklar

[1] UNSCEAR. 1988. Sources and effects of ionising radiation. United Nations Scientific Committee on the Effects of Atomic Radiation. Annex A, United Nations, New York.

[2] Elzain A.E.A. 2015. Estimation of Soil Gas Radon Concentration and the Effective Dose Rate by Using SSNTDs. International Journal of Scientific and Research Publications, 5 (2): 1-5.

[3] UNSCEAR. 2000. Sources and effects of ionising radiation. United Nations Scientific Committee on the Effects of Atomic Radiation. United Nations, New York.

[4] Arafa W. 2004. Specific Activity and Hazards of Granite Samples Collected from The Eastern Desert of Egypt.. J. Environ. Radioact., 75: 315–327.

[5] Rahman S.U., Rafique M., Matiullah A.J. 2010. Radon Measurement Studies in Workplace Buildings of The Rawalpindi Region and Islamabad Capital Area, Pakistan. Build. Environ., 45: 421–426.

[6] Agarwal T.K., Sahoo B.K., Gaware J.J., Joshi M., Sapra B.K. 2014. CFD Based Simulation of Thoron (220Rn) Concentration in a Delay Chamber for Mitigation Application. J. Environ. Radioact, 136: 16–21.

[7] Ghany H.A.A., Aassy I.E.E., Ibrahim E.M., Gamil S.H. 2018. White Sand Potentially Suppresses Radon Emission from Uranium Tailings. Radiat. Phys. Chem., 144: 100–105.

[8] Dieguez-Elizondo P.M., O´Donuhoe P.G., Gil-Lopez T., Castejon-Navas J., Gálvez-Huerta M.A. 2019. Calculation Methods of Radon-222 Radiological Activity for NORM Plant with Ventilation. Journal of Petroleum Science and Engineering, 183 (106360): 1-9.

[9] Little J.B. 1997. What Are The Risks of Low-Level Exposure to a Radiation from Radon? P. Natl. Aca. Sci. USA, 94: 5996–5997.

[10] ICRP., 2008. Nuclear decay data for dosimetric calculations. Ann. ICRP, 38: 7–96.
[11] Li P., Zhang R., Zheng G. 2018. Genetic and Physiological Effects of the Natural Radioactive Gas Radon on the Epiphytic Plant Tillandsia Brachycaulos. Plant Physiology and Biochemistry, 132: 385-390.
[12] Kılıç Ö. 2015. Bitlis Kaynak Sularında Radon Seviyesinin Belirlenmesi. Bitlis Eren Üniversitesi, Fen Bilimleri Enstitüsü, Ders Semineri, Bitlis.
[13] http://www.mta.gov.tr/v2.0/bolgeler/van/index.php?id=bitlis (Erişim tarihi: 30.03.2015).
[14] Kılıç Ö. 2016. Bitlis'te Yetişen Bazı Tıbbi ve Aromatik Bitkilerde Radon Seviyesinin Belirlenmesi. Bitlis Eren Üniversitesi, Fen Bilimleri Enstitüsü, Yüksek Lisans Tezi, 46s, Bitlis.
[15] Şahin Bal S., Kılıç Ö., Gönültaş F. 2017. Bitlis Kaynak Sularında Radon Konsantrasyonunun Belirlenmesi. Sakarya Üniversitesi Fen Bilimleri Enstitüsü Dergisi, 21 (3): 302-306.
[16] Radosys. 2011. Radosys Kullanma Kılavuzu, Hungary: Radosys.
[17] Erol H. 2010. SPSS Paket Programı ile İstatistiksel Data Analizi. Nobel kitapevi, Adana.
[18] Sussa F.V., Damatto S.R., Alencar M.M., Mazzilli B.P., Silva P.S.C. 2013. Natural Radioactivity Determination in Samples of Peperomia Pellucida Commonly Used as a Medicinal Herb. Journal of Environmental Radioactivity, 116: 148-151.
[19] Njinga R.L., Jonah S.A., Gomina M. 2015. Preliminary Investigation of Naturally Occurring Radionuclides in Some Traditional Medicinal Plants Used in Nigeria, Journalof Radiation Research and Applied Sciences, 8: 208-215.
[20] Chandrashekara K., Somashekarappa H.M. 2016. Estimation of Radionuclides Concentration and Average Annual Committed Effective Dose Due to Ingestion for Some Selected Medicinal Plants of South India. Journal of Radiation Research and Applied Sciences, 9: 68-77.
[21] Okeji M.C., Kenneth K.A., Felicitas U.I. 2012. Natural Radioactivity in Cultivated Land in the Vicinity of a Phosphate Fertilizer Plant in Nigeria. Radiation Physics and Chemistry, 81: 1823–1826.
[22] Alsaffar M.S., Jaafar M.S., Kabir N.A., Ahmad N. 2015. Distribution of ^{226}Ra, ^{232}Th and ^{40}K in Rice Plant Components and Physico-Chemical Effects of Soil on Their Transportation to Grains. Journal of Radiation Research and Applied Sciences, 8: 300-310.

Araştırma Makalesi / Research Article

Comparission of E1 Response of ^{154}Sm and ^{155}Sm in the Pygmy Dipole Resonance (PDR) Region

Hakan YAKUT, Emre TABAR, Huseynqulu QULIYEV*

Physics Department, Sakarya University, 54187 Sakarya, Turkey
(ORCID: 0000-0002-3903-5863) (ORCID: 0000-0002-5093-9409) (ORCID: 0000-0002-6306-658X)

Abstract
The dipole response associated with the pygmy dipole resonance (PDR) in ^{154}Sm and ^{155}Sm has been studied. In the ^{154}Sm nucleus 1^- phonons with K=0 and K=1 branches have been calculated using the Translation and Galilean Invariant Quasiparticle Random Phase Approximation (TGI-QRPA). The structure of the more pronounced electric dipole ($E1$) peaks in PDR region in ^{154}Sm is composed of predominantly two-quasiproton or two-quasineutron states. The calculations in ^{155}Sm has been performed in the framework of the Translation and Galilean Invariant Quasiparticle Phonon Nuclear Model (TGI-QPNM) based on the TGI-QRPA 1^- phonons calculated for ^{154}Sm. When going from ^{154}Sm to neighbouring ^{155}Sm, the fragmentation of the $E1$ strength is dramatically enhanced. The results emphasize the role of the quasiparticle⊗phonon interactions in enhancing the fragmentation of the strength in the PDR region in ^{155}Sm. Even though the strong fragmentation of the $E1$ strength obtained for ^{155}Sm, in 5-8 MeV energy region the summed $E1$ strength is comparable to that in ^{154}Sm. The results indicate that one quasiparticle behaves solely as a spectator in ^{155}Sm.

Keywords: TGI-QRPA, TGI-QPNM, PDR, ^{154}Sm,^{155}Sm, $E1$.

Pygmy Dipol Rezonans (PDR) Bölgesinde ^{154}Sm ve ^{155}Sm'nin E1 Uyarılmalarının Karşılaştırılması

Öz
^{154}Sm ve ^{155}Sm izotoplarının pygmy dipol rezonansla (PDR) ilişkisi incelenmiştir. ^{154}Sm çekirdeğinde 1^- fononlarının K=0 ve K=1 dalları Öteleme ve Galileo Değişmez Kuaziparçacık Rastgele Faz Yaklaşımı (TGI-QRPA) modeli kapsamında hesaplanmıştır. ^{154}Sm için PDR bölgesinde daha belirgin olan elektrik dipolün (El) pik yapıları, ağırlıklı olarak iki-kuaziproton veya iki-kuazinötron durumlarından meydana gelmektedir. ^{155}Sm çekirdeği üzerine yapılan hesaplamalar, ^{154}Sm için kullanılan 1^- fononlarının hesaplandığı TGI-QRPA modeli baz alınarak, Öteleme ve Galileo Değişmez Kuasiparçacık Fonon Nükleer Model (TGI-QPNM) çerçevesinde yapılmıştır. ^{154}Sm'den komşu ^{155}Sm'ye giderken, E1 kuvvetinin çarpıcı bir biçimde parçalanmaktadır. Sonuçlar, kuaziparçacık⊗fonon etkileşimlerinin ^{155}Sm' de PDR bölgesi için kuvvetin parçalanmasındaki rolünü vurgulamaktadır. ^{155}Sm için elde edilen E1 gücünün güçlü parçalanmasına rağmen, 5-8 MeV enerji bölgesinde toplanan E1 gücü, ^{154}Sm'deki ile benzelrlik göstermektedir. Sonuçlar, bir kuasiparçacığın ^{155}Sm'de yalnızca bir izleyici olarak davrandığını göstermektedir.

Anahtar kelimeler: TGI-QRPA, TGI-QPNM, PDR, ^{154}Sm,^{155}Sm, $E1$.

1. Introduction

Collective excitations (magnetic and electric dipole excitations) play an important role in the study of the nuclear structure. GDR mode defined as the vibration of the proton system against the neutron system is the first collective mode [1]. In the early 1960s, thermal neutron capture experiments showed that there were E1 excitations around the neutron threshold energy [2]. These excitations are called PDR mode because the strength of this mode are smaller than GDR [3]. PDR mode in even-even spherical,

*Sorumlu yazar: huseynqulu@yahoo.com
Geliş Tarihi: 21.11.2019, Kabul Tarihi: 19.12.2019

semi-magic and double magic nuclei were theoretically and experimentally studied. Recently, interest in PDR mode studies in deformed nuclei has increased. In this context, only theoretical studies for even-even deformed Sm and Nd nuclei are available in the literature [4]. In odd-mass nuclei only experimental study was performed for ^{139}La [5]. Therefore, the structure of PDR mode in odd mass nuclei are a open question.

The aim of the present work is to study the properties of PDR of in ^{154,155}Sm. The theoratical tool used in this paper based on selection of the suitable separable effective forces to restore the broken translational and Galilean invariances of the QPNM and QRPA hamiltonians for the description of the E1 excitations in odd- and even-mass nuclei, respectively. In our previous study, this method has been quite successful in explaining of the PDR in N=82 nuclei [6], low lying electric dipole excitations up to 4 MeV [7] and GDR mode in ^{235}U [8].

2. Theory

The model Hamiltonian that produces the E1 states in deformed nuclei can be written as follows:

$$H = H_{sqp} + h_0 + h_\Delta + W_1 \tag{1}$$

where H_{sqp} is the Hamiltonian for the single-quasiparticle motion, W_1 is the isovector part of the dipole-dipole ($\lambda = 1$) interaction, h_0 and h_Δ are separable effective residual interactions restoring the broken Translational and Galilean symmetry of the Hamiltonian, respectively.

$$H_{sqp} = \sum_{qq'} \varepsilon_s(\tau) B_{qq'}(\tau) \tag{2}$$

$$W_{dip} = \frac{3}{2\pi}\chi_1 \left(\frac{NZ}{A}\right)^2 \left(\vec{R}_N - \vec{R}_Z\right)^2, \vec{R}_\tau = \frac{1}{N_\tau}\sum_{k=1}^{N_\tau} r_k \tag{3}$$

$$h_0 = -\frac{1}{2\gamma}\sum_\mu [H_{sqp}, P_\mu]^+ [H_{sqp}, P_\mu] \tag{4}$$

$$h_\Delta = -\frac{1}{2\beta}\sum_\mu [U_{çift}, R_\mu]^+ [U_{çift}, R_\mu] \tag{5}$$

The coupling parameters $\gamma = \langle 0|[P_\mu^+, [H_{sqp}, P_\mu]|0\rangle$ and $\beta = \langle 0|[P_\mu^+, [U_\Delta, R_\mu]|0\rangle$ are determined by the mean field and pairing potentials, respectively, where $R_\mu = \sum_{k=1}^{A} r_k Y_{lm}(\Theta_k, \Phi_k)$ is proportional to the c.m. coordinate of the nucleus.

The wave function of the odd mass deformed nuclei consists of a sum of single-quasiparticle and quasiparticle phonon terms

$$\psi_K^j(\tau) = \left\{ N_K^j(\tau)\alpha_K^+(\tau) + \sum_{i\mu}\sum_\nu G_j^{i\mu\nu}\alpha_\nu^+(\tau) Q_{i\mu}^+ \right\} |\psi_0\rangle \qquad \mu = 0, \pm 1 \tag{6}$$

To obtain the η_K excitation energies of *electric dipole resonance* for odd-mass nuclei, one has to solve the secular equation following secular equation.

$$P(\eta_K) \equiv \varepsilon_\varsigma - \eta_K - \sum_{i\mu}\sum_\nu \frac{\left(\kappa_1 \frac{2}{N_\tau} r_{\varsigma_q\nu}^\tau V_{\varsigma_q\nu} \overline{L_i} - \varepsilon_{\varsigma_q\nu}^{(-)} p_{\varsigma_q\nu}^\tau M_{\varsigma_q\nu} + \Delta_\tau r_{\varsigma_q\nu} L_{\varsigma_q\nu} L_i\right)^2}{4\omega_i Y(\omega_i)\left(w_i + \varepsilon_\nu - \eta_K\right)} = 0 \tag{7}$$

Where

$$L_i = \frac{\gamma}{\beta}\frac{\sum_\tau \Delta_\tau \sum_{qq'} r_{qq'} M_{qq'} w^i_{qq'}}{\sum_\tau \sum_{qq'} \varepsilon_{qq'} p_{qq'} L_{qq'} g^i_{qq'}} \qquad \overline{L_i} = \gamma \frac{\sum_\tau \frac{1}{N_\tau} \sum_{qq'} r_{qq'} u_{qq'} g^i_{qq'}}{\sum_\tau \sum_{qq'} \varepsilon_{qq'} p_{qq'} L_{qq'} g^i_{qq'}} \tag{8}$$

Here, $p^\mu_{qq'} = \langle q | p_\mu | q' \rangle$ and $r^\mu_{qq'} = \langle q | r_\mu | q' \rangle$ are the single particle matrix elements of the linear momentum and core mass center position operator, respectively. The Bogolyubov canonical transformation parameters (u_q and v_q) are also expressed in $V_{qq'} = u_q u_{q'} - v_q v_{q'}$, $U_{qq'} = u_q v_{q'} + u_{q'} v_q$, $L_{qq'} = u_q v_{q'} - u_{q'} v_q$ and $M_{qq'} = u_q u_{q'} - v_{q'} v_q$,respectively. $\psi^i_{qq'}$ and $\varphi^i_{qq'}$ terms are two quasiparticle amplitudes of the even-even core and given in the $g^i_{qq'} = \psi^i_{qq'} + \varphi^i_{qq'}$ and $w^i_{qq'} = \psi^i_{qq'} - \varphi^i_{qq'}$. Finally, the $Y(\omega_i)$ term is obtained from the normalization condition of the wave function of the core nucleus. $\varepsilon_{qq',\tau} = \varepsilon_q + \varepsilon_{q'}$ and $\varepsilon^-_{qq',\tau} = \varepsilon_q - \varepsilon_{q'}$ are terms are two quasiparticle energies.

$$\left(N^j_K\right)^{-2} = 1 + \sum_{i\mu}\sum_{\nu}\left(\frac{-4\kappa_1 \frac{1}{Z} r^p_{\varsigma_q\nu} V_{\varsigma_q\nu} \overline{L_i} - 2\varepsilon^{(-)}_{\varsigma_q\nu} p^p_{\varsigma_q\nu} M_{\varsigma_q\nu} + 2\Delta_n r^p_{\varsigma_q\nu} L_{\varsigma_q\nu} L_i}{4\omega_i Y(\omega_i)\left(\omega_i + \varepsilon_\nu - \eta_K\right)} \right)^2 \tag{9}$$

$$G^{i\mu\nu}_j = -N^j_\varsigma \left\{ \frac{-4\kappa_1 \frac{1}{N} r^p_{\varsigma_q\nu} V_{\varsigma_q\nu} \overline{L_i} - 2\varepsilon^{(-)}_{\varsigma_q\nu} p^p_{\varsigma_q\nu} M_{\varsigma_q\nu} + 2\Delta_n r^p_{\varsigma_q\nu} L_{\varsigma_q\nu} L_i}{\sqrt{4\omega_i Y(\omega_i)}\left(\omega_i + \varepsilon_\nu - \eta_K\right)} \right\} \tag{10}$$

Probabilities of *E*1 transitions from the ground-states to the excited-states in odd-mass and even-even deformed nuclei, respectively can be written as follows:

$$B(E1, I_i K_i \to I_f K_f) = \sum_\mu \langle I_i 1 K_i \mu | I_f K_f \rangle^2 \left| -\frac{1}{2} e^n_{eff.} \sum_q N^j_{\varsigma_q} N^j_{\varsigma_0} r^\tau_{\varsigma_q\varsigma_0} V_{\varsigma_q\varsigma_0} + N^j_{\varsigma_0} \sum_{i\mu} G^{i\mu\varsigma_0}_j \frac{\kappa_1 (1 - L_i)}{\sqrt{\omega_i Y(\omega_i)}} \left(e^n_{eff.} \frac{F_n}{N} - e^n_{eff.} \frac{F_p}{Z} \right) \right|^2 \tag{11}$$

where $e^p_{eff} = N/A$ and $e^n_{eff} = -Z/A$ are neutron and proton effective charges, respectively.

The QRPA theory for even-even nuceus was in ref [7].

3. Results and Discussions

For calculation of the E1 dipole transitions in the ^{155}Sm the mean field deformation parameters δ_2 are calculated according to [9] using deformation parameters β_2 defined from experimental quadrupole moments [10]. The single-particle energies were obtained from the Warsaw deformed Woods–Saxon potential [11]. The pairing-interaction constants taken from Soloviev [12] are based on the single-particle levels corresponding to the nucleus studied. The calculation for the E1 excitation was performed using a strength parameter $\chi_1 = 350 / A^{5/3} MeVfm^{-2}$, values of the pairing parameters Δ and λ are given in Table 1.

Table 1. Pairing correlation parameters (in MeV) and δ_2 values

Nucleus	$[Nn_z\Lambda]\Sigma$	Δ_n	Δ_p	λ_n	λ_p	δ_2
^{155}Sm	[521] 3/2$^-$	1.11	1.22	-6.702	-8.569	0.234

The distribution of B(E1) strength calculated for ^{154}Sm and ^{155}Sm are shown in Fig.1. Theory predicts three strong E1 transitions at 6.348 MeV, 6.916 MeV and 7.779 MeV energies for K=0 branches and four strong E1 transitions at 6.645 MeV, 6.919 MeV, 7.167 MeV and 7.6 MeV energies for K=1 branches in ^{154}sm core nucleus. Similar situations are seen in the $K_f=K_0$ and $K_f=K_0\pm1$ branches of the ^{155}Sm nucleus.

The gross features of the E1 strength in 5-8 MeV energy range in ^{154,155}Sm are given in Table 2. For ^{154}Sm theory predicts nineteen negative-parity K=0 states with $\Sigma B(E1)=0.387$ e^2fm^2 and thirty K=1 states with $\Sigma B(E1)=0.193$ e^2fm^2. K=0 branch ^{154}Sm corresponds to $K_f=K_0$ in odd mass ^{155}Sm, K1 branch of core ^{154}Sm nucleus corresponds to $K_f=K_0-1$ and $K_f=K_0+1$ states of odd mass ^{155}Sm. In addition, because of the Clebsh-Gordon coefficients in the B(E1) transition expression, $K_f=K_0$ branch has two $\{(K_0-1,I_0-1),(K_0-1,I_0)\}$ branches, $K_f=K_0-1$ branch has three $\{(K_0-1,I_0-1),(K_0-1,I_0),(K_0-1,I_0+1)\}$ branches and $K_f=K_0+1$ branch has one $\{K_0+1,I_0+1\}$ branch. For ^{155}Sm nucleus, thirty six $K_f=K_0$ ($3/2^+$) branch with $\Sigma B(E1)=0.376$ e^2fm^2, nine $K_f=K_0-1$ ($1/2^+$) branch with summed $\Sigma B(E1)=0.017$ e^2fm^2 and thirty five $K_f=K_0+1$ ($5/2^+$) branch with summed $\Sigma B(E1)=0.017$ e^2fm^2 were calculated. It is seen from Table 2 that K = 0 (or $K_f=K_0$ for odd mass nucleus) branch is the dominant branch in PDR region from the results of both core ^{154}Sm and odd mass^{155}Sm nuclei.

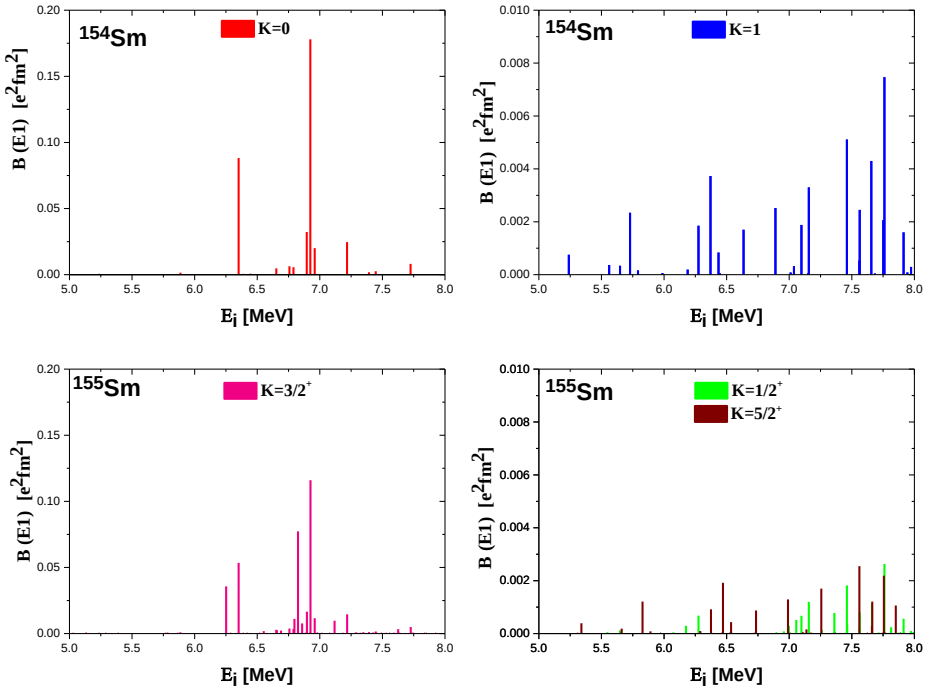

Figure 1. Comparison of the B(E1) values calculated for ^{154}Sm and ^{155}Sm nucleus.

Table 2. The comparison of theoretical values of summed *E*1 strength for ^{154,155}Sm nuclei in the energy range of 5-8 MeV.

^{154}Sm	$\Sigma B(E1)$ (e^2fm^2)	^{155}Sm	$\Sigma B(E1)$ (e^2fm^2)
$K=1^-_0$	0.376	$K=3/2^+$	0.387
$K=1^-_1$	0.046	$K=1/2^+$	0.017
		$K=5/2^+$	0.017
K=All	0.422	K=All	0.421

Excitations energies, B(E1) transitions, one-quasiparticle and Quasiparticle⊗Phonon amplitudes for odd mass ^{155}Sm nucleus have been shown in Table 3. The E1 states in the PDR region in^{155}Sm nucleus have approximately 99% Quasiparticle⊗Phonon character. In ^{155}Sm for instance, the strongest transitions are dominated by the $[521]\uparrow\otimes Q_j$.

Table 3. Energies, B(E1↑)values, amplitudes, and the structure of PDR in odd-mass ^{155}Sm isotope.

E_i (MeV)	B(E1) (e^2fm^2)	K^π	N_K	$\sum_{i\mu}\sum_{\nu} G_j^{i\mu\nu}$	Sturcture
6.348	0.0078	$3/2^+$	0.0912	-0.9946	% 100 $[521]\uparrow\otimes Q_{13}$
6.896	0.030	$3/2^+$	0.0295	-0.9948	% 99 $[521]\uparrow\otimes Q_{18}$
6.917	0.153	$3/2^+$	0.104	-0.2919	% 8.5 $[521]\uparrow\otimes Q_{18}$
				-0.9414	% 89 $[521]\uparrow\otimes Q_{19}$
				0.1223	% 1.5 $[521]\uparrow\otimes Q_{20}$
6.956	0.025	$3/2^+$	0.00943	0.9997	% 99 $[521]\uparrow\otimes Q_{20}$
7.167	0.016	$1/2^+$	0.0278	0.9995	% 99 $[521]\uparrow\otimes Q_{38}$
7.215	0.026	$3/2^+$	0.124	-0.9892	% 97.8 $[521]\uparrow\otimes Q_{21}$
7.664	11.7713	$1/2^+$	0.00915	0.9995	% 99 $[521]\uparrow\otimes Q_{48}$
7.780	69.5644	$3/2^+$	0.0565	0.9878	% 98 $[521]\uparrow\otimes Q_{28}$
				-0.1225	% 2 $[521]\uparrow\otimes Q_{28}$
7.786	21.4048	$3/2^+$	0.925	-0.1009	% 1 $[521]\uparrow\otimes Q_{27}$
				0.7079	% 50 $[521]\uparrow\otimes Q_{28}$
				0.6899	% 48 $[521]\uparrow\otimes Q_{29}$

4. Conclusion

In this study, E1 transitions were theoretically calculated for ^{154,155}Sm isotopes in the frame of QRPA and QPNM, respectively.The calculations show existance of the resonance like structure between 6.2-8 MeV energy intervals, which can be identified as pygmy dipole resonance. When the total B(E1) transition values of the core and odd mass have been compared, it has been seen that the total transition is close to each other in PDR region. However, due to the coupling properties of the E1 operator, E1 spectra of ^{155}Sm are much more fragmented than the core's. The calculations show that the effect of the one quasiparicle component in the wave function on the structure of the E1 levels in ^{155}Sm is very weak, and the contribution of the Quasiparticle⊗Phonon components are dominant.

Acknowledgments

We are grateful to Prof. Dr. A. A. Kuliev for their valuable comments. This research was supported by the Scientific and Technological Research Council of Turkey (TUBITAK) (Project No.118F094).

Referances

[1] Goldhaber M., Teller E. 1948. On nuclear dipole vibrations. Physical Review, 74: 1046.
[2] Bartholomew G.A. 1961. Annu. Rev. Nucl. Sci. 11: 259.
[3] Brzosko J.S., Gierlik E., Soltan A., Wilhelmi Z., Can. J. 1969. Phys., 47: 2849.
[4] Yoshida K., Nakatsukasa T. 2011. Phys. Rev., C 83: 021304®.
[5] Makinaga A., et.al. 2010. Phys. Rev., C:82, 024314.
[6] Guliyev E., Kuliev A.A., Guner M. 2010. Cent. Eur. J. Phys., 8: 961.
[7] Kuliev A.A, et al. 2010. Eur. Phys. J. A 43: 313.
[8] Yakut H., et.al. 2019. 5th International Conference on Theoretical and Experimental Studies in Nuclear Applications and Technology, Conferance Proceeding Book, 167.
[9] Bohr A., Mottelson B. 1975. Nuclear Structure (Benjamin, Reading, 1975), Vol. II.
[10] Raman S., et al. 2001. At. Data Nucl. Data Tables, 78: 1.
[11] Dudek J., Werner T. 1978. J. Phys. G 4: 1543.
[12] Soloviev G. 1976.Theory of Complex Nuclei: TerHaar D (ed). Pergamon Press. 1st edn. New York.

Araştırma Makalesi / Research Article

Energy loss analysis from RBS spectrum of thin Cu_2ZnSnS_4 (CZTS) film

Metin USTA*

Mustafa Kemal University, Science and Art Faculty, Physics Department, Hatay
(ORCID: 0000-0002-7896-397X)

Abstract
The goal of this work is to offer an alternative method to the available literature on determining the energy loss of CZTS thin films. For this purpose, thin CZTS film structures were first produced by sol-gel method and then the RBS spectrum was received with RBS detector irradiating this structure with 3.034 MeV proton beams in a microbeam chamber. The energy calibration was implemented to this spectrum, where the it was fitted with SIMNRA program. In the RBS spectrum of the thin film generated, a method for the calculation of energy loss was used for the position and energy width analysis of the corresponding peaks and a polynomial fit was obtained from the stopping power of the CZTS thin film by making certain approaches. Also, the effective charge approach that we used in our previous studies for the stopping power was employed with atomic natural orbitals and it was founded that the results were close to each other at certain error rates. The data obtained from this study will inspire the future studies on the interaction of radiation with matter.

Keywords: Energy loss, CZTS, RBS.

İnce Cu_2ZnSnS_4 (CZTS) filmin RBS spektrumundan enerji kaybı analizi

Öz
Bu çalışmanın amacı, CZTS ince filmlerinin enerji kaybını belirlemek için mevcut literatüre alternatif bir yöntem sunmaktır. Bu amaçla, ince CZTS film yapıları ilkönce sol-gel yöntemiyle üretildi ve daha sonra bu yapı bir mikroışın çemberinde 3.034 MeV protonlarla ışınlanarak RBS detektörüyle RBS spektrumu alındı. SIMNRA programıyla fit edilen bu spektruma enerji kalibrasyonu uygulandı. Üretilen ince filmlerin RBS spektrumunda, ilgili piklerin konum ve enerji genişliği analizinden enerji kaybı hesaplaması için bir yöntem kullanıldı ve belirli yaklaşımlar yaparak CZTS ince filmin durdurma gücünden bir polinom fit elde edildi. Ayrıca, durdurma gücü için önceki çalışmalarda kullandığımız etkin yük yaklaşımı atomik doğal orbitaller ile kullanıldı ve sonuçların belirli hata oranlarında birbirine yakın oldukları bulundu. Bu çalışmadan elde edilen veriler maddeyle radyasyonun etkileşmesi üzerine yapılacak çalışmalara ilham verecektir.

Anahtar kelimeler: Enerji kaybı, CZTS, RBS.

1. Introduction

As well as cosmic rays, slow and fast particles penetrate into the interior and the exterior. Significant representatives of our outer solar system are solar rays consisting of solar wind, proton, electron and helium ions. These particles interact with the planets' atmosphere. Sunburn is probably the best-known radiation effect that these particles cause. Analyzes of meteors and moon samples offer evidence of exposure of materials to high radiation doses and consent modeling of solar wind and intergalactic radiation. The exposure of spacecraft to local radiation fields upsets the material properties of the spacecraft, the functioning of computerized instruments, and the health of astronauts. Particularly the interaction of radiation with spacecraft and solar batteries placed on satellite wings changes the function and energy efficiency of these materials. Therefore, it is very important to examine the interaction of charged particles with solar batteries and therefore to determine the energy loss [1].

*Sorumlu yazar: musta@mku.edu.tr
Geliş Tarihi: 28.10.2019, Kabul Tarihi: 21.12.2019

The development of clean energy resources as an alternative to fossil fuels has become one of the most important requirements of the 21st Century. Among the renewable energy sources, the best alternative to meet the energy needs of modern society is solar energy. In order to make photovoltaic devices widespread, cheap, high efficiency and environmentally friendly solar cells are needed. In particular, the Cu_2ZnSnS_4 (CZTS) compound is a good candidate for the absorbent layer in solar cell applications [2, 3].

Despite being a film with great potential as absorbent material, studies on CZTS solar cells are still in its infancy. The examination of the interaction of CZTS solar cells with radiation, or rather the determination of the stopping power for charged particles, has a great proposition in terms of efficiency. To the best of our knowledge, there is no scientific study of the energy loss of CZTS thin films. In the light of the information thus far, it is necessary to study the theoretical and experimental stopping power of CZTS films. The aim of this work is to present an alternative method to available works on determining the energy loss of CZTS thin films. Therefore, thin CZTS film structures were first produced by sol-gel method and then the RBS spectrum was obtained by irradiating this structure with proton beams in microbeam chamber. The RBS spectrum was taken with RBS detector and the energy calibration was then applied to this spectrum, where the RBS spectrum was fitted with SIMNRA [4] program. Then, in the RBS spectrum of the CZTS thin film, the individual peaks of each element constituent the film were generated. These peaks produced were matched to Gaussian type function by chi2 method. The values obtained by the peak analysis were used instead of the energy loss statements derived from the linear approach and the stopping power data of these elements were calculated by iterations. At least squares method was applied to these obtained values and the stopping power of CZTS thin film was determined by Bragg additivity rule. The results were compared with the theoretical effective charge approach presented in this study and the available reference data in the literature. This technique is a fast and simple method that can be used analytically to help improve the accuracy of the existing methods in the literature used to determine the energy loss of thin films.

2. Material and Method

2.1. Experimental procedure

2.1.1. Production of CZTS thin films

The CZTS films were produced by using sol-gel spin coating method. The CZTS precursor solutions were arranged by melting copper (II) acetate monohydrate (0.3M, 98+%), zinc (II) acetate dihydrate (0.3M, 99.99%), tin (II) cloride (0.3M, 98%) from Sigma Aldrich and thiourea (1.2M, 99.0+% from Sigma Aldrich) into 2-methoxyethanol (20 ml, 99.8% from Sigma Aldrich). The last solutions were commingled at 45^{o}C, 850 rpm for 1 h to liquefy the metal compounds entirely. Throughout mixing, 2 ml of diethanolamine (DEA) was put stepwise inside each solution as a stabilizer. The quartz-glass slides were use as substrates which were ultrasonically wiped out one by one with detergent, nitric acid (1:4), acetone and ethanol for 10 min. To fabricate the CZTS films, the already made solutions were spin-coated onto quartz and n-type silicon substrates at 3000 rpm for 30 s in the course of solvent-drying at 175^{o}C for 10 min on a hot plate. To provide electrical conductivity, molybdenum layer was sandwiched between quartz-glass substrate and CZTS thin film layer. Lastly, the samples were subjugated to an annealing procedure for 2 h at 500^{o}C in a quartz tube including 10 g of elemental sulfur. The thickness of the produced films was determined from the SEM cross section images. The completed sample is shown in Figure 1 below.

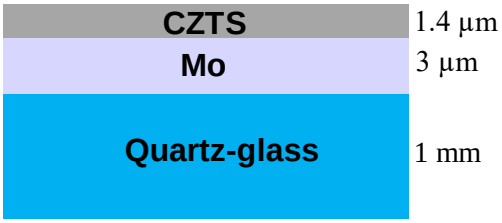

Figure 1. Fabricated CZTS thin film and its thickness

2.1.2. Set up and detection procedure

The experimental set up and procedure were carried out at the Jožef Stefan Institute Tandetron accelerator facility. Test measurements were made for both CZTS samples and NIST 1107 naval brass sample for energy calibration using protons of 3.034 MeV. Since the NIST 1107 naval brass contains most of the elements in the produced CZTS film, it was used [5] as reference material. For convenience, the microbeam chamber was employed with the RBS detector at 135 degrees scattering angle. The solid angle of the RBS detector is 4.59e-3, the resolution is 18 keV, the diameter of the detector aperture with circular shape is 4 mm, the sample-detector aperture is 52.3 mm, and the thickness of the aluminum foil material in front of the detector is 800 nm. RBS signal from the chopper and RBS spectrum was obtained. The incoming proton beam had a diameter of 30 micrometers but was scanned over an area of 500x500 micrometers. To get the number of input particles, the chopper signal was considered and the calibration constant was found from the measurements of NIST 1107. Experimental set up is displayed in Figure 2.

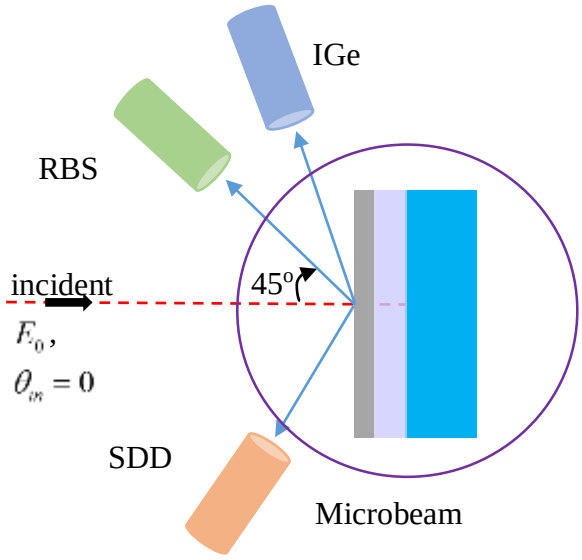

Figure 2. Experimental set up

2.1.3. Determination of energy loss

The RBS spectrum shown in Figure 3 was simulated by means of SIMNRA. Previous calibration values and necessary initial parameters were entered into the program and the spectrum was obtained. The target material consists of three different layers. Cu, Zn, Sn and S elements containing CZTS thin film as the first layer, Mo element as the second layer and O and Si elements with the inclusion of the quartz substrate as the last layer were selected and the conjectural concentration values of these elements were inserted into this program. The roughness for the layer and the substrate materials and the correction factors for stopping power of these layers were not considered. Instead, the Chi2 channel evaluation option was used as the fit parameter for the roughness of each layer, and the fit values were obtained with a maximum iteration of 50 and an accuracy of 0.01. As reaction kinematics, Rutherford cross-sections were employed for backscattering of projectiles present in the program's internal file.

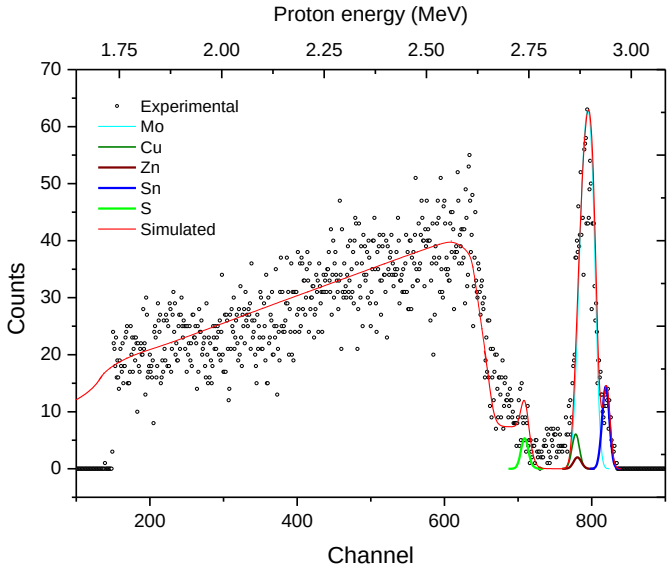

Figure 3. The RBS spectrum of the CZTS thin film

Backscattering technique is one of the methods used to determine the energy loss, the ingredients with the depth scale and the stopping cross section of the samples can be assigned from the RBS analysis. However, due to the peak of the Mo layer used to provide conductivity between the substrate and film, the peaks of elements constituting the CZTS thin film in the RBS spectrum of Figure 3 are not clearly visible. Hence, the RBS spectrum of the film was simulated with SIMNRA and the peaks of the elements forming the sample were generated.

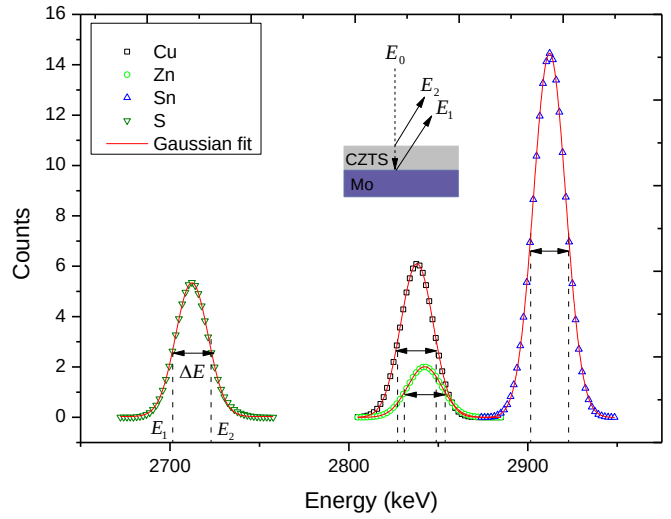

Figure 4. The Gaussian fit functions for these values with the fit values of experimental data SIMNRA program for Cu, Zn, Sn and S

As can be seen from Figures 3 and 4, a procedure was used to calculate the stopping power, that is, the energy loss from the signal height and energy width values of the respective elements in the RBS spectrum. Thus, energy loss along the paths of the incoming and outgoing protons on target was considered (Figure 4). To obtain the spectrum peaks of the individual elements, the positions of E_2, E_1 energy particles and ΔE widths equal to the full widths at half maximum (FWHM) scattered from the front and rear surfaces of the CZTS thin film, which are simulated with SIMNRA software and containing peaks of these elements, were obtained from the peak analysis. The simulated spectrum was

fitted with the Gaussian function by five times iterations with chi-square method $\left(\chi^2\right)$. Then, considering the linear approach, the stopping power of each element was calculated according to the following expressions:

$$S_i\left(\overline{E_i}\right)=\frac{\Delta E}{N_t\Delta x\left\{k\left|\sec\theta_i\right|+\dfrac{S_i\left(\overline{E_0}\right)}{S_i\left(\overline{E_i}\right)}\left|\sec\left(\theta_i-\theta_0\right)\right|\right\}} \tag{1}$$

$$S_0\left(\overline{E_0}\right)=\frac{\Delta E}{N_t\Delta x\left\{k\dfrac{S_0\left(\overline{E_i}\right)}{S_0\left(\overline{E_0}\right)}\left|\sec\theta_i\right|+\left|\sec\left(\theta_i-\theta_0\right)\right|\right\}} \tag{2}$$

Here, θ_0 and θ_i are the angles between the surface normal of the incoming and the scattered ions respectively. For details can be examined Ref. [6].

Before and after the scattering, followed by the assumption that the path of the projectile is straight and assuming the initial value of stopping power ratio is 1 ($S_i\left(\overline{E_0}\right)\big/S_i\left(\overline{E_i}\right)=S_0\left(\overline{E_i}\right)\big/S_0\left(\overline{E_0}\right)=1$), stopping power was expanded to the power series of the energy using the least squares method with iteration [7]:

$$S\left(E\right)=(a_1E^{-0.5}+a_2E^{-0.25}+a_3E^{0.25}+a_4E^{0.5}+a_5E^{0.75})\big/\Delta x \tag{3}$$

Where a's are the coefficients and unit of energy is eV. Finally, the stopping power values of the CZTS thin film were calculated with the Bragg's additivity rule [8].

2.1. Theoretical procedure

The stopping power of a material is defined as the average energy loss per unit path length and the total stopping power $\left(S\right)$ is the sum of collision $\left(S_{coll}\right)$ and nuclear $\left(S_{nuc}\right)$ constituents:

$$S\left(E\right)=S_{coll}\left(E\right)+S_{nuc}\left(E\right) \tag{4}$$

For protons, the highest addition to the total stopping power is supplied by the collision stopping power which based on inelastic collisions with target's electrons. Inversely, the least contribute to the total stopping power comes from nuclear stopping power which stem from elastic Coulomb collisions with target's nucleons and since it is only considerable at very low energies, it was not considered in this study.

The collision stopping power is specified by allowance the number of velocity-dependent effective charge and effective mean excitation energies of the target material. Taking into account the interaction potential between the protons with target in Ref [9], the collision stopping power for protons is given by

$$S_{coll}\left(E\right)=\frac{4\pi e^4}{m_ec^2\beta^2}Z^*\ln\left(\frac{q_{\max}}{q_{\min}}\right) \tag{5}$$

where e is charge of electron, $\beta=\upsilon/c$ is the proton's velocity in light velocity units, m_e is mass of electron, Z^* is the effective charge of target, $q_{\max}$ and $q_{\min}$ are maximum and minimum momentum transfer to the target from projectile, respectively.

In this present study, the electronic charge densities required for the effective charge and effective mean excitation energy of the target were calculated using atomic natural orbitals (ANO-RCC) from Gaussian type orbitals [10].

3. Results and Discussion

In Figure 3, it is seen that the simulation with SIMNRA is quite compatible with the experimental values. In the simulation, separate spectra were generated for constituents forming the CZTS thin film and for the Mo element. As expected, the fit distributions of the elements vary depending on the concentration in the film and the increased the cross-section with increasing atomic number. However, the peak of the Mo element appeared in the foreground plane due to its atomic number and thickness, and because the elements including the CZTS were not clearly visible. Especially, the peaks of the Cu and Zn elements were overlapped because of their atomic numbers were very close together, but still remained dimmed alongside the Mo peak. On the contrary, the Sn peak appeared a little more pronounced since the RBS analysis is very sensitive to heavy elements.

Table 1. Fit function coefficients for stopping power values of elements forming CZTS thin film

Elements	Coefficients				
	a_1	a_2	a_3	a_4	a_5
Cu	-4.59E+02	2.51E+02	-1.15E+00	-7.22E-01	7.09E-02
Zn	-7.06E+02	3.94E+02	-1.21E+01	1.21E+00	-2.77E-02
Sn	-1.80E+03	1.05E+03	-6.21E+01	1.04E+01	-5.17E-01
S	-8.74E+02	5.89E+02	-3.73E+01	6.17E+00	-2.98E-01

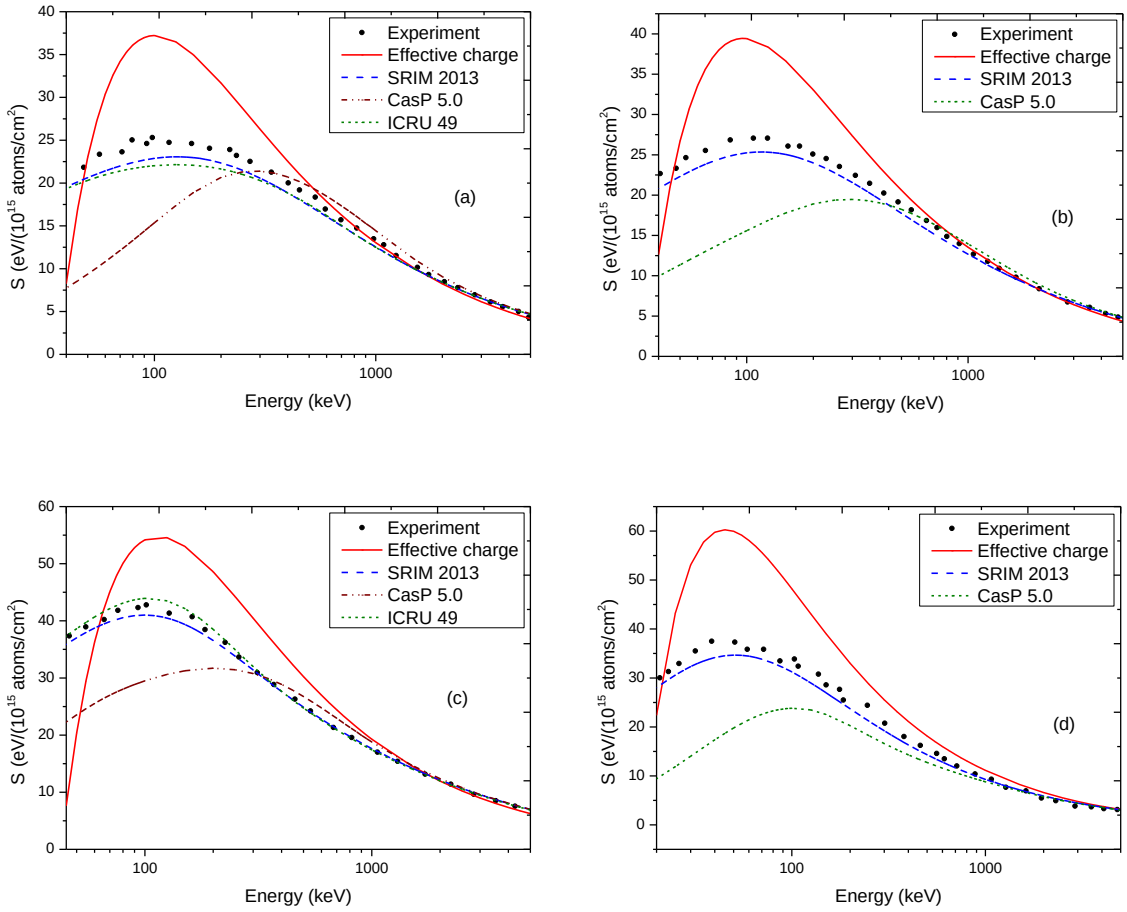

Figure 5. The stopping power values of (a) Cu (b) Zn (c) Sn (d) S

The coefficients related to the fit functions obtained by using Equation (3) are shown in Table 1 and Figures 5 (a)-(d) indicate the stopping power values of Cu, Zn, Sn and S acquired by these fit functions in the 45 keV-5 MeV energy range. Although the data are compatible with the energies of 1 MeV and above, there are differences in the low energies as expected. The peak point values in the stopping power curves of the experimental data seem to be closer to the ICRU [11] and SRIM [12]

values than the effective charge approach we used in this study. There are significant variances in the positions of the peaks for CasP [13] data. While the peak values of the curve in Cu, Zn and Sn are approximately 100 keV, this value is localized at approximately 300 keV for CasP. For S, these values are about 100 keV for CasP and 55-60 keV for the others. However, lower values than the peak points of the effective charge approach decrease very quickly compared to other reference data. Figure 6 represents the stopping power data of the CZTS thin film calculated according to the Bragg's sum rule with the fit function composed by matching the experimental data. The reference data included here are also the data of Andersen-Ziegler [14] and Ziegler-Biersack [15] currently available in the SIMNRA program. The values are generally compatible with each other, but an important point here is that there is little change between the fit function and the SRIM values in energies greater than 1 MeV. It is also noteworthy that the fit function and the energy values of the maximum of the effective charge approach overlap. The compliance rate with fit function was founded as 6.40% for SRIM, 7.49% for Ziegler-Biersack, 10.28% for Andersen-Ziegler, 16.45% for effective charge and 16.93 for CasP.

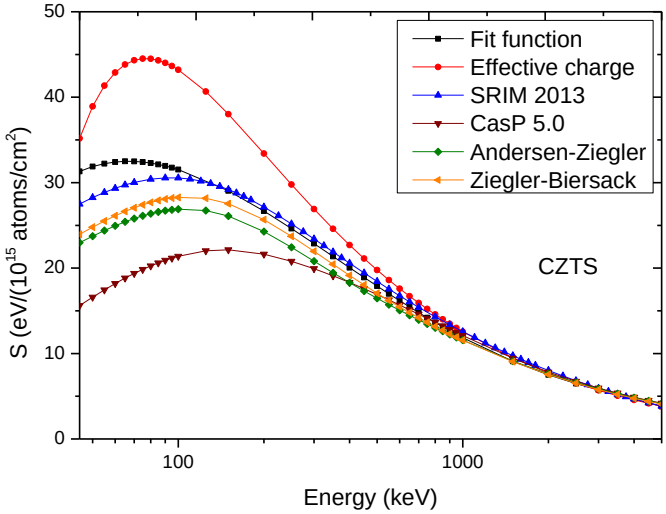

Figure 6. The stopping power of CZTS thin film

In this work, energy loss calculations of CZTS thin films were made by RBS technique. Accordingly, it is the SRIM data that is most compatible with the fit function. The effective charge approach handled under the Bethe-Bloch theory is actually valid for energies of 1 MeV and above, since it includes the first Born approximation. In this approach, no correction term was needed as the target's atomic numbers and mean excitation energies were taken as effective values. Based on the stopping power curve at the energies less than 1 MeV, it is very important that this method used gives reasonable results. The scattering peaks of these elements were obtained by corresponding the entire spectrum with the SIMNRA program since the scattering peaks of the elements constituting CZTS film were not visible. Therefore, it is worth noting that the method used is actually quasi-experimental rather than experimental. Even if the results are calculated by iteration, they have certain margins of error because they have been obtained directly by simulation instead of experimental. However, the results obtained may be applied to the conditions affecting the efficiency of the thin films used as solar cells as a result of exposure to radiation. In order to expand the study, CZTS thin film should be produced directly on the substrate and the corresponding peaks should be observed directly then the calculations should be done on this process. Also, the channeling effects were neglected in this study because the angle between the surface normal of target and the incoming beam was zero degrees. Therefore, to avoid these channeling effects, the incident beam should make a certain angle with the normal of the surface. In addition, to review the results with the dielectric theory and to use different orbital wave functions for the electronic charge density will carry the study to a different dimension.

4. Conclusion

In this paper, CZTS thin film structures used as solar cell were fabricated by means of sol-gel method and then RBS spectrum was gained by irradiating these films with protons in microbeam chamber. In the RBS spectrum of the thin film produced, a method for the calculation of energy loss was used for the position and energy width analysis of the respective peaks and a polynomial fit was determined for the stopping power of the CZTS thin film by making specific approaches. In addition, the effective charge approach that we used in our preceding studies for the stopping power was first discussed with atomic natural orbitals and it was perceived that the results were close to each other at certain error rates. The data obtained from this study will inspire the future studies on the interaction of radiation with matter.

Acknowledgment

I would like to thank Professor Žiga Šmit for his efforts on the experimental part of this work.

References

[1] Sigmund P. 2006. Particle Penetration and Radiation Effects: General Aspects and Stopping of Swift Point Charges. Springer.
[2] Pawar S.M., et al. 2010. Single step electrosynthesis of Cu2ZnSnS4 (CZTS) thin films for solar cell application. Electrochimica Acta, 55 (12): 4057-4061.
[3] Hironori K., et al. 2008. Enhanced Conversion Efficiencies of Cu 2 ZnSnS 4 -Based Thin Film Solar Cells by Using Preferential Etching Technique. Applied Physics Express, 1 (4): 041201.
[4] Eckstein W., Mayer M. 1999. Rutherford backscattering from layered structures beyond the single scattering model. Nuclear Instruments and Methods in Physics Research Section B: Beam Interactions with Materials and Atoms, 153 (1): 337-344.
[5] Siegel J.M., L.E.G. 1951. Radiochemical Studies: The Fission Products. National Nuclear Energy Series IV. New York: McGraw-Hill.
[6] Stoquert J.P., et al. 1982. Alpha particle stopping cross sections of Cu and Au at energies below 3 MeV. Nuclear Instruments and Methods in Physics Research, 194 (1): 51-55.
[7] Abdesselam M., et al. 2008. Stopping of 0.3–1.2 MeV/u protons and alpha particles in Si. Nuclear Instruments and Methods in Physics Research Section B: Beam Interactions with Materials and Atoms, 266 (18): 3899-3905.
[8] Bragg W.H., Kleeman R. 1905. XXXIX. On the α particles of radium, and their loss of range in passing through various atoms and molecules. Philosophical Magazine Series 6, 10 (57): 318-340.
[9] Usta M., et al. 2018. Stopping power and dose calculations with analytical and Monte Carlo methods for protons and prompt gamma range verification. Nuclear Instruments and Methods in Physics Research Section A: Accelerators, Spectrometers, Detectors and Associated Equipment, 897: 106-113.
[10] Aquilante F., et al. 2016. Molcas 8: New capabilities for multiconfigurational quantum chemical calculations across the periodic table. Journal of Computational Chemistry, 37 (5): 506-541.
[11] ICRU. 1993. Stopping Powers and Ranges for Protons and Alpha Particles, in ICRU Report 49.
[12] Ziegler J.F., Biersack J.P., Ziegler M.D. 2013. SRIM, the Stopping and Range of Ions in Matter. SRIM Company.
[13] Grande P.L., Schiwietz G. 2009. Convolution approximation for the energy loss, ionization probability and straggling of fast ions. Nuclear Instruments and Methods in Physics Research Section B: Beam Interactions with Materials and Atoms, 267 (6): 859-865.
[14] Andersen H.H., Ziegler J.F. 1977. Hydrogen Stopping powers and ranges in all elements. United States: Pergamon Press.
[15] Ziegler J.F., Biersack J.P. 1985. The Stopping and Range of Ions in Matter, in Treatise on Heavy-Ion Science: Volume 6: Astrophysics, Chemistry, and Condensed Matter, D.A. Bromley, Editor. 1985, Springer US: Boston, MA. p. 93-129.

Araştırma Makalesi / Research Article

Calculation of Radiogenic Heat Productions from Marble and Glazed Tiles Used as Covering Building Materials in Turkey

Aybaba HANÇERLİOĞULLARI*, Şeref TURHAN, Aslı KURNAZ

Kastomunu University, Faculty of Science and Letters, Department of Physics, 37150, Kastamonu, Turkey
(ORCID: 0000-0001-7008-480X)(ORCID: 0000-0001-5303-3680) (ORCID: 0000-0002-7910-3461)

Abstract
In this study, radiogenic heat productions of marble and glazed tiles samples are calculated based on the elemental concentrations of uranium (in terms of mg/kg), thorium (in terms of mg/kg) and potassium (in terms of %) in the samples collected from various provinces in Turkey. The radiogenic heat productions from the marble tile samples varied from 0.05 to 2.17 μW/m3 with an average of 0.26 μW/m3. The average of the radiogenic heat production of the marble tile samples is approximately four times lower than the average continental crust of 0.9 μW/m3.

Keywords: Marble, Radiogenic heat production, Building materials.

Türkiye'de kaplama yapı malzemesi olarak kullanılan mermer ve sırlı karolardan radyojenik ısı üretiminin hesaplanması

Öz
Bu çalışmada, Türkiye'nin çeşitli illerinden toplanan mermer ve sırlı karo örneklerinin radyojenik ısı üretimi, uranyumun (mg/kg cinsinden), toryumun (mg/kg cinsinden) ve potasyumun (% cinsinden) temel konsantrasyonlarına göre hesaplanmıştır. Mermer karo örneklerinden elde edilen radyojenik ısı üretimi, ortalama 0.26 μW/m3 olam üzere 0.05 ile 2.17 μW/m3 arasında değişmektedir. Mermer karo örneklerinin radyojenik ısı üretiminin ortalaması, 0.9 μW/m3 ortalama kıtasal kabuk değerindenyaklaşık dört kat daha düşüktür.

Anahtar kelimeler: Mermer, Radyojenik ısı üretimi, Yapı malzemeleri.

1. Introduction

The radioactive elements that cause this are divided into two groups as short and long half-life isotopes. Long half-life radionuclides such as the member of natural radioactive series of uranium †(^{238}U), thorium (^{232}Th), actinium (^{235}U), and radioactive potassium (^{40}K). The two main radionuclides, ^{238}U (half-life of 4.5 x10^9 y) and ^{235}U (half-life of 0.7 x10^9 y), decay into lead, ^{206}Pb and ^{207}Pb, respectively.

In this study, radiogenic heat productions of marble tiles are calculated based on the elemental concentrations of uranium (in terms of mg/kg), thorium (in terms of mg/kg) and potassium (in terms of %) in the samples collected from various provinces in Turkey.

2. Material and Method

The elemental concentrations (EC) using the following formula:

$$EC = \frac{W \times A_C \times F}{\lambda_E \times N_{Av.} \times IA_E} \quad (1)$$

*Sorumlu yazar: aybaba@kastamonu.edu.tr
Geliş Tarihi: 15.10.2019, Kabul Tarihi: 19.12.2019

The elemental concentration of ^{238}U was calculated. The radioactive heat production (H in $\mu W/m^3$) of given rocks or building materials can be calculated by using the equation [2]:

$$H = \rho \times (9.52 \times C_U + 2.56 \times C_{Th} + 3.48 \times C_K) \times 10^{-5} \quad (2)$$

where ρ is the bulk density of the rock or building material (in kg/m^3), C_U, C_{Th} and C_K is elemental concentration of U (in terms of mg/kg), Th (in terms of mg/kg) and K (in terms of %), respectively.

3. Results and Discussion

The values of elemental concentrations of U, Th and K in marble tile samples, and radiogenic heat productions calculated for marble tile samples are given in Table 1. It is seen from Table 1 that the elemental concentrations of U, Th and K varied from 0.1 to 4.6 mg/kg with an average of 0.7 mg/kg, 0.2 to 20.4 mg/kg with an average of 1.5 mg/kg and 0.04 to 2.4% with an average of 0.2%, respectively. The highest concentration of ^{238}U was measured in marble tile sample coded of MRB5 while the lowest concentration of ^{238}U was measured in marble tile samples coded of MRB17 and MRB25. The highest concentration of ^{232}Th and ^{40}K was measured in marble tile sample coded of MRB4 while the lowest concentration of ^{232}Th and $^{40}K$was measured in marble tile samples coded of MRB13 and MRB12, respectively. The value of H from marble samples varied from 0.05 to 2.17 $\mu W/m^3$ with an average of 0.26 $\mu W/m^3$. The highest value of radiogenic heat production was calculated in marble tile sample coded of MRB4. Comparison of the average value of the H calculated for the marble samples studied with those calculated for different rocks types is given in Table 2. From Table 2, the average value of the marble H is lower than those of rock types.

4. Conclusions

The average of concentration of U, Th and K in marble samples is lower than the average value of earth's crust of 2.5, 13 and 25000 mg/kg, respectively [6]. The average of the radiogenic heat production of the marble tile samples is approximately four times lower than the average continental crust of 0.9 $\mu W/m^3$. The contribution of ^{238}U, ^{232}Th and ^{40}K to total radiogenic heat production is estimated as 60%, 34% and 6%, respectively. The results revealed that radiogenic heat production by the marble samples varies according to the geological structure of the region.

Table 1. The values of radiogenic heat production of the marble samples

Sample code	^{238}U	^{232}Th	^{40}K	H ($\mu W/m^3$)
	mg/kg	mg/kg	(%)	
MRB1	0.3	0.8	0.2	0.13
MRB2	0.9	1.1	0.2	0.30
MRB3	0.6	1.0	0.2	0.21
MRB4	3.3	20.2	2.4	2.17
MRB5	4.6	0.8	0.1	1.08
MRB6	0.3	0.8	0.1	0.11
MRB7	2.4	0.6	0.1	0.58
MRB8	0.2	0.8	0.0	0.09
MRB9	1.9	2.3	0.3	0.59
MRB10	0.2	0.3	0.0	0.06
MRB11	0.2	0.3	0.0	0.06
MRB12	0.2	0.3	0.0	0.06
MRB13	0.5	0.2	0.1	0.13
MRB14	0.6	0.8	0.0	0.18
MRB15	0.3	0.6	0.1	0.11
MRB16	0.1	0.3	0.1	0.05
MRB17	0.1	0.3	0.1	0.05
MRB18	0.2	0.5	0.1	0.08
MRB19	0.4	0.6	0.0	0.14
MRB20	0.2	0.4	0.1	0.07
MRB21	0.1	0.5	0.1	0.06
MRB22	0.2	0.6	0.1	0.09

MRB23	0.3	0.8	0.1	0.12
MRB24	1.2	3.0	1.2	0.55
MRB25	0.1	0.3	0.1	0.05
MRB26	0.4	2.5	0.1	0.25
MRB27	0.5	1.1	0.1	0.19
MRB28	0.2	0.8	0.0	0.10
MRB29	0.2	0.6	0.1	0.08
MRB30	0.3	0.6	0.1	0.10
Average	0.7	1.5	0.2	0.26
Standard deviation	1.0	3.6	0.5	0.42
Standard error	0.2	0.7	0.1	0.08
Min	0.1	0.2	0.04	0.05
Max	4.6	20.2	2.4	2.17

Table 2. Comparison of the marble H with those calculated for different rocks [7]

Type of Rock	H ($\mu W/m^3$)
Granite (Egypt)	9.53
Granite (South Africa)	3.51
Quartz diorite (Egypt)	1.76
Quartz diorite (California)	0.40
Acidic rocks	2.38
Acidic rocks	2.84
Lamprophyre (Egypt)	1.74
Swiss Alps	1.12
Basalt (Egypt)	0.11
Basalt (Japan)	0.80
Basalt (Former USSR)	0.39
Metamorphic (Marble-Turkey)	0.26

References

[1] McKenna T.E., Sharp I.M. 1998. Radiogenic heat production in sedimentary rocks of the Gulf of Mexico Basin, South Texas. AAPG Bulletin, 82 (3): 484–496.

[2] Clauser C. 2011. Radiogenic heat production of rocks. In: Harsh Gupta (Ed.), Encyclopedia of Solid Earth Gophysics, 2nd ed., Springer, Dordrecht, preprint.

[3] UNSCEAR (United Nations Scientific Committee on the Effects of Atomic Radiation). 2000. Sources and effects of ionizing radiation. United Nations Publication, New York, USA.

[4] Turhan Ş., Varinlioğlu A. 2012. Radioactivity measurement of primordial radionuclides in and dose evaluation from marble and glazed tiles used as covering building materials in Turkey. Radiation Protection Dosimetry, 151 (3): 546-555.

[5] Rybach L. 1988. Determination of heat production rate. In: Haenel, R., Rybach, L., Stegena, L. (Eds.), Handbook of Terrestrial Heat-Flow Density Determination. Kluwer Academic Publishers, Dordrecht, pp.125–142.

[6] Yaroshevsky A.A. 2006. Abundance of chemical elements in the earth's crust. Geochemistry International, 44 (1): 54-62.

[7] Abbady A.G.E. El-Arabi A.M., Abbady A. 2004. Heat production rate from radioactive elements in igneous and metamorphic rocks in Eastern Desert, Egypt. VII Radiation Physics & Protection Conference, pp. 287-294, 27-30 November 2004, Ismailia-Egypt.

Araştırma Makalesi / Research Article

Calculations of Spontaneous Fission (SF) half-lives of superheavy nuclei in different models

Asım SOYLU*

Niğde Ömer Halisdemir University, Physics Department, Niğde
(ORCID: 0000-0002-4656-7200)

Abstract
The spontaneous fission (SF) is a decay mode for heavy and superheavy nuclei (Z≥90) and it is an important confining factor explaning the stability of synthesized superheavy nuclei. Since the fission decay is complex, it is difficult to explain such a multi-dimensional system in a complete microscopic manner. In this study, SF half-lives of ^{284}Cn and ^{284}Fl superheavy nuclei are investigated using the direct method, the Universal Decay Law (UDL). The fission decay constant for each possible case is computed by using the UDL and then the SF half-life for ^{284}Cn and ^{284}Fl superheavy nuclei are predicted. The calculated SF half-lives are compared with the results of other semi-empirical models and the experimental data. Furthermore, the results are compared with ones of the model in which they proposed this direct method for the SF by using CPPM potentials. Good agreement has been obtained between the results of present approach and the others. This study shows that UDL would also be used in the half-lives calculations of Spontaneous Fission of superheavy nuclei in a direct way.

Keywords: Superheavy, Half-lives, Spontaneus Fission.

Süper-ağır çekirdeklerin kendiliğinden fisyon yarı ömürlerinin farklı modellerdeki hesaplamaları

Öz
Kendiliğinden Fisyon (SF) Z≥90 olan ağır ve süper-ağır çekirdekler için bir bozunma modudur ve süper-ağır çekirdeğin sentezinin kararlılığını tanımlayan önemli bir sınırlandırma faktörüdür. Fisyon bozunması karmaşık olduğu için, böyle çok boyutlu bir sistemin açıklamasını yapmak zordur. Bu çalışmada, ^{284}Cn ve ^{284}Fl süper-ağır çekirdeklerinin kendiliğinden fisyon yarı-ömürleri doğrudan bir metot olan evrensel bozunma yasası (UDL) kullanılarak araştırıldı. Her bir mümkün bozunma durumu için fisyon bozunma sabitleri UDL ile hesaplandı ve sonrasında ^{284}Cn ve ^{284}Fl için SF yarı-ömürleri tahmin edildi. Elde edilen SF yarı-ömürleri diğer yarı-ampirilk formüller ve deneysel değerleriyle kıyaslandı. Ayrıca sonuçlar diğer doğrudan model olan CPPM potansiyeli modeli sonuçlarıyla karşılaştırıldı. Bu yaklaşımların sonuçları arasında iyi bir uyum elde edildi. Bu çalışma UDL metodunun da doğrudan metot olarak kendiliğinden fisyon yarı ömürlerinin hesaplamalarında kullanılabileceğini gösterdi.

Anahtar kelimeler: Süper-ağır, Yarı-ömürler, Kendiliğinden Fisyon.

1. Introduction

More recently, investigation of α decay (AD) of superheavy nuclei has been popular for both the experimental and theoretically in nuclear area. When superheavy nuclei are produced in an experiment, they go to the ground state via α decays. Counting these α particles give important information on the synthesis of nuclei. Therefore, it is very important to make theoretical studies on the α decay of superheavy nuclei [1-7]. On the other hand, these decays can sometimes be in the form of the

*Sorumlu yazar: asimsoylu@gmail.com
Geliş Tarihi: 23.12.2019, Kabul Tarihi: 24.12.2019

spontaneous fission (SF) [8]. Although these phenomena are studied through the quantum mechanical tunneling [9,10], the SF is more complex. Since there are many uncertainties and complexity in the fission process, it is very difficult to describe it in a complete microscopic manner of such a multidimensional system. Xu and others have studied the half-lives of the AD and SF for heavy and super-heavy nuclei with Z ≥90 protons systematically [11]. In recent years, Santhosh et al. predicted half-life and decay modes of all 104≤ Z≤136 isotopes of superheavy nuclei and compared results with the AD half-lives [12].

In Ref. [13], isotopic yields and half-lives of ^{284}Cn and ^{284}Fl superheavy nuclei have been investigated by using CPPM as a direct way. Decay constant for each combination has been computed and then the total decay constant and fission half-life for ^{284}Cn and ^{284}Fl superheavy nuclei have been predicted. Good agreement has been obtained between the results of present study and the experimental data. Furthermore, some predictions have been made on heavier cluster decays from superheavy nuclei [14] by using different models. It has been found in Ref. [15] that the UDL formula [16] could predict the lighter and heavier cluster decay owing to the inclusion of the preformation and fission-like mechanisms. In this study, using UDL approach [16] that works well for cluster decay as a direct way, the SF half-lives of ^{284}Cn and ^{284}Fl superheavy nuclei have been investigated. The SF half-lives have also been computed with the formulas of Bao [17] and Soylu [18]. The obtained half-lives are compared with the results of other models and present experimental data.

2. Models

2.1. Universal Decay Law (UDL)

Qi et al. proposed a universal decay law (UDL) for the decays (α and cluster) by helping R-Matrix theory and the microscopic mechanism [16] as follows

$$\log_{10} T_{1/2} = aZ_cZ_d\sqrt{\frac{A}{Q_c}} + b\sqrt{AZ_cZ_d(A_d^{1/3} + A_c^{1/3})} + c \quad (1)$$

where $A=A_cA_d/(A_c+A_d)$ and the constants a=0.4314, b=-0.4087, c=-25.7725 by fitting above equation to α and cluster decays experimental data [16].

2.2. The formula of Bao et al.

Bao et al. [17] derived a formula for the SF half-lives considering of the shell and isospin effect, this formula is given by

$$\log_{10} T_{1/2}(yr) = c_1 + c_2\left(\frac{Z^2}{(1-kI^2)A}\right) + c_3\left(\frac{Z^2}{(1-kI^2)A}\right)^2 + c_4E_{sh} + h_i \quad (2)$$

The using parameters in this formula can be found in Ref. [17].

2.3. Formula of Soylu

A new function that was proposed for the SF half-lives [18] is given by

$$T_{SF} = e^{2\pi[aA+bA^{2/3}+cZ(Z-1)/A^{1/3}+d(N-Z)^2/A+eZ^4+f]} \quad (3)$$

where Z, N and A are the proton, neutron and mass numbers of the parent nuclei and a, b, c, d, e, f are the adjustable parameters obtained by fitting it to present experimental data and this equation is in terms of years. The parameters are given by a=-10.0987592959, b=119.319858732, c=-0.516609881059, d=-9.52538327068, e=1.92155604207.10-6, f=-1496.05967574 [18].

3. Results

UDL approach was applied to ^{284}F1 nucleus and λ values for each case were obtained. The results obtained are given in Table 1 for different cases. Using these λ values, SF half-lives were obtained for ^{284}F1. This value,-4.8750, is given in the Table 3. On the other hand, the same process was applied for ^{284}Cn and results were obtained. The obtained λ values and half-life value,-3.884, are given in the Tables 2 and 3. By using semiempirical formulas given in Eqs.2 and 3, the SF half-lives have been calculated for related nuclei. These values are presented in Table 3. It should be noted that the MES code [19] in Python language has been used for the calculations in this study.

Table 1. Spontaneous fission constant for each individual fragmentation of ^{284}F1superheavy nucleus.

A_1	A_2	Q (MeV)	λ (s^{-1})	A_1	A_2	Q (MeV)	λ (s^{-1})
^{4}He	^{280}Cn	10.80	2.71e+01	^{118}Pd	^{166}Er	309.23	2.68e-07
^{8}Be	^{276}Ds	21.44	9.52e-19	^{119}Ag	^{165}Ho	312.46	2.80e-06
^{9}Be	^{275}Ds	16.00	2.34e-38	^{120}Cd	^{164}Dy	318.85	3.56e-02
^{10}Be	^{274}Ds	17.11	7.95e-37	^{121}Cd	^{163}Dy	316.38	2.08e-04
^{11}Be	^{273}Ds	10.38	3.99e-78	^{122}Cd	^{162}Dy	317.71	3.90e-03
^{12}Be	^{272}Ds	7.82	5.65e-110	^{123}Cd	^{161}Dy	314.39	3.44e-06
^{13}B	^{271}Mt	21.26	2.45e-51	^{124}Sn	^{160}Gd	325.10	2.12e+01
^{14}C	^{270}Hs	40.79	3.91e-21	^{125}Sn	^{159}Gd	323.38	6.39e-01
^{15}C	^{269}Hs	34.49	1.57e-35	^{126}Sn	^{158}Gd	325.62	7.43e+01
^{16}C	^{268}Hs	32.40	1.96e-42	^{127}Sn	^{157}Gd	323.21	5.24e-01
^{72}Ni	^{212}Rn	231.81	2.63e-12	^{128}Sn	^{156}Gd	324.82	1.60e+01
^{78}Zn	^{206}Po	244.59	7.38e-11	^{129}Sb	^{155}Eu	325.37	3.08e+00
^{82}Ge	^{202}Pb	260.28	5.75e-06	^{130}Te	^{154}Sm	328.73	3.16e+02
^{83}Ge	^{201}Pb	255.17	8.54e-11	^{131}Te	^{153}Sm	326.69	4.86e+00
^{84}Ge	^{200}Pb	253.32	1.49e-12	^{132}Te	^{152}Sm	328.87	4.71e+02
^{86}Se	^{198}Hg	270.38	1.21e-05	^{133}Te	^{151}Sm	326.43	3.12e+00
^{87}Se	^{197}Hg	265.89	7.77e-10	^{134}Te	^{150}Sm	328.50	2.41e+02
^{88}Se	^{196}Hg	264.63	5.43e-11	^{135}I	^{149}Pm	291.51	1.13e-35
^{92}Kr	^{192}Pt	273.98	1.51e-10	^{136}Xe	^{148}Nd	332.76	5.01e+04
^{96}Sr	^{188}Os	282.98	1.21e-09	^{137}Xe	^{147}Nd	329.45	5.69e+01
^{102}Zr	^{182}W	288.75	6.14e-11	^{138}Xe	^{146}Nd	329.82	1.25e+02
^{108}Mo	^{176}Hf	294.25	9.84e-12	^{139}Xe	^{145}Nd	326.00	4.31e-02
^{112}Ru	^{172}Yb	303.81	5.79e-08	^{140}Xe	^{144}Nd	325.65	2.12e-02
^{113}Ru	^{171}Yb	300.10	1.82e-11	^{141}Ba	^{143}Ce	330.26	5.61e+01
^{114}Ru	^{170}Yb	299.91	1.30e-11	^{142}Ba	^{142}Ce	331.30	4.79e+02
^{115}Rh	^{169}Tm	304.43	1.03e-09				
^{116}Pd	^{168}Er	311.74	4.95e-05				
^{117}Pd	^{167}Er	308.64	6.66e-08				

Table 2. Spontaneous fission constant for each individual fragmentation of ^{284}Cn superheavy nucleus.

A_1	A_2	Q (MeV)	λ (s^{-1})	A_1	A_2	Q (MeV)	λ (s^{-1})
^{4}He	^{280}Ds	9.61	8.89e-02	^{113}Ru	^{171}Er	292.14	2.28e-10
^{8}Be	^{276}Hs	19.32	6.54e-23	^{114}Ru	^{170}Er	292.88	1.32e-09
^{9}Be	^{275}Hs	14.58	1.26e-42	^{115}Rh	^{169}Ho	295.58	2.92e-09
^{10}Be	^{274}Hs	16.45	1.21e-37	^{116}Pd	^{168}Dy	300.94	3.65e-06
^{11}Be	^{273}Hs	10.48	8.58e-75	^{117}Pd	^{167}Dy	298.90	4.49e-08
^{12}Be	^{272}Hs	8.46	6.99e-99	^{118}Pd	^{166}Dy	300.52	1.75e-06
^{13}B	^{271}Bh	20.07	7.22e-54	^{119}Ag	^{165}Tb	301.77	3.79e-07
^{14}C	^{270}Sg	38.04	1.79e-24	^{120}Cd	^{164}Gd	306.28	1.65e-04
^{15}C	^{269}Sg	32.92	2.83e-37	^{121}Cd	^{163}Gd	304.94	9.68e-06
^{72}Ni	^{212}Po	227.15	3.63e-11	^{122}Cd	^{162}Gd	307.44	2.43e-03
^{73}Ni	^{211}Po	225.09	3.48e-13	^{123}Cd	^{161}Gd	305.47	3.61e-05
^{74}Ni	^{210}Po	226.96	2.97e-11	^{124}Sn	^{160}Sm	311.02	1.14e-02
^{77}Cu	^{207}Bi	231.22	1.47e-12	^{125}Sn	^{159}Sm	310.65	5.59e-03
^{78}Zn	^{206}Pb	243.82	1.57e-05	^{126}Sn	^{158}Sm	313.81	5.17e+00
^{79}Zn	^{205}Pb	239.75	2.01e-09	^{127}Sn	^{157}Sm	312.70	5.14e-01
^{80}Zn	^{204}Pb	239.31	8.32e-10	^{128}Sn	^{156}Sm	315.27	1.29e+02
^{82}Ge	^{202}Hg	255.31	2.67e-04	^{129}Sn	^{155}Sm	314.12	1.02e+00
^{83}Ge	^{201}Hg	251.19	3.50e-08	^{130}Te	^{154}Nd	315.72	4.38e+00
^{84}Ge	^{200}Hg	250.20	4.38e-09	^{131}Te	^{153}Nd	315.09	1.20e+00
^{86}Se	^{198}Pt	262.96	6.52e-06	^{132}Te	^{152}Nd	317.89	4.69e+02
^{87}Se	^{197}Pt	259.40	2.85e-09	^{133}Te	^{151}Nd	316.43	2.26e+01
^{88}Se	^{196}Pt	259.08	1.61e-09	^{134}Te	^{150}Nd	318.76	3.22e+03
^{90}Se	^{194}Pt	253.11	2.21e-15	^{135}I	^{149}Pr	280.12	9.90e-37
^{92}Kr	^{192}Os	267.20	7.14e-10	^{136}Xe	^{148}Ce	319.38	8.74e+02
^{96}Sr	^{188}W	274.14	1.45e-10	^{137}Xe	^{147}Ce	316.95	5.29e+00
^{98}Sr	^{186}W	271.48	4.38e-13	^{138}Xe	^{146}Ce	318.16	7.01e+01
^{102}Zr	^{182}Hf	280.19	3.18e-11	^{139}Xe	^{145}Ce	315.26	1.51e-01
^{103}Zr	^{181}Hf	277.77	1.44e-13	^{140}Xe	^{144}Ce	315.97	6.88e-01
^{108}Mo	^{176}Yb	286.80	1.52e-10	^{141}Ba	^{143}Ba	316.22	4.84e-01
^{110}Mo	^{174}Yb	284.04	3.46e-13	^{142}Ba	^{142}Ba	318.23	3.51e+01
^{111}Tc	^{173}Tm	287.83	3.83e-12				
^{112}Ru	^{172}Er	294.67	5.80e-08				

Table 3. Spontaneous fission half-lives for ^{284}Fl and ^{284}Cn superheavy nucleus in different models.

	UDL(direct way)	Soylu (Eq.3)	Bao (Eq.2)	CPPM (direct way) [13]	Exp. [20,21]
^{284}Fl	-4.8750	2.4688	0.3304	-3.83	-2.602
^{284}Cn	-3.8443	-4.0197	-2.1547	-3.48	1.001

4. Conclusion

In this study, the Spontaneous Fission (SF) half-lives of ^{284}Fl and ^{284}Cn superheavy nuclei are calculated using the direct method, the Universal Decay Law (UDL). The calculated SF half-lives are compared with the results of the model using the CPPM, other semi-empirical formulas and the present experimental data. Good agreement is obtained between the results of present approach and the others. It has been shown that UDL would also be used in the half-lives calculations of Spontaneous Fission of superheavy nuclei in a direct way. Present mechanism could be applied to obtain SF half-lives of new superheavy nuclei.

Acknowledgments

This work has been supported by the Turkish Science and Research Council (TUBİTAK) with Project No: 118R028.

References

[1] Oganessian Y.T., Utyonkov V.K., Dmitriev S.N., Lobanov Y.V., Itkis M.G., Polyakov A.N., Sokol E.A. 2005. Synthesis of elements 115 and 113 in the reaction Am243+Ca 48. Physical Review C, 72 (3): 034611.

[2] Oganessian Y.T., Utyonkov V.K., Lobanov Y.V., Abdullin F.S., Polyakov A.N., Sagaidak R. N., Bogomolov S.L. 2006. Synthesis of the isotopes of elements 118 and 116 in the cf 249 and cm 245+ ca 48 fusion reactions. Physical Review C, 74 (4): 044602.

[3] Poenaru D.N., Gherghescu R.A. 2018. α decay and cluster radioactivity of nuclei of interest to the synthesis of Z= 119, 120 isotopes. Physical Review C, 97 (4): 044621.

[4] Santhosh K.P., Nithya C. 2018. Predictions on the modes of decay of even Z superheavy isotopes within the range 104≤ Z≤ 136. Atomic Data and Nuclear Data Tables, 119: 33-98.

[5] Ni D., Ren Z. 2009. Microscopic calculation of α-decay half-lives with a deformed potential. Physical Review C, 80 (5): 051303.

[6] Zhang G.L., Le X.Y., Zhang H.Q. 2009. Calculation of α preformation for nuclei near N= 162 and N= 184. Physical Review C, 80 (6): 064325.

[7] Mirea M., Budaca R., Sandulescu A. 2017. Spontaneous fission, cluster emission and alpha decay of 222Ra in a unified description. Annals of Physics, 380: 154-167.

[8] Bohr N., Wheeler J.A. 1939. The mechanism of nuclear fission. Physical Review, 56 (5): 426.

[9] Gamow G. 1928. Zur quantentheorie des atomkernes. Zeitschrift für Physik, 51 (3-4): 204-212.

[10] Gurney R.W., Condon E.U. 1928. Wave mechanics and radioactive disintegration. Nature, 122 (3073): 439.

[11] Xu C., Ren Z., Guo Y. 2008. Competition between α decay and spontaneous fission for heavy and superheavy nuclei. Physical Review C, 78 (4): 044329.

[12] Santhosh K.P., Biju R.K., Sahadevan S. 2010. Semi-empirical formula for spontaneous fission half life time. Nuclear Physics A, 832 (3-4): 220-232.

[13] Pahlavani M.R., Joharifard M. 2019. Isotopic yield and half-life of spontaneous fission for Cn284 and Fl 284 superheavy isobars using direct calculation and semiempirical formulas. Physical Review C, 99 (4): 044601.

[14] Poenaru D.N., Stöcker H. Gherghescu R.A. 2018. Cluster and alpha decay of superheavy nuclei. The European Physical Journal A, 54 (2): 14.

[15] Zhang Y.L., Wang Y.Z. 2018. Systematic study of cluster radioactivity of superheavy nuclei. Physical Review C, 97 (1): 014318.

[16] Qi C., Xu F.R., Liotta R.J., Wyss R. 2009. Universal decay law in charged-particle emission and exotic cluster radioactivity. Physical review letters, 103 (7): 072501.

[17] Bao X.J., Guo S.Q., Zhang H.F., Xing Y.Z., Dong J.M., Li J.Q. 2015. Competition between α-decay and spontaneous fission for superheavy nuclei. Journal of Physics G: Nuclear and Particle Physics, 42 (8): 085101.

[18] Soylu A.2019. Search for decay modes of heavy and superheavy nuclei. Chinese Physics C, 43 (7): 074102.

[19] Soylu A. 2019. MES: A Code for Calculations of Half-lives of Alpha, Cluster Decays and Spontaneous Fission, Prediction of Decay Modes of Superheavy Nuclei, unpublished.

[20] Audi G., Kondev F.G., Wang M., Huang W.J., Naimi S. 2017. The NUBASE2016 evaluation of nuclear properties. Chinese Physics C, 41 (3): 030001.

[21] Utyonkov V.K., Brewer N.T., Oganessian Y.T., Rykaczewski K.P., Abdullin F.S., Dmitriev S.N., Roberto J.B. 2015. Experiments on the synthesis of superheavy nuclei Fl 284 and Fl 285 in the Pu 239, 240+ Ca 48 reactions. Physical Review C, 92 (3): 034609.

Derleme Makalesi / Review Article

Investigation of the High Radiation Levels in Plio-Quaternary Volcanic and Pyroclastic Rocks Used as Building Raw Materials in Isparta Volcanic Area, SW Turkey

Hakan ÇOBAN*

Bitlis Eren University, Engineering and Architecture Faculty, Department of Civil Engineering, Bitlis
(ORCID: 0000-0002-9614-6818)

Abstract

Available natural radioactivity (^{40}K, ^{238}U, ^{232}Th) measurements on Plio-Quaternary volcanic and pyroclastic rocks, which are usually used as building raw materials, from the Isparta region of SW Turkey, released that their radium equivalent activity values are close to the internationally accepted upper limits and a potential radiation risk. In this study, the relationship between their magma and source characteristics has been investigated to reveal the reason of the high radiation values in these volcanic materials carrying value by more than three times the equivalent materials in Turkey. Recent volcanological studies have shown that potassic-ultrapotassic magmas governed the genesis of the Isparta volcanism. Potassium-rich characters and elevated concentrations of radiogenic (e.g.,Th and U) and total rare earth elements (∑REE) are their most diagnostic features. These characteristics are also similar to some mantle-derived carbonatites (e.g., Norwage and Kenya) with high radiation levels. To support this, recent investigations also revealed that the origin of Isparta potassic volcanism is associated with a common and enriched mantle source, which were interacted with carbonatite melts. Accordingly, carbonatitic melts left their geochemical imprints into their mantle sources, and partial melting of this mantle source produced K, REE, Th, and U-rich volcanic materials with high radiation levels in the region. These results indicate that the carbonatite-influenced mantle source were played a key role for not only enrichments in distinct elements (e.g., Th, U and REE) but also high radioactivity levels in Isparta volcanic and pyroclastic rocks. In this study, attention is drawn to the fact that a potential risk of high radiation in volcanic and pyroclastic rocks used as building raw materials can be expected for a given volcanic region, which include potassic magma derived from a carbonatite-modified mantle source.

Keywords: Isparta, potassic volcanism, carbonatitic affinity, high radiation, building materials

Isparta (GB Türkiye) Volkanik Alanında Yapı Malzemesi Olarak Kullanılan Pliyo-Kuvaterner yaşlı Volkanik ve Piroklastik Kayaçlardaki Yüksek Radyasyonun İncelenmesi

Öz

Isparta bölgesinde (GB Türkiye), genellikle yapı hammaddesi olarak kullanılan, Pliyo-Kuvaterner yaşlı volkanik ve piroklastik kayaçlarda belirlenmiş olan mevcut doğal radyoaktivite (^{40}K, ^{238}U, ^{232}Th) ölçümleri, radyum eşdeğer aktivite değerlerinin, uluslararası kabul edilebilir üst limitlerine ve potansiyel bir radyasyon riskine yakın değerler olduğunu açığa çıkarmıştır. Türkiye'deki eşdeğer materyallere göre üç kat fazla değerler taşıyan bu volkanik materyallerdeki yüksek radyasyon seviyelerine neyin sebep olduğunu çözümlemek için, burada, onları üreten mağmalar ve türedikleri kaynak arasındaki ilişki araştırılmıştır. Son güncel volkanolojik çalışmalar, Isparta volkanizmasının jenezini potasik ve ultrapotasik mağmaların kontrol ettiğini göstermiştir. Potasyumca zengin karakterleri ve yüksek konsantrasyonlardaki radyojenik element (örn., Th ve U) ve toplam nadir toprak element (∑NTE) içerikleri, onların en tanımlayıcı özellikleridir. Bu karakteristikler aynı zamanda, yüksek radyasyon seviyeli bazı karbonatitlerin (örn., Norveç ve Kenya karbonatitlerinin) karakteristiklerine benzerdir. Bunu destekleyecek şekilde, son zamanlardaki araştırmalar, Isparta potasik volkanizmasının orjininin, karbonatit

*Sorumlu yazar: hcoban@beu.edu.tr
Geliş Tarihi: 20.10.2019, Kabul Tarihi: 19.12.2019

eriyikleriyle etkileşmiş olan yaygın ve zenginleşmiş bir manto kaynağıyla ilişkili olduğunu açığa çıkarmıştır. Bunun bir sonucu olarakta, karbonatitik eriyikler, manto kaynağına jeokimyasal etkilerini bırakmış ve bu manto kaynağının kısmi ergimeside, bölgede K, NTE, Th ve U'ca zengin, yüksek radyasyon seviyeli volkanik materyalleri üretmiştir. Bu sonuçlar, karbonatitlerle etkileşmiş bir manto kaynağının, Isparta volkanik ve piroklastik kayaçlarının sadece belirgin elementlerce (örn, Th, U, NTE) zenginleşmelerinde değil aynı zamanda yüksek radyoaktivite seviyelerinde de anahtar bir rol oynadığına işaret etmektedir. Burada ayrıca, yapı malzemesi olarak kullanılan volkanik ve piroklastik kayaçlardaki yüksek radyasyonun potansiyel bir riski, karbonatitlerle modifiye olmuş bir manto kaynağından türemiş potasik mağmaların yüzeylendiği herhangi bir volkanik bölgeden beklenebileceğine de dikkat çekilmektedir.

Anahtar kelimeler: Isparta, potasik vokanizma, karbonatitik affinite, yüksek radyasyon, yapı malzemeleri.

1. Introduction

During the last decades, there is an increasing interest on radiological safety of rocks, due to their common usage as building raw materials, and effects on environmental pollution and human health. The specific levels of environmental radiation are related to the contents of thorium, uranium and potassium in the rocks and soils [1]. The most significant natural radionuclides are potassium (^{40}K), uranium (^{238}U), and thorium (^{232}Th) and their decay products. Igneous rocks from which building materials produced, commonly include these radionuclides, and are one of the sources of direct radiation. Information on their radionuclides concentrations and dispersions also provide useful information for monitoring natural radioactivity and environmental pollution [2]. Accordingly, the natural radiation is the main contributor to the external dose of the population and important to assess the gamma radiation dose from natural sources [3]. The concentrations of natural radionuclides in building raw materials (e.g., cement, bricks, concrete) are also measured to establish dose criteria [4-6]. In this regard, plenty of radioactivity measurements in magmatic rocks and in building raw materials from different localities of Turkey have been researched and reported by several workers [1-3,7-16]. From the natural radioactivity assessments in construction materials in Elazığ, Turkey [11], highest radiation value obtained in gas concrete (as 405.2 Bq/kg), which is higher than global values (370 Bq/kg). Similarly, mean activity concentrations in cement in Turkey [15] are lower than international standart values. Amongst the activity measurements in magmatic products from different localities in Turkey, the most remarkable values, which are close to the internationally accepted upper limit and enriched three times more than those of the other Turkish magmatic products, were obtained from the Isparta volcanic field. In this study, to better understanding of the reason for the high radioactivity levels in Isparta volcanic and pyroclastic rocks, a specific research have been performed on the relationship between their magma styles and source characteristics.

2. Volcanic Setting in Isparta Region

During Pliocene to Quaternary period of historical volcanic activity in Isparta region (SW Turkey), Gölcük explosive volcano and concomitant volcanic eruptions produced various types of volcanic (e.g., trachyte, trachyandesite, phonolite, leucite ankaratrite, lamprophyre) and pyroclastic products (e.g., ignimbrite, tuff, pumice) (Figure 1) [17-19]. Such volcanic products widespreadly exposed at surrounding areas of Isparta city centre, and overlies the pre-volcanic units (Figure 1). From these volcanic products, pumice is used to make lightweight building materials such as concrete and concrete block and for plastering the buildings made of bricks [16], and trachyandesite (locally known as andesite stone) is used as pavement stone.

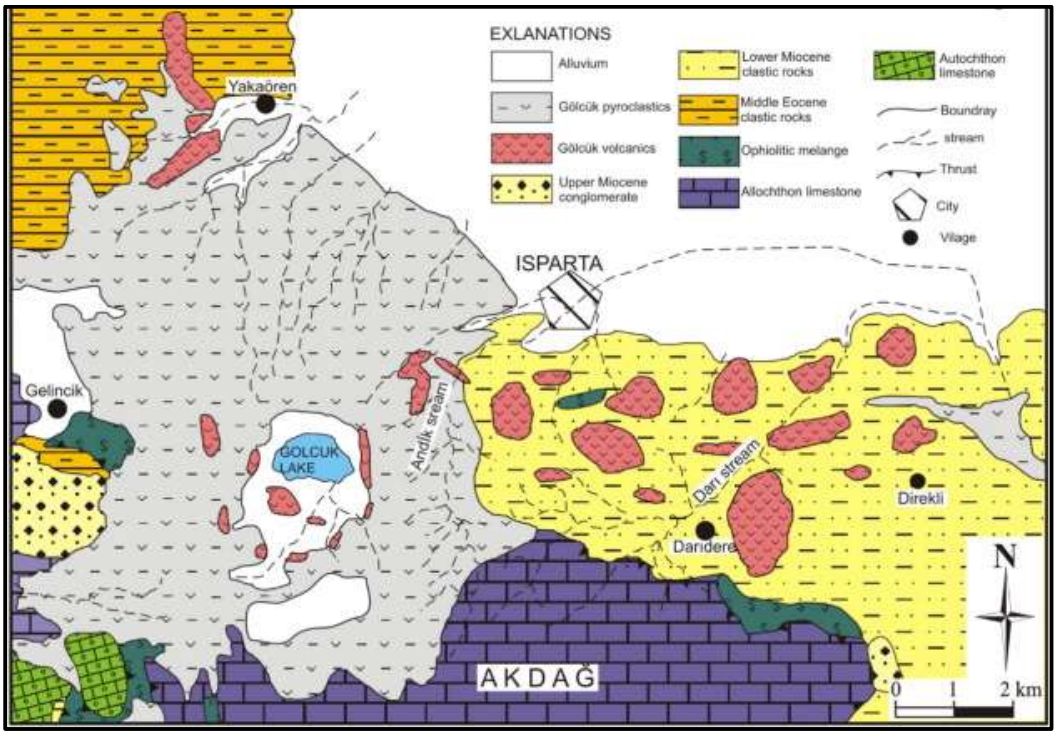

Figure 1. Simplified geological map of the Isparta region. Modified from [24].

3. Results

3.1. Th, U and REE Geochemistry of Isparta Potassic Volcanism

Potassic nature's and elevated concentrations of radiogenic elements (e.g.,Th and U) and total rare earth elements (∑REE) are the most diagnostic feature of the Isparta volcanism (Table 1). These characteristics also show a geochemical similarity to those of some carbonatites (e.g., Norway and Kenya carbonatites, [20,21]). Isparta volcanites were derived from two magma types; potassic-shoshonitic magmas and ultrapotassic magmas [17-19]. Average K_2O/Na_2O ratio of potassic-shoshonitic magmas, from which trachytes, trachyandesites, phonolites, ankaratrites, pumices, tuffs and ignimbrites produced, is ≈ 1, and K_2O contents almost range between 3 – 6 wt.% (Table 1). In ultrapotassic magmas, from which lamprophyres produced, average K_2O/Na_2O ratio is greater than 2, and K_2O contents can reach up to 10 wt.% [17,19]. All volcanic and volcanoclastic rocks are characterized by enrichments in distinct elements, e.g., ∑REE (up to 1325 ppm in phonolite; 733 ppm in trachyandesite; 805 ppm in ankaratrite; 695 ppm in lamprophyre), radiogenic Th (up to 138 ppm in pumice; 128 ppm in trachyandesite; 103 ppm in phonolite) and U (up to 37 ppm in pumice; 28 ppm in trachyandesite, 22 ppm in phonolite) (Table 1). Highest concentrations of Th (145 ppm), U (249 ppm) and ∑REE (32012 ppm) found in ultramafic xenoliths, which are represent to an enriched mantle source (Table 1).

3.2. Measured Radioation Levels in Magmatic Products from Turkey and in Some Carbonatites

Available radioactivity measurements of ^{226}Ra, ^{238}U, ^{232}Th and ^{40}K (Bq/kg) in tuffs, granites and pumice samples from different regions in Turkey, together with those of Isparta volcanic and pyroclastic rocks, are given in Table 2. Results show that except for Isparta samples, measured radiation levels of magmatic rocks in Turkey are low, and below the international accepted limits (370 Bq/kg). In contrast, Isparta volcanic and pyroclastic rocks contain enhanced concentrations of natural radioactivity, with respect to the other Turkey magmatic products. For example, in Isparta pumice, ^{226}Ra values reach up to 256.2 Bq/kg. In Isparta volcanic rocks, ^{238}U values reach up to 444 Bq/kg, ^{232}Th values reach up to 408 Bq/kg and ^{40}K reach up to 1959 Bq/kg (Table 2). As mentioned before, Isparta volcanics also carry the typical geochemical characteristics of carbonatites, and high radioactivity levels also reported from

some carbonatite occurrences (e.g., Norway and Kenya carbonatites; [20,21]). In Norway carbonatites [20], ^{226}Ra values reach up to 300 Bq/kg in rauhaugite, ^{232}Th values reach up to 5900 Bq/kg in rödberg, and ^{40}K reach up to 1500 Bq/kg in fenite. In Kenya carbonatites [21], ^{238}U values reach up to 909 Bq/kg and ^{232}Th values reach up to 4247 Bq/kg and ^{40}K reach up to 1166 Bq/kg.

Table 1. Th, U and REE concentrations in Isparta potassic volcanics and in mantle xenoliths found in pyroclastics

	Rock Type		Th (ppm)	U (ppm)	K_2O (wt.%)	K_2O/Na_2O	∑REE (ppm)	References
ISPARTA	Potassic Volcanic Rocks	Phonolite	103	22,2	4,4	1,0	1325	[19]
			70	10,6	6,5	1,1	1274	[18]
		trachyte-trachyandesite	128	28,0	6,5	1,0	635	[22]
			98	25,0	6,0	1,1	733	[23]
		ankaratrite	38	9,8	4,4	1,5	713	[24]
			33	8,8	4,0	1,8	805	
	Ultrapotassic Rocks	lamprophyre	35,6	9,5	4,4	2,5	489	[19]
			33,8	6,2	5,4	2,0	695	[17]
	Xenoliths	Ultramafic	145	29,0	3,6	0,6	1366	[23]
		mafic, felsic	132	249	7,0	11,8	32012	[25]

Table 2. Radioactivity measurements in magmatic rocks in Isparta and in other locations of Turkey

Location	Rock type	^{226}Ra (Bq/kg)	^{238}U (Bq/kg)	^{232}Th (Bq/kg)	^{40}K (Bq/kg)	References
Central Anatolia	Tuff (average)	17,8-97,2 (50,4)		17,4-96,0 (58,6)	229-1036 (717,6)	[13]
Turkey (Isparta not included)	Tuff	2-108	3-129	8,0-89,0	99-1147	[8]
	Granite (average)	0,7-186 (69,4)		0,5-249 (83,19)	166-1923 (1234)	[12]
	Pumice (average)	12,7-166,7 (80,9)		12,3-161,7 (80,5)	445-1847 (1254)	[16]
Western Turkey	Granite (average)	15,6-139,7 (60,5)			297-880 (632)	[14]
Eastern Mediterranean	Pumice	15,7		16,11	403	[2]
Isparta	Volcanic		204-444	234-408	1608-1959	[1]
	Trachyandesite		351	261,4	1460	[10,26]
	Pyroclastic		172-280	192-278	1261-1555	[1]
	Tuff	146-197	211-356	159-366	940-1290	[8]
	Pumice (average)	235,9-256,2 (244,4)		224,4-237,9 (231,4)	1613-1840 (1743)	[16] [7]

Discussion

The origin of Isparta Plio-Quaternary potassic-ultrapotassic volcanism is associated with a lithospheric mantle source metasomatized by slab derived melts/fluids and asthenospheric melts [19,24,27]. Recent petrological studies also demonstrated that the asthenospheric carbonatite melts were played a key role on the mantle lithosphere of Isparta Plio-Quaternary volcanism, and they interacted and modified the wall-rock peridotites [24,27]. Hence, carbonatite melts left their geochemical imprints into these mantle metasomes. Partial melting of carbonatite- and slab melts-modified lithospheric mantle produced the several types of volcanic and pyroclastic products in the region. Thus, high Th, U and REE concentrations in Isparta volcanic and pyroclastic rocks can be explained by observed carbonatitic affinity, since carbonatites are the main carrier of REE and some radiogenic elements (e.g., Th and U). Presence of highest concentrations of Th, U and REE in ultramafic xenoliths found in pyroclastic rocks support this arguement (see Table 1). Accordingly, measured high radioactivity levels in some carbonatites (e.g., Norway and Kenya) [20,21], also can provide an evidence for elevated radiation ratios of Isparta potassic volcanics. These petrological inferrence also suggest that since their usage of building and industrial raw materials, a potential risk of high radiation in volcanic and pyroclastic rocks can be expected for a given volcanic region, which include potassic magma derived from a carbonatite-modified mantle source.

4. Conclusions

Obtained radioactivity measurements in magmatic products in Turkey demonstrated that Isparta volcanic field carry values by more than three times the magmatic products in other locations. In this study, a spesific geochemical research on potassic magmas and source characteristics of volcanic and pyroclastic products in Isparta volcanic field have been realised to clarify the reason for their high radioactivity levels. Results are given below:

1. High radioactivity (^{40}K, ^{238}U, ^{232}Th) levels in Isparta volcanic and pyroclastic rocks are related to the high elemental concentrations of K, Th and U in these volcanic products.
2. High REE concentrations in Isparta potassic volcanic products derived from a carbonatite-modified mantle source, together with high Th and U, are typical characteristics of those of some mantle-derived carbonatites (e.g., Norway and Kenya).
3. Presence of high radiation levels in mantle-derived carbonatites (e.g., Norwage and Kenya) indicates that high radiation levels in Isparta volcanic products are related to role of carbonatitic melts in the genesis of Isparta volcanics.
4. Carbonatite melts left their chemical effects in the mantle source, and partial melting of this carbonatite-modified mantle produced several types of volcanic products with high radiation levels in the Isparta region.
5. It is also concluded that a potential risk of high radiation in volcanic and pyroclastic rocks used as building raw materials can be expected for a given volcanic region, which include potassic magma derived from a carbonatite-modified mantle source.

References

[1] Kalyoncuoğlu Ü.Y. 2015. In situ gamma source radioactivity measurement in Isparta plain, Turkey. Environmental Earth Sciences, 73: 3159–3175

[2] Kilic A.M., Aykamis A.S. 2009. The natural radioactivity levels and radiation hazard of pumice from the East Mediterranean Region of Turkey. Bulletin of Engineering Geology and Environment, 68: 331–338.

[3] Akkurt İ., Uyanık N.A., Günoğlu K. 2015. Radiation dose Estimation: An in vitro measurement for Isparta-Turkey. International Journal of Computational and Experimental Science and Engineering (IJCESEN), 1 (1): 1-4.

[4] Trevisi R., Risica S., D'Alessandro M., Paradiso D., Nuccetelli C. 2012. Natural radioactivity in building materials in the European Union: a database and an estimate of radiological significance. Journal of Environmental Radioactivity, 105: 11-20.

[5] Nuccetelli C., Risica1 S., D'Alessandro M., Trevisi R. 2012. Natural radioactivity in building material in the European Union: robustness of the activity concentration index I and comparison with a room model. Journal of Radiological Protection, 32: 349–358.
[6] Sas Z., Doherty R., Kovacs T., Soutsos M., Sha W., Schroeyers W. 2017. Radiological evaluation of by-products used in construction and alternative applications; Part I. Preparation of a natural radioactivity database. Construction and Building Materials, 150 (30): 227-237.
[7] Turhan Ş., Yücel H., Gündüz L., Şahin Ş., Vural M., Parmaksiz A., Demircioglu B. 2007. Natural radioactivity measurement in pumice samples used raw materials in Turkey. Applied Radiation and Isotopes, 65 (3): 350-354.
[8] Turhan Ş., Atıcı E., Varinlioğlu A. 2015. Radiometric analysis of volcanic tuff stones used as ornamental and structural building materials in Turkey and evaluation of radiological risk. Radioprotection, 50 (4): 273-280.
[9] Turhan, S. 2008. Assessment of the natural radioactivity and radiological hazards in Turkish cement and its raw materials. Journal of Environmental Radioactivity, 99: 404-414.
[10] Uyanik N.A., Akkurt I., Uyanik O. 2010. A ground radiometric study of uranium, thorium and potassium in Isparta, Turkey. Annals of Geophysics, 53 (5-6): doi: 10.4401/ag-4726.
[11] Baykara O., Karatepe Ş., Doğru M. 2011. Assessments of natural radioactivity and radiological hazards in construction materials used in Elazig, Turkey. Radiation Measurements, 46 (1): 153-158.
[12] Çetin E., Altinsoy N., Örgün Y. 2012. Natural radioactivity levels of granites used in Turkey. Radiation Protection Dosimetry, 151 (2): 299–305.
[13] Değerlier M. 2013. Assessment of natural radioactivity and radiation hazard in volcanic tuff stones used as building and decoration materials in the Cappadocia region, Turkey. Radioprotection, 48 (2): 215-229.
[14] Tatar Erkül S., Özmen S.F., Erkül F., Boztosun İ. 2016. Comparison between natural radioactivity levels and geochemistry of some granitoids in western Turkey. Turkish Journal of Earth Science, 25: 242-255.
[15] Özdiş B.E., Çam N.F., Canbaz B., Öztürk B.C. 2017. Assessment of natural radioactivity in cements used as building materials in Turkey. Journal of Radioanalytical and Nuclear Chemistry, 311: 307–316.
[16] Turhan Ş., Gündüz L. 2008. Determination of specific activity of 226Ra, 232Th and 40K for assessment of radiation hazards from Turkish pumice samples. Journal of Environmental Radioactivity, 99 (2): 332-342.
[17] Görmüş M., Sagular E.K., Çoban H., 2002. The Miocene sequence characteristics, its contact relation to the older rocks and lamprophyric dykes in the Dereboğazı area (S Isparta, Turkey). Ö.T. Akıncı, M. Görmüş, M. Kuşçu, R. Karagüzel, M. Bozcu (Eds.), Proceedings of the 4th International Symposium on Eastern Mediterranean Geology, Süleyman Demirel University, Isparta, Turkey, 69-90.
[18] Kumral M., Çoban H., Gedikoglu A., Kilinc A. 2006. Petrology and geochemistry of augite trachytes and porphyritic trachytes from the Gölcük volcanic region, Isparta, SW Turkey: A case study. Journal of Asian Earth Sciences, 27 (5): 707-716.
[19] Elitok Ö., Özgür N., Drüppel K., Dilek Y., Platevoet B., Guillou H., Poisson A., Scaillet S., Satır M., Siebel W., Bardintzeff J.-M., Deniel C., Yılmaz K. 2010. Origin and geodynamic evolution of late Cenozoic potassium-rich volcanism in the Isparta area, southwestern Turkey. International Geology Review, 52 (4–6): 454-504.
[20] Sundal A.V., Strand T. 2004. Indoor gamma radiation and radon concentrations in a Norwegian carbonatite area. Journal of Environmental Radioactivity, 77 (2): 175-189.
[21] Kaniua M.I., Angeyo H.K., Darby I.G., Muiac L.M. 2018. Rapid in-situ radiometric assessment of the Mrima-Kiruku high background radiation anomaly complex of Kenya. Journal of Environmental Radioactivity, 188: 47-57.
[22] Kumral M., Çoban H., Caran Ş. 2007. Th, U and LREE-Bearing grossular, chromian ferriallanite-(Ce) and chromian cerite-(Ce) in skarn xenoliths ejected from the Gölcük maar crater, Isparta, Anatolia, Turkey. The Canadian Mineralogist, 45: 1119-1125.
[23] Platevoet B., Elitok Ö., Guillou H., Bardintzeff J.-M., Yağmurlu F., Nomade S., Poisson A., Deniel C., Özgür N. 2014. Petrology of Quaternary volcanic rocks and related plutonic xenoliths

from Gölcük Volcano, Isparta Angle, Turkey: origin and evolution of the high-K alkaline series. Journal of Asian Earth Sciences, 92: 53-76.

[24] Caran Ş. 2016. Mineralogy and petrology of leucite ankaratrites with affinities to kamafugites and carbonatites from the Kayıköy area, Isparta, SW Anatolia, Turkey: implications for the influences of carbonatite metasomatism into the parental mantle sources of silica-undersaturated potassic magmas. Lithos, 256–257: 13-25.

[25] Yılmaz K. 2019. Geochemistry of ultramafic, mafic, and felsic xenoliths from the Gölcük (Isparta, SW Turkey) alkali rocks: genetic relationship with arc magmas. Arabian Journal of Geosciences, 12: 306. https://doi.org/10.1007/s12517-019-4461-6

[26] Uyanık N.A., Uyanık O., Akkurt İ. 2013. Micro-zoning of the natural radioactivity levels and seismic velocities of potential residential areas in volcanic fields: The case of Isparta (Turkey). Journal of Applied Geophysics, 98: 191-204.

[27] Çoban H., Topuz G., Roden M.F., Hoang N., Schwarz W.H. 2019. ^{40}Ar-^{39}Ar dating and petrology of monzonite ejecta in tephra from Quaternary Gölcük volcano (Isparta, SW Turkey): tear-related contrasting metasomatic symptoms in extensional mantle-derived magmas. Lithos, 330–331: 160-176.

BEU FEN BİLİMLERİ DERGİSİ
YAZIM KURALLARI

İLK SUNUŞ FORMATI

Makaleler elektronik ortamda Word dosyası olarak sunulmalıdır. Makale, A4 kâğıda, 11 punto büyüklüğündeki Times New Roman fontuyla, tüm kenarlardan 2,5 cm boşluk bırakılarak, tek satır aralıklı olarak yazılmalıdır. Makaleler 20 sayfayı geçmeyecek şekilde yazılmalı ve online olarak http://dergipark.gov.tr/bitlisfen adresinden gönderilmelidir. Kör hakemlik uygulamasından dolayı makale ana dosyasında yazar bilgileri verilmemelidir. Yazar bilgileri ayrı bir dosya yüklenerek verilmelidir. Bir sayıda aynı yazara ait en fazla 2 yayın bulunabilir. **Gönderiler, araştırma ve yayın etiğine uygun olmak zorundadır.** Makaleler aşağıda verilen düzene ve kurallara göre yazılmalıdır.

Makalenin ana bölümleri Giriş, Materyal ve Metot, Bulgular ve Tartışma, Sonuç ve Kaynaklardan oluşur.

Benzerlik Oranı: Gönderilen makalelerin benzerlik oranı %15'i geçmemelidir. Her bir benzerlik oranı ise %3'i geçmemelidir.

Makale Dili: Türkçe veya İngilizce'dir.

Başlık: İçeriğe uygun, kısa ve anlaşılır olmalıdır. Türkçe ve İngilizce başlıklar Times New Roman, 14 punto, kalın (**bold**), ilk harfleri büyük ve ortalanarak yazılmalıdır.

Yazar isimleri ve adresleri: Başlığın altındaki yazar isimleri kısaltmasız, ilk harf büyük ve soyadı büyük harflerle, 12 punto, ortalı olarak yazılmalıdır. Yazar isimlerinden sonra virgül ve adres belirtmek için üst simge olarak rakam kullanılmalıdır (1, 2, 3, gibi). Sorumlu yazar isminde mutlaka üst simge yıldız sembolü olmalıdır
(*). Yazarların tam adresleri isimlerinin hemen alt kısmına küçük harflerle (İlk harfler büyük), ortalı, italik ve 10 punto yazılmalı, sorumlu yazarın e-mail adresi ilk sayfanın sol alt köşesinde (*) sembolü ile belirtilmelidir.

Özet ve Anahtar kelimeler (Summary ve Keywords): Makalede Türkçe ve İngilizce öz olmalı ve makale özü en az 75, en fazla 250 sözcük içerecek şekilde 10 punto olarak yazılmalıdır. Her iki özün hemen altında en az 3, en fazla 6 sözcükten oluşan Anahtar Kelimeler (Keywords) 10 punto olarak yazılmalıdır.

Ana Metin: Makaledeki ana başlıklar ve varsa alt başlıklar anlaşılır ve numaralı olmalıdır. Tüm ana metin başlıkları sola yanaşık, İlk harfleri büyük diğerleri küçük harflerle, 11 punto ve kalın karakter olmalıdır. Alt başlıklar 11 punto yazılmalıdır. Metin; iki yana yaslı, paragraflar arası satır boşluğu kullanılmamalı, alt başlıklardan hemen sonraki ilk paragrafta girinti olmamalıdır.

Giriş: Konu hakkında kısa bir literatür bilgisi vermeli, sonunda çalışmanın amacı kısaca belirtilmelidir.

Materyal ve Metot: Detaylı ve açıklayıcı bir biçimde verilmelidir.

Bulgular ve Tartışma: Bu bölümde elde edilen sonuçlara yer verilmeli, sonuçlar gerekirse şekil ve tablolarla da desteklenmelidir. Elde edilen bulgular ilgili literatürlerle karşılaştırılmalıdır.

Sonuç ve Öneriler: Sonuçlar gereksiz tekrarlardan kaçınılarak mutlaka yorumlanmalıdır. Sonuçların başka araştırmalarla benzerlik ve farklılıkları verilmeli, bunların olası nedenleri tartışılmalıdır.

Teşekkür: Gerek görüldüğü takdirde ya da proje vs. kapsamında bir çalışma ise; çalışmada yardımları olan kişi(ler), kurum ve kuruluşlara yardım ve desteklerinden dolayı teşekkür edilmelidir.

Kaynaklar: Kaynakların metin içinde gösterimi numara sırasına göre olmalıdır ([1], [2] v.b.). Makale içinde verilen her kaynak, makalenin Kaynaklar kısmında mutlaka yer almalıdır. Kaynaklar makale sonunda numara sırasına göre verilmelidir. Kaynakların makale sonundaki gösterimi aşağıdaki örneklerdeki gibi olmalıdır.

Kaynak bir makale ise;

1. Köksal K., Koç F. 2016. Optical Manipulation of Photo-induced Current in Spherical Semiconductor Quantum Dots by Optical Vortices, Philosophical Magazine, 96 (25): 2686-2695.
2. Öztürk Ö. 2017. A Different Solution Method for the Confluent Hypergeometric Equation, Iğdır Üniversitesi Fen Bilimleri Enstitüsü Dergisi, 7 (2): 215-224.
3. Kurşat M., Emre İ.,Yılmaz Ö., Erecevit P. 2011. Antioxidant and antimicrobial activity in the seeds of *Origanum vulgare* L. subsp. *gracile* (C. Koch) Ietswaart and *Origanum acutidens* (Hand.-Mazz.) Ietswaart from Turkey, Grasas y aceites, 62 (4): 410-417.

Kaynak bir kitap ise;

1. Chapra C.S., Canale R.P. 2003. *Yazılım ve Programlama Uygulamalarıyla Mühendisler için Sayısal Yöntemler*, Literatür Yayınları, 1004s. İstanbul.
2. Demirsoy A. 1999. *Genel ve Türkiye Zoocoğrafyası "Hayvan Coğrafyası"*. Meteksan Yayınları, 965s.
   Ankara.

Kitap bölümü ise;

1. Cullen J. 1975. Artemisia L. in *Flora of Turkey and East Aegean Islands,* Edited by Davis PH, Vol.5, Edinburgh: Edinburgh Univ Press, 311-324.
2. Cassidy J., Elder R. 1984. Spillways of high dams, in *Developments in Hydraulic Engineering 2,* Edited by Novak P., Aplied Science Publishers Ltd. Essex, UK, 153-173.

Kaynak sempozyum ise;

1. Akyüz M., Kırbağ S. 2012. Fatty Acid and Vitamin Compsition of Pleurotus eryngii var.ferulae Grown on Various Agro-wastes, 21. Ulusal Biyoloji Kongresi, pp1168-1169, 3-7 Eylül, İzmir.
2. Tabur M.A., Uzun A., Ayvaz Y. 2004. Why is White-headed Duck Wintering in Lake Burdur (Turkey) decreasing? 1st International Eurasian Ornithology Congress 8-11 April , Abstract Book, 63s. Antalya.

Web adresi;

İnternet kaynağın yazar ismi ve tarihi biliniyorsa;

1. Şenel F. 2006. Kırım-Kongo Kanamalı Ateşi. http://www.biltek. tubitak.gov. tr/ pdf/ kene. (Erişim Tarihi: 21.01.2007).

Yazar ve tarih isimleri bilinmiyorsa;

1. Biyolojik çeşitlilik 2005. Türkiye'nin Biyolojik Çeşitliliği. http://www.bcs.gov.tr/1.4.php (Erişim tarihi:
   15.01.2007).

Kaynak Tez ise;

1. Kurşat M. 2010. Türkiye'de Yetişen *Artemisia* L. (*Asteraceae*) Taksonlarının Taksonomik Revizyonu. Fırat Üniversitesi, Fen Bilimleri Enstitüsü, Doktora tezi, 348s, Elazığ.

Kaynak Anonim ise;

1. Anonim, 1990. Sulak Alanların Korunması. Doğal Hayatı Koruma Derneği, 93s. İstanbul.

Şekil ve Tablolar: Fotoğraf, resim, çizim ve grafik gibi göstermeler şekil olarak verilmelidir. Resim, şekil ve grafikler net ve ofset baskı tekniğine uygun olmalıdır. Şekiller (Renkli ve siyah-beyaz fotoğraflar, siyah-beyaz çizimler, haritalar) metin içerisinde verilmelidir. Şekiller 16x20 cm den büyük olmamalıdır. Resim ve fotoğraflar en az 600 dpi çözünürlükte olmalıdır. Tüm tablo ve şekiller makale

boyunca sırayla numaralandırılmalı (Tablo 1., Şekil 1.), başlık ve açıklamalar içermelidir. Açıklamaların sonunda nokta veya virgül konulmamalıdır. Tablo başlıkları tablonun üstünde, şekil başlıkları ise şekil altında ortalı ve 10 punto olmalıdır.

Birim Sistemi: Makalelerde kullanılan birim sistemleri SI birim sistemlerine uyumlu olmalıdır.

Yayına Kabul Edilen Makalelerin Son Düzeltmelerindeki Dikkat Edilecek Hususlar

Tüm kenar boşlukları (sağ, sol, üst ve alt) 2,5 cm ve satır aralığı tek olmalı,

- Özetler 10 punto, ana metin 11 punto olmalı,
- Makale başlıkları (Türkçe – İngilizce) 14 punto, kalın yalnızca ilk harfler büyük,
- Metin ana başlıkları 11 punto, kalın yalnız ilk harfler büyük,
- Alt başlıklar 11 punto, kalın ve sadece ilk harfi büyük olmalıdır.

BEU JOURNAL OF SCIENCE

Manuscript Preparation

Format of First Submission

Manuscripts should be submitted digitally as MS Word. Files should be prepared by using A4 paper size with 2.5 cm margin from all sides, in 11 font size and Times New Roman font with single space. Manuscripts should not exceed 20 pages and should be submitted via http://dergipark.gov.tr/bitlisfen web site. Author informations should not be given in the main file of the article due to blind review. Author informations should be given by uploading a different file. Up to 2 publications of the same author can be found in one issue. Submissions must comply with research and publication. Manuscripts should be written according to following rules and structure.

Main sections of the article are Introduction, Material and Methods, Results and Discussion, and References. An Acknowledgement section can be included before References.

Similarity Ratio: The similarity rate of submitted articles should not exceed 15%. Each similarity rate should not exceed 3%.

Manuscript Language: Turkish or English.

Title: It should a concise and clear phrase describing the content of the text. Both Turkish and English titles should be centered and bold in Times New Roman with 14 font size and First Letters Should Be Capitalized.

Author Names and Addresses: Full names of all authors are given below the title. Surnames (Family Names) and first letters of the Given Names should be capitalized with 12 font size as centered. Author names are separated by coma. Superscript Arabic letters ([1], [2], [3], ect.) should be used to indicate addresses. Corresponding author should be indicated with an asterisk (*). Full addresses of the authors should be written with lower case italic letter and be centered (10 font) immediately after author names. E-mail address of the corresponding author should be given lower left corner of the first page, leading with an asterisk (*).

Abstract and Key Words: All manuscript should include Turkish and English abstracts and each abstract should be written in 10 font size including at least 75 words and at most 250 words. Keywords consisting of at least 3 words and at most 6 words should be written in 10 points just under both abstracts.

Main Text: Titles of main sections and subsections should be comprehensible and numbered. All main section titles should be left aligned, bold, and in 11 font size with capitalized first letters. Subsection titles should be in 11 font size. The text should be justified. There should be no space between paragraphs. Paragraphs following a title should not have first-line indent.

Introduction: A brief summary of the subject and the current literature should be given. The aim of the study should be briefly stated at the end.

Material and Method: It should be given in detail and clearly.

Results and Discussion: The results should be presented in a comprehensible manner which may include figures and tables. Presented results should be compared with the literature.

Conclusion: The results should be interpreted in avoiding unnecessary repetitions. It should be stated and discussed with its possible reasons if the results comply with previous studies or not.

Acknowledgement: If appropriate, acknowledgements to sponsor(s) and assisting individual(s) should be given.

References: References should be cited in text according to order of appetences with Arabic numbers in square brackets (e.g. [1], [2], ect.). All references cited in the text should be listed in References and vice versa. Journal names should not be abbreviated in the References. References should be listed according to numeric order at the end of the article. References should be written according to following examples.

Article:

1. Köksal K., Koç F. 2016. Optical Manipulation of Photo-induced Current in Spherical Semiconductor Quantum Dots by Optical Vortices, Philosophical Magazine, 96 (25): 2686-2695.
2. Öztürk Ö. 2017. A Different Solution Method for the Confluent Hypergeometric Equation, Iğdır Üniversitesi Fen Bilimleri Enstitüsü Dergisi, 7 (2): 215-224.
3. Kurşat M., Emre İ.,Yılmaz Ö., Erecevit P. 2011. Antioxidant and antimicrobial activity in the seeds of *Origanum vulgare* L. subsp. *gracile* (C. Koch) Ietswaart and *Origanum acutidens* (Hand.-Mazz.) Ietswaart from Turkey, Grasas y aceites, 62 (4): 410-417.

Book:

1. Chapra C.S., Canale R.P. 2003. *Yazılım ve Programlama Uygulamalarıyla Mühendisler için Sayısal Yöntemler*, Literatür Yayınları, 1004s. İstanbul.
2. Demirsoy A. 1999. *Genel ve Türkiye Zoocoğrafyası "Hayvan Coğrafyası"*. Meteksan Yayınları, 965s. Ankara.

Book Chapter:

1. Cullen J. 1975. Artemisia L. in *Flora of Turkey and East Aegean Islands,* Edited by Davis PH, Vol.5, Edinburgh: Edinburgh Univ Press, 311-324.
2. Cassidy J., Elder R. 1984. Spillways of high dams, in *Developments in Hydraulic Engineering 2,* Edited by Novak P., Aplied Science Publishers Ltd. Essex, UK, 153-173.

Symposium Proceeding:

1. Akyüz M., Kırbağ S. 2012. Fatty Acid and Vitamin Composition of Pleurotus eryngii var.ferulae Grown on Various Agro-wastes, 21. Ulusal Biyoloji Kongresi, pp1168-1169, 3-7 Eylül, İzmir.
2. Tabur M.A., Uzun A., Ayvaz Y. 2004. Why is White-headed Duck Wintering in Lake Burdur (Turkey) decreasing? 1st International Eurasian Ornithology Congress 8-11 April , Abstract Book, 63s. Antalya.

Web sites:

If the author name and date are known:

1. Senel F. 2006. Kirim-Kongo Kanamali Atesi. http://www.biltek. tubitak.gov. tr/ pdf/ kene. (Access Date: 21.01.2007).

If the author name and date are unknown:

1. Biyolojik çesitlilik 2005. Türkiye'nin Biyolojik Çesitliligi, http://www.bcs.gov.tr/1.4.php (Access Date: 15.01.2007).

Thesis:

1. Kursat M. 2010. Türkiye'de Yetisen *Artemisia* L. (*Asteraceae*) Taksonlarinin Taksonomik Revizyonu. Firat Üniversitesi, Fen Bilimleri Enstitüsü, PhD Thesis, 348s, Elazig.

Ananimous:

1. Anonymous, 1990. Sulak Alanlarin Korunmasi. Dogal Hayati Koruma Dernegi, 93s. Istanbul.

Figures and Tables: Images like photos, pictures, drawings, and graphs should be given as figures. Figures should be clear and appropriate for press. All figures should be given within the text. Figures should not exceed the size of 16x20 cm. Pixel based figures should be minimum of 600 dpi. All tables and figures should be numbered (e.g. Table 1, Figure 1), and should include a title and legend. There should be no period or comma after the legend. The tiles should be centered and in 10 font size. Tables and figure titles should be placed above the table and below the figure, respectively.

Units: All units should be given according to SI (International System of Units).

Final Check List For Articles Accepted For Publication

- All margins are 2.5 cm.
- Paragraphs are single spaced.
- Article titles (Turkish and English) are bold and in 14 font size with capitalized first letters.
- Main section titles are bold and in 11 font size with capitalized first letters.
- Subsection titles are bold and in 11 font size and only the first letter of the first word is capitalized.

BEU
FEN BİLİMLERİ DERGİSİ
YAYIN İLKELERİ

Bitlis Eren Üniversitesi Fen Bilimleri Dergisi, mühendislik ve temel bilimler alanlarındaki gelişmeleri ve yenilikleri takip etmek, meslek kuruluşlarının, araştırmacıların ve bireylerin ulusal ve uluslararası gelişimlerine katkıda bulunmak ve bu alanlarda elektronik bir kaynak oluşturmak amacıyla yayımlanmaktadır. Derginin yazım dili Türkçe veya İngilizcedir. Fen Bilimleri Dergisi, Bitlis Eren Üniversitesi Fen Bilimleri Enstitüsü yayını olup, 2012 yılından bu yana ücretsiz ve açık erişimli olarak yayın hayatına devam etmektedir. Mühendislik ve temel bilimlerin bilgi tabanına ve teknolojik gelişmelere ışık tutması amacıyla bu alanlarda yapılmış deneysel ve teorik ilerlemeleri konu alan özgün araştırma makalelerine, derlemelere ve teknik notlara yer verilmektedir. Dergiye gönderilen çalışmaların benzerlik oranı %15'i geçmemelidir. Yazım kurallarına uymayan makaleler, hakemlere gönderilmeden önce düzeltilmek üzere yazara geri gönderilir. Bu nedenle, derginin yazım kuralları dikkate alınmalıdır. Ayrıca, editörlerden yazarlara iletilen düzeltmelere veya taleplere 15 gün içerisinde cevap verilmediği takdirde ilgili makaleler reddedilir. Makaleler şekiller ve tablolar dâhil 20 sayfayı geçmemelidir. Dergiye yayın için gönderilen makaleler en az iki hakem tarafından değerlendirilir. Yazarlardan hakem önerisi talep edilmemektedir. Makalelerin dergide yayımlanabilmesi için hakemler tarafından olumlu görüş bildirilmesi gerekmektedir. Dergi Editör Kurulu, hakem raporlarını (iki hakemin değerlendirmeleri geldikten sonra) dikkate alarak makalelerin yayımlanmak üzere kabul edilip edilmemesine karar verir. Fen Bilimleri Dergisi, yılda iki defa (Haziran, Aralık) yayımlanmaktadır. **Dergimiz Tübitak-Ulakbim Mühendislik ve Temel Bilimler Veri Tabanı Dergi Listesinde taranmaktadır.**

Dergide yayımlanacak makalelerin bilimsel etik kuralları içerisinde olması gerekmektedir. Makalede yer alan tüm yazarlar, çalışmalarının yayın haklarını Bitlis Eren Üniversitesi Fen Bilimleri Dergisi'ne verdiklerine dair **Telif Hakları Formu**'nu imzalamalıdırlar. Bu form iletilmeden yayın kabul edilse de yayımlanmayacaktır. Bütün bu bilgiler aşağıdaki DergiPark sistemi, e-posta adresi veya posta adresi ile editörlüğe gönderilmelidir. Dergide yayımlanacak makalelerin içeriğinden kaynaklanan her türlü yasal sorumluluklar ve telif haklarına ilişkin doğabilecek hukuki sorumluluklar tamamen yazarlara aittir.

Bitlis Eren Üniversitesi
Fen Bilimleri Dergisi Editörlüğü

Bitlis Eren Üniversitesi
Fen Bilimleri Enstitüsü
13000, Merkez, Bitlis/TÜRKİYE
E-posta : fbe@beu.edu.tr
Web : http://dergipark.gov.tr/bitlisfen

Makale No/Article ID: ……

B.E.U.

FEN BİLİMLERİ DERGİSİ

Telif Hakkı Devir Formu / Copyright Form

[Makale Adı / Article title]

……

……

……

Başlıklı makalenin telif hakkından feragat etmeyi/ettiğimizi, makalenin telif hakkının Bitlis Eren Üniversitesi Fen Bilimleri Enstitüsü'ne devredildiğini ve Bitlis Eren Üniversitesi Fen Bilimleri Dergisi Editörlüğü makalenin yayımlanabilmesi konusunda yetkili kılındığını kabul eder ve imza ederiz.

Ayrıca, adı geçen makalenin tüm içeriği konusunda tüm sorumluluk yazar/yazarlara ait olup, makalenin içeriği konusunda doğabilecek sorunlardan Bitlis Eren Üniversitesi Fen Bilimleri Dergisi Editörlüğü sorumlu değildir.

Bütün yazarlar tarafından imzalanması gerekiyor: (Sorumlu yazar/Corresponding author*)

Yazarın Adı ve Soyadı / Author Names	İmzası / Signature	Tarih / Date
1 ……		
2 ……		
3 ……		
4 ……		
5 ……		

NOT: Eksik imza durumunda sorumluluk imzalayan yazarlara aittir. Form doldurulup imzalandıktan sonra online veya e-posta yoluyla gönderilmelidir:

Web : http://dergipark.gov.tr/bitlisfen

E-mail : fbe@beu.edu.tr

Article ID: ……..

BEU

JOURNAL OF SCIENCE

Copyright Transfer Form

We, the authors of the manuscript entitled

_____
_____
_____

relinquish our copyrights on the manuscript in favor of BEU Graduate School of Science. Hence, we, the authors, accept and signs for this copyright transfer which includes but not limited to granting the right to publish the manuscript to the Editorial Board of BEU Journal of Science.

Nevertheless, we, the authors, retain all responsibilities regarding the manuscript. The Editorial Board of BEU Journal of Science cannot be held responsible for any conflict due to the content of the manuscript, by any means.

All authors must sign:

Authors' Full Names	Signature	Date
1. _____	_____	_____
2. _____	_____	_____
3. _____	_____	_____
4. _____	_____	_____
5. _____	_____	_____

(Add additional lines if needed. Corresponding author should be indicated by "*".)

In case of absent signature, signing authors will be responsible. Filled and signed forms should be sent online or by email.

Web : http://dergipark.gov.tr/bitlisfen

E-mail : fbe@beu.edu.tr